Physics of behavior across scales

Borges Santos da Costa, A.C.

2020

document version
Publisher's PDF, also known as Version of record

Physics of behavior across scales

A dynamical systems approach to the representation and understanding of animal movement

Antonio Carlos Costa

This thesis was reviewed by:

Prof. dr. E. Peterman	Vrije Universiteit Amsterdam The Netherlands
Prof. dr. P.R. ten Wolde	Vrije Universiteit Amsterdam The Netherlands
Prof. dr. A. Celani	Internation Centre for Theoretical Physics Trieste Italy
Prof. dr. E. Lerner	Universiteit van Amsterdam The Netherlands
Prof. dr. G. Tkačik	Institute for Science and Technology Austria
Dr. E. Carroll	Delft University of Technology The Netherlands

Printed by: NORPRINT Artes Gráficas SA

An electronic version of this dissertation is available at
www.ubvu.vu.nl.

VRIJE UNIVERSITEIT

PHYSICS OF BEHAVIOR ACROSS SCALES

A dynamical systems approach to the representation and understanding of animal movement

ACADEMISCH PROEFSCHRIFT

ter verkrijging van de graad Doctor of Philosophy aan
de Vrije Universiteit Amsterdam,
op gezag van de rector magnificus
prof.dr. V. Subramaniam,
in het openbaar te verdedigen
ten overstaan van de promotiecommissie
van de Faculteit der Bètawetenschappen
op dinsdag 1 september 2020 om 13.45 uur
in de online bijeenkomst van de universiteit,
De Boelelaan 1105

door

Antonio Carlos Borges Santos da Costa

geboren te Povoa de Varzim, Portugal

promotor:	prof.dr. T.S. Shimizu
copromotor:	dr. G.J. Stephens

Para Luísa e Delfina

CONTENTS

1

INTRODUCTION

Since the earliest philosophers and mathematicians, much of our scientific endeavor strives for a description of natural phenomena that yields a large degree of quantitative detail. Physicists have successfully done so in a variety of topics, from the movement of planets to the inner working of the atom. Much of our understanding comes from intricate combination of three factors: being able to make very precise measurements, finding a representation that highlights the patterns in the measurements and creating the mathematical framework that pushes intuition into the quantitative realm. In most systems for which these three factors were verified, physicist have been able to develop solid predictive theories. One example, is the universal theory of gravitation. First, the observation of the movements of celestial bodies allowed for the formulation of various models of the solar system. One of the earliest prominent ideas was that the Earth was in the centre of the universe. Such an intuition drove Ptolemy to create a predictive model based on the intricate motion of spheres on spheres, which provided reasonably accurate predictions of the movement of planets, despite its complexity. Over the following centuries, first from Galileo's observations, and later through the precise measurements of Tycho Brahe, the Ptolemaic model was abandoned for heliocentric models, that put the sun in the centre of the Universe [1]. This change in representation, combined with the precision of Brahe's measurements, provided Kepler with the intuition to formulate his three laws of planetary motion [2], which were later solidified to a greater degree of

1

mathematical detail by Sir Isaac Newton and his universal theory of gravitation [3]. Therefore, having precise measurements, combined with the right representation, opens the path for the development of simpler theories that can achieve a greater level of quantitative detail and a deeper mechanistic understanding.

There are, however, a variety of phenomena for which we cannot achieve the same level of understanding. The most common example being quantum gravity and cosmology [4], where access to precise measurements is fundamentally limited. On the other hand, there is also a number of natural phenomena for which observation is not fundamentally limited and yet remains elusive to our understanding: the most recognized example being the general problem of turbulence [5]. In general, systems with a large number of degrees of freedom that exhibit non-negligible out-of-equilibrium dynamical properties continue to pose deep challenges to quantitative understanding. In general, such systems exhibit unpredictability at small scales, but also interpretable coarse-grained emergent properties. One example is that of the patterns of body movement in an animal. We certainly find it hard to catch a fly mid flight, but we have no problem saying it is "flying". Understanding such contrasting patterns of unpredictability and stereotypy in animal behavior will be one of the main focuses of this thesis.

The study of animal behavior dates back to the early twentieth century, with the advent of ethology [6, 7]. It is controlled at the finest scales by neuromusculatory mechanisms, but it is also modulated over long time scales through changes in the genetic expression of different neuromodulators or other environmental changes [8–10]. Understanding behavior would signify an advance in a number of fields, ranging from neuroscience, genetics and ethology [6, 7, 11–17] to control theory [18], robotics and artificial intelligence [19].

One of the challenges to building physics theories of animal behavior lies at the level of measurement and representation. Typically, the study of behavior by classical ethologists relied on expert observation and the careful annotation of different types of behaviors into ethograms [6, 7]. Nowadays, with recent advances in machine vision, precise measurements of behavior are becoming available, both at the level of collectives [20–23] and at the level of the body posture of single organisms [24–31]. However, the multiplicity of time and length scales in behavior [15] makes

it extremely challenging to find the right type of measurement and, above all, the right representation that can yield mechanistic understanding over such complex phenomena. In that sense, the physical study of behavior lags behind other branches of physics by a few centuries, but time is ripe for new representations and theories that bring our understanding of behavior to the level of physiology, genetics and neuroscience, perhaps in a complementary way.

The modern study of locomotory behavior in a laboratory setting typically starts with precise video imaging of positions and/or body postures over time [13–17], depending on the length and time scales of interest. Coarse-grained, centroid level descriptions of behavior are generally used to study navigation, or longer time scale changes in behavior coming from genetic expression or changes in the environment. These studies sometimes build Langevin-like phenomenological descriptions of the dynamics at large spatio-temporal scales that try to ignore the fine scale fluctuations coming from postural movements [32–46]. More recently, posture-level descriptions of behavior have become more common (see, e. g., [24, 26, 30]), in an attempt to get closer to muscular activity and the underlying neuronal control mechanisms [47]. Despite the obvious advantages of working at a posture-level description, new challenges arise. First of all, the body posture is inherently a higher dimensional measurement than the animals position (which is at most three dimensional). Luckily, despite the *a priori* large number of degrees of freedom an animal could explore, correlations between different body parts help reducing the dimensionality of the space of postures [24, 30, 48]. Unlike centroid-level dynamics, building simple interpretable models of complex high-dimensional postural dynamics that span the multiple spatio-temporal scales characteristic of behavior is exceedingly challenging. As such, most approaches focus on short time-scale movements, and devise various dynamical representations of the postural time series that allow for the distinction of different types of stereotyped movements, in close analogy to the classical ethologist's approach [14, 26, 30, 49]. However powerful, such approaches are often constrained to short time scale dynamics, and do not provide a principled means for bridging time scales and reaching the longer time scale phenomenological descriptions obtained with a centroid-level analysis. In this thesis, we will use *C. elegans* behavior as a playground for discussing these ideas of measurement, representation

and modelling of animal behavior on multiple scales.

C. elegans has long been a model organism in biology [10, 50], which has undoubtedly resulted in an outstanding wealth of information about the worm's genetics [51], development [52] and neural connectome [53]. In addition, recent advances in imaging have made it feasible to record a large fraction of the worm's nervous system at single-cell resolution in freely-behaving animals [54–57], and the ability to make genetic perturbations has highlighted the importance of neuromodulatory processes at orchestrating longer time scale behavioral sequences [10, 58–60]. Despite its "small" nervous system composed of 302 neurons, *C. elegans* exhibits complex behavioral patters that include behavioral plasticity, adaptation and learning [61–66], complex navigation strategies [44, 67–71] and even "sleep"-like states [72–75]. The worm's short generation time ($\sim$ 2 days) and small size ($\sim$ 1 mm in length) facilitate high resolution imaging of the worm's locomotion in a laboratory setting [45, 76]. The typical modern locomotion assay in *C. elegans* places the worm in a petri dish with agarose and makes use of high resolution imaging to extract positional and postural information [77]. On agar, the worm moves by propagating waves though its body: its behavioral repertoire [78, 79] is commonly characterized in terms of forward motion occasionally interrupted by brief reversals [37, 76, 80], during which the undulatory body wave that drives its movement switches direction [81]. In addition, worms reorient with a combination of gradual curves in the trajectory ("weathervaning") [68, 82] and sharp changes in body orientation (Ω-turns [80] and δ-turns [25]). These elementary behaviors are combined in exploring an environment [44, 68]: environmental cues such as chemical, mechanical, or thermal stimuli bias the frequency of different behaviors and their transitions, guiding the worm in favorable directions [44, 68–70]. In the absence of stimuli, worms exhibit large variability in their foraging strategies: when taken to a plate without food, worms tend to first do a local search with frequent reversals and turns and after a few minutes they start performing longer distance runs to quickly explore the environment [67]. Analogously, the worm's behavior on food is characterized by transitions between local search "dwelling" behavior and longer range "roaming" behavior [43, 58].

In Chapter 2, we will look at a centroid-level description of behavior, and build simple phenomenological models of the centroid speed and

head orientation that carry predictive power over coarse-grained statistics of the dynamics in a variety of nematode species, and reveals an exploration-exploitation axis underlying the variation in model parameters across species [83]. In Chapter 3 we will focus on a posture level representation of *C. elegans* behavior, and use the statistics of the space of adaptively defined locally-linear models to uncover broad stereotyped classes of behavior on short time scales [49]. In Chapters 4 and 5, we search for principles that can guide us towards finding a representation with which to bridge these time scales, from millisecond posture movements to minutes long navigation strategies [84]. We propose that state space reconstruction of the postural dynamics [85], combined with the approximation of the transfer operator on densities, provides a means to bridge the gap between fine scale postural descriptions and coarse-grained phenomenological models.

1

REFERENCES

[1] W. W. Bryant, *A History of Astronomy* (Methuen & Co., London, 1907).

[2] J. Kepler, *Epitome of Copernican Astronomy: & Harmonies of the World* (Promethus Books, Amherst, N.Y., 1995).

[3] I. Newton, *Newton's Principia : the mathematical principles of natural philosophy* (translation: Daniel Adee, New-York, 1846).

[4] R. P. Woodard, *How far are we from the quantum theory of gravity?* Reports on Progress in Physics **72**, 126002 (2009), arXiv:arXiv:0907.4238v1 .

[5] U. Frisch, *Turbulence: The Legacy of A. N. Kolmogorov* (Cambridge University Press, 1995).

[6] N. Tinbergen, *On aims and methods of Ethology,* Zeitschrift für Tierpsychologie **20**, 410 (1963).

[7] K. Lorenz and P. Leyhausen, *Motivation of human and animal behavior; an ethological view* (Van Nostrand Reinhold Co., New York, 1973).

[8] S. M. Kim, C.-Y. Su, and J. W. Wang, *Neuromodulation of Innate Behaviors in Drosophila ,* Annual Review of Neuroscience **40**, 327 (2017).

[9] F. Libersat and H.-J. Pflueger, *Monoamines and the Orchestration of Behavior,* BioScience **54**, 17 (2004).

[10] C. I. Bargmann and E. Marder, *From the connectome to brain function,* Nat Methods **10** (2013), 10.1016/j.cub.2012.01.061.

[11] N. Tinbergen, *The study of instinct.* (Clarendon Press/Oxford University Press, New York, NY, US, 1951) pp. xii, 237–xii, 237.

[12] A. Gomez-Marin, J. J. Paton, A. R. Kampff, R. M. Costa, and Z. F. Mainen, *Big behavioral data: psychology, ethology and the foundations of neuroscience.* Nature neuroscience **17**, 1455 (2014).

[13] J. W. Krakauer, A. A. Ghazanfar, A. Gomez-Marin, M. A. MacIver, and D. Poeppel, *Neuroscience Needs Behavior: Correcting a Reductionist Bias,* Neuron **93**, 480 (2017).

[14] A. E. Brown and B. De Bivort, *Ethology as a physical science,* Nature Physics , 1 (2018).

[15] G. J. Berman, *Measuring behavior across scales,* BMC Biol. **16** (2018), 10.1186/s12915-018-0494-7.

[16] S. R. Datta, D. J. Anderson, K. Branson, P. Perona, and A. Leifer, *Computational Neuroethology: A Call to Action,* Neuron **104**, 11 (2019).

[17] A. J. Calhoun and M. Murthy, *Quantifying behavior to solve sensorimotor transformations: advances from worms and flies,* Curr. Opin. Neurobiol. **46**, 90 (2017).

[18] N. J. Cowan, M. M. Ankarali, J. P. Dyhr, M. S. Madhav, E. Roth, S. Sefati, S. Sponberg, S. A. Stamper, E. S. Fortune, and T. L. Daniel, *Feedback control as a framework for understanding tradeoffs in biology,* American Zoologist **54**, 223 (2014).

[19] J. Aguilar, T. Zhang, F. Qian, M. Kingsbury, B. McInroe, N. Mazouchova, C. Li, R. Maladen, C. Gong, M. Travers, R. L. Hatton, H. Choset, P. B. Umbanhowar, and D. I. Goldman, *A review on locomotion robophysics: the study of movement at the intersection of robotics, soft matter and dynamical systems.* Reports on progress in physics. Physical Society (Great Britain) **79**, 110001 (2016).

[20] W. Bialek, A. Cavagna, I. Giardina, T. Mora, E. Silvestri, M. Viale, and A. M. Walczak, *Statistical mechanics for natural flocks of birds,* Proceedings of the National Academy of Sciences **109**, 4786 (2012).

[21] A. Pérez-Escudero, J. Vicente-Page, R. C. Hinz, S. Arganda, and G. G. de Polavieja, *idTracker: tracking individuals in a group by automatic identification of unmarked animals.* Nat. Methods **11**, 743 (2014).

[22] A. I. Dell, J. A. Bender, K. Branson, I. D. Couzin, G. G. de Polavieja, L. P. Noldus, A. Pérez-Escudero, P. Perona, A. D. Straw, M. Wikelski, and U. Brose, *Automated image-based tracking and its application in ecology,* Trends in Ecology and Evolution **29**, 417 (2014).

[23] F. Romero-Ferrero, M. G. Bergomi, R. C. Hinz, F. J. H. Heras, and G. G. de Polavieja, *idtracker.ai: tracking all individuals in small or large collectives of unmarked animals,* Nature Methods **16**, 179 (2019).

[24] G. J. Stephens, B. Johnson-Kerner, W. Bialek, and W. S. Ryu, *Dimensionality and dynamics in the behavior of C. elegans.* PLoS Comput. Biol. **4**, e1000028 (2008).

[25] O. D. Broekmans, J. B. Rodgers, W. S. Ryu, and G. J. Stephens, *Resolving coiled shapes reveals new reorientation behaviors in c. elegans,* eLife **5(e17227)** (2016), 10.7554/eLife.17227.

[26] G. J. Berman, D. M. Choi, W. Bialek, and J. W. Shaevitz, *Mapping the stereotyped behaviour of freely moving fruit flies.* J. Royal Soc. Interface **11**, 1 (2014).

[27] Mathis, Alexander, Mamidanna, Pranav, Cury, Kevin M, Abe, Taiga, Murthy, Venkatesh N, Mathis, Mackenzie Weygandt, and Bethge, Matthias, *DeepLabCut: markerless pose estimation of user-defined body parts with deep learning,* Nature Neuroscience **21**, 1281 (2018).

[28] Pereira, Talmo D, Aldarondo, Diego E, Willmore, Lindsay, Kislin, Mikhail, Wang, Samuel S H, Murthy, Mala, and Shaevitz, Joshua W, *Fast animal pose estimation using deep neural networks,* Nature Methods **16**, 117 (2019).

[29] S. Han, E. Taralova, C. Dupre, and R. Yuste, *Comprehensive machine learning analysis of Hydra behavior reveals a stable basal behavioral repertoire.* eLife **7**, 413 (2018).

[30] A. B. Wiltschko, M. J. Johnson, G. Iurilli, R. E. Peterson, J. M. Katon, S. L. Pashkovski, V. E. Abraira, R. P. Adams, and S. R. Datta, *Mapping Sub-Second Structure in Mouse Behavior,* Neuron **88**, 1121 (2015).

[31] J. M. Graving, D. Chae, H. Naik, L. Li, B. Koger, B. R. Costelloe, and I. D. Couzin, *Deepposekit, a software toolkit for fast and robust animal pose estimation using deep learning,* eLife **8**, e47994 (2019).

[32] H. C. Berg and D. A. Brown, *Chemotaxis in Escherichia coli analysed by Three-dimensional Tracking,* Nature **239**, 500 (1972).

[33] P. S. Lovely and F. W. Dahlquist, *Statistical measures of bacterial motility and chemotaxis.* J. Theor. Biol. **50**, 477 (1975).

[34] M. Schnitzer, S. Block, H. Berg, and E. Purcell, *Strategies for chemotaxis.* Symp. Soc. Gen. Microbio. **46**, 15 (1990).

[35] P. G. De Gennes, *Chemotaxis: The role of internal delays,* Eur. Biophys. J. **33**, 691 (2004).

[36] A. Celani, T. S. Shimizu, and M. Vergassola, *Molecular and Functional Aspects of Bacterial Chemotaxis,* J. Stat. Phys. **144**, 219 (2011).

[37] W. M. Roberts, S. B. Augustine, K. J. Lawton, T. H. Lindsay, T. R. Thiele, E. J. Izquierdo, S. Faumont, R. A. Lindsay, M. C. Britton, N. Pokala, *et al.*, *A stochastic neuronal model predicts random search behaviors at multiple spatial scales in C. elegans,* Elife **5**, e12572 (2016).

[38] M. H. Gail and C. W. Boone, *The locomotion of mouse fibroblasts in tissue culture,* Biophys. J. **10**, 980 (1970).

[39] R. T. Tranquillo, D. A. Lauffenburger, and S. H. Zigmond, *A stochastic model for leukocyte random motility and chemotaxis based on receptor binding fluctuations,* J. Cell Biol. **106**, 303 (1988).

[40] D. Selmeczi, S. Mosler, P. H. Hagedorn, N. B. Larsen, and H. Flyvbjerg, *Cell motility as persistent random motion: theories from experiments,* Biophys. J. **89**, 912 (2005).

[41] P. H. Wu, A. Giri, S. X. Sun, and D. Wirtz, *Three-dimensional cell migration does not follow a random walk,* Proceedings of the National Academy of Sciences of the United States of America **111**, 3949 (2014).

[42] P. E. Smouse, S. Focardi, P. R. Moorcroft, J. G. Kie, J. D. Forester, and J. M. Morales, *Stochastic modelling of animal movement,* Philosophical Transactions of the Royal Society B: Biological Sciences **365**, 2201 (2010).

[43] J. Ben Arous, S. Laffont, and D. Chatenay, *Molecular and sensory basis of a food related two-state behavior in C. elegans,* PLoS ONE **4**, 1 (2009).

[44] J. T. Pierce-Shimomura, T. M. Morse, and S. R. Lockery, *The fundamental role of pirouettes in Caenorhabditis elegans chemotaxis.* J. Neurosci. **19**, 9557 (1999).

[45] M. Fujiwara, P. Sengupta, and S. L. McIntire, *Regulation of body size and behavioral state of C. elegans by sensory perception and the EGL-4 cGMP-dependent protein kinase.* Neuron **36**, 1091 (2002).

[46] T. Gallagher, T. Bjorness, R. Greene, Y. J. You, and L. Avery, *The Geometry of Locomotive Behavioral States in C. elegans,* PLoS ONE **8** (2013), 10.1371/journal.pone.0059865.

[47] V. J. Butler, R. Branicky, E. Yemini, J. F. Liewald, A. Gottschalk, R. A. Kerr, D. B. Chklovskii, and W. R. Schafer, *A consistent muscle activation strategy underlies crawling and swimming in Caenorhabditis elegans,* Journal of the Royal Society Interface **12** (2015), 10.1098/rsif.2014.0963.

[48] G. J. Berman, W. Bialek, and J. W. Shaevitz, *Hierarchy and predictability in Drosophila behavior,* Proceedings of the National Academy of Sciences **104**, 20167 (2016).

[49] A. C. Costa, T. Ahamed, and G. J. Stephens, *Adaptive, locally linear models of complex dynamics,* Proceedings of the National Academy of Sciences of the United States of America **116**, 1501 (2019).

[50] S. Brenner, *The Genetics of Caenorhabditis elegans,* Genetics **77**, 71 (1974).

[51] R. K. Wilson, *How the worm was won: The C. elegans genome sequencing project,* Trends in Genetics **15**, 51 (1999).

[52] J. Sulston, E. Schierenberg, J. White, and J. Thomson, *The embryonic cell lineage of the nematode caenorhabditis elegans,* Developmental Biology **100**, 64 (1983).

[53] J. G. White, E. Southgate, J. N. Thomson, and S. Brenner, *The structure of the nervous system of the nematode Caenorhabditis elegans,* Philosophical Transactions of the Royal Society of London. B, Biological Sciences **314**, 1 (1986).

[54] S. Kato, H. S. Kaplan, T. Schrödel, S. Skora, T. H. Lindsay, E. Yemini, S. Lockery, and M. Zimmer, *Global brain dynamics embed the motor command sequence of Caenorhabditis elegans,* Cell **163**, 1 (2015).

[55] V. Venkatachalam, N. Ji, X. Wang, C. Clark, J. K. Mitchell, M. Klein, C. J. Tabone, J. Florman, H. Ji, J. Greenwood, *et al.*, *Pan-neuronal imaging in roaming caenorhabditis elegans,* Proceedings of the National Academy of Sciences of the United States of America **113**, 1082 (2016).

[56] J. P. Nguyen, F. B. Shipley, A. N. Linder, G. S. Plummer, M. Liu, S. U. Setru, J. W. Shaevitz, and A. M. Leifer, *Whole-brain calcium imaging with cellular resolution in freely behaving caenorhabditis elegans,* Proceedings of the National Academy of Sciences of the United States of America **113**, E1074 (2016).

[57] M. Scholz, A. R. Dinner, E. Levine, and D. Biron, *Stochastic feeding dynamics arise from the need for information and energy,* Proceedings of the National Academy of Sciences of the United States of America , 201703958 (2017).

[58] S. W. Flavell, N. Pokala, E. Z. Macosko, D. R. Albrecht, J. Larsch, and C. I. Bargmann, *Serotonin and the neuropeptide PDF initiate and extend opposing behavioral states in C. elegans,* Cell **154**, 1023 (2013).

[59] J. L. Donnelly, C. M. Clark, A. M. Leifer, J. K. Pirri, M. Haburcak, M. M. Francis, A. D. T. Samuel, and M. J. Alkema, *Monoaminergic Orchestration of Motor Programs in a Complex C. elegans Behavior,* PLoS Biology **11** (2013), 10.1371/journal.pbio.1001529.

[60] S. Stern, C. Kirst, and C. I. Bargmann, *Neuromodulatory Control of Long-Term Behavioral Patterns and Individuality Article Neuromodulatory Control of Long-Term Behavioral Patterns and Individuality across Development Authors,* Cell (2017), 10.1016/j.cell.2017.10.041.

[61] O. Hobert, *Behavioral plasticity in C. elegans: Paradigms, circuits, genes,* Journal of Neurobiology **54**, 203 (2003).

[62] E. Law, W. M. Nuttley, and D. van der Kooy, *Contextual Taste Cues Modulate Olfactory Learining in C. elegans by an Occasion-Setting Mechanism,* Current Biology **14**, 1303 (2004).

[63] M. de Bono and A. Villu Maricq, *Neuronal Substrates of Complex Behaviors in C. Elegans ,* Annual Review of Neuroscience **28**, 451 (2005).

[64] A. J. Chang, N. Chronis, D. S. Karow, M. A. Marletta, and C. I. Bargmann, *A distributed chemosensory circuit for oxygen preference in C. elegans,* PLoS Biology **4**, 1588 (2006).

[65] S. Pereira and D. van der Kooy, *Two forms of learning following training to a single odorant in Caenorhabditis elegans AWC neurons,* Journal of Neuroscience **32**, 9035 (2012).

[66] H. Sasakura and I. Mori, *Behavioral plasticity, learning, and memory in C. elegans,* Curr. Opin. Neurobiol. **23** (2013), 10.1016/j.conb.2012.09.005.

[67] J. M. Gray, J. J. Hill, and C. I. Bargmann, *A circuit for navigation in Caenorhabditis elegans.* Proceedings of the National Academy of Sciences of the United States of America **102**, 3184 (2005).

[68] Y. Iino and K. Yoshida, *Parallel use of two behavioral mechanisms for chemotaxis in Caenorhabditis elegans.* J. Neurosci. **29**, 5370 (2009).

[69] S. Faumont, T. Lindsay, and S. Lockery, *Neuronal microcircuits for decision making in C. elegans.* Curr. Opin. Neurobiol. **22**, 580 (2012).

[70] W. S. Ryu and A. D. T. Samuel, *Thermotaxis in Caenorhabditis elegans analyzed by measuring responses to defined thermal stimuli.* J. Neurosci. **22**, 5727 (2002).

[71] A. J. Calhoun, S. H. Chalasani, and T. O. Sharpee, *Maximally informative foraging by Caenorhabditis elegans.* Elife **3** (2014), 10.7554/eLife.04220.

[72] D. M. Raizen, J. E. Zimmerman, M. H. Maycock, U. D. Ta, Y. J. You, M. V. Sundaram, and A. I. Pack, *Lethargus is a Caenorhabditis elegans sleep-like state,* Nature **451**, 569 (2008).

[73] M. D. Nelson and D. M. Raizen, *A sleep state during C. elegans development,* Current Opinion in Neurobiology **23**, 824 (2013).

[74] S. Iwanir, N. Tramm, S. Nagy, C. Wright, D. Ish, and D. Biron, *The Microarchitecture of C. elegans Behavior during Lethargus: Homeostatic Bout Dynamics, a Typical Body Posture, and Regulation by a Central Neuron,* Sleep **36**, 385 (2013).

[75] A. L. A. Nichols, T. Eichler, R. Latham, and M. Zimmer, *A global brain state underlies C. elegans sleep behavior,* Science **356** (2017), 10.1126/science.aam6851.

[76] N. A. Croll, *Behavioural analysis of nematode movement,* Adv. Parasitol. **13**, 71 (1975).

[77] J. Likitlersuang, G. Stephens, K. Palanski, and W. S. Ryu, *C. elegans tracking and behavioral measurement,* J Vis Exp , e4094 (2012).

[78] J. Gjorgjieva, D. Biron, and G. Haspel, *Neurobiology of caenorhabditis elegans locomotion: Where do we stand?* BioScience **64**, 476 (2014).

[79] N. Cohen and T. Sanders, *Nematode locomotion: dissecting the neuronal–environmental loop,* Curr. Opin. Neurobiol. **25**, 99 (2014).

[80] N. A. Croll, *Behavioural analysis of nematode movement.* Adv. Parasitol. **13**, 71 (1975).

[81] J. Gray and H. W. Lissmann, *The locomotion of nematodes,* J. Exp. Biol. **41**, 135 (1964).

[82] M. Peliti, J. S. Chuang, and S. Shaham, *Directional locomotion of C. elegans in the absence of external stimuli,* PLoS ONE **8** (2013), 10.1371/journal.pone.0078535.

[83] S. J. Helms, W. M. Rozemuller, A. C. Costa, L. Avery, G. J. Stephens, and T. S. Shimizu, *Modelling the ballistic-to-diffusive transition in nematode motility reveals variation in exploratory behaviour across species,* Journal of The Royal Society Interface **16**, 20190174 (2019).

[84] A. C. Costa, D. Jordan, T. Ahamed, and G. J. Stephens, *Bridging time scales in C. elegans behavior,* in prep. (2020).

[85] T. Ahamed, A. C. Costa, and G. J. Stephens, *Capturing the Continuous Complexity of Behavior in C. elegans,* (2019), arXiv:1911.10559 [q-bio.NC] .

2

MODELING THE BALLISTIC-TO-DIFFUSIVE TRANSITION IN NEMATODE MOTILITY REVEALS VARIATION IN EXPLORATORY BEHAVIOR ACROSS SPECIES

2.1. INTRODUCTION

A ubiquitous feature of biological motility is the combination of stereotyped movements in seemingly random sequences. Capturing the essential characteristics of motion thus requires a statistical description, in close analogy to the random-walk formulation of Brownian motion in physics. A canonical example is the "run-and-tumble" behavior of *E. coli* bacteria, in which relatively straight paths (runs) are interspersed by rapid and random reorientation events (tumbles) [2]. The random walk of *E. coli* can thus be characterized by two random variables (run length and tumble angle) and two constant parameters (swimming speed and

Parts of this chapter have been published in the Journal of the Royal Society Interface **16**, (2019), [1]

rotational diffusion coefficient), and detailed studies over decades have yielded mechanistic models that link these key behavioral parameters to the underlying anatomy and physiology [3–6]. Random-walk theory has been fruitfully applied also to studies of eukaryotic cell migration in both two [7–9] and three [10] dimensions.

Can a similar top-down approach be fruitfully applied to more complex organisms–for example, an animal controlled by a neural network? Animal behavior is both astonishing in its diversity and daunting in its complexity, given the inherently high-dimensional space of possible anatomical, physiological, and environmental configurations. It is therefore essential to identify appropriate models and parameterizations to succinctly represent the complex space of behaviors — a non-trivial task that has traditionally relied on the insights of expert biologists. In this study, we ask if one can achieve a similar synthesis by an alternative, physically-motivated approach [11]. We seek a quantitative model with predictive power over behavioral statistics, and yet a parameterization that is simple enough to permit meaningful interpretations of phenotypes in a reduced space of variables. As an example, we focus on the motile behavior of nematodes, which explore space using a combination of random and directed motility driven by undulatory propulsion.

The worm's behavioral repertoire has been extensively studied, and is characterized at finer scales by the propagation of waves across the body that propel the worm forwards and backwards [12–17], and occasional deep turns (omega-turns [15] and delta-turns [18]) or more gradual reorientations ("weathervaning") [19, 20]. Longer time scale exploratory behaviors have also been described, generally in response to external cues, and generally include the modulation of the frequency of different behaviors as well as the transitions between behaviors [16, 19, 21–24], in analogy to the run-and-tumble model of bacterial random walks [2].

Importantly, while these previous studies have illuminated different modes of behavioral control, they were not designed to obtain a predictive model of the trajectory statistics and thus a succinct parameterization of *C. elegans* motility remains an important open problem. A quantitative parameterization capturing the repertoire of *C. elegans*' behavioral phenotypes would facilitate data-driven investigations of behavioral strategies: for example, whether worms demonstrate distinct modes of motility (characterized by correlated changes in parameters) over time, or in re-

sponse to changes in environmental conditions [25–28]. Variation in the obtained parameters among individuals can inform on the distribution of behavioral phenotypes within a population, and reveal evolutionary constraints and trade-offs between strategies represented by distinct parameter sets [29]. *C. elegans* is a member of the *Nematoda* phylum, one of the largest and most diverse phylogenetic groups of species [30, 31]. Despite the diversity of ecological niches these animals inhabit [30], comparisons of nematode body plans have revealed a remarkable degree of conservation, even down to the level of individual neurons [32]. This combination of highly conserved anatomy and ecological diversity makes nematode motility a compelling case for studies of behavioral phenotypes. Anatomical conservation suggests it might be possible to describe the behavior of diverse nematodes by a common model, and identifying the manner in which existing natural variation is distributed across the parameter space of the model could reveal distinct motility strategies resulting from optimization under different environmental conditions.

In this study, we develop a simple random walk model describing the translational movements of a variety of nematode species, freely-moving on a two-dimensional agar surface. In addition to providing a quantitative and predictive measure of trajectory dynamics, the parameters of our model define a space of possible behaviors. Variation within such a space can occur due to changes in individual behavior over time (reflecting temporal variation in the underlying sensorimotor physiology, or "mood"), differences in behavior among individuals (reflecting stable differences in physiology, or "personality") and differences between strains and species (reflecting cumulative effects of natural selection). By quantitative analyses of such patterns of variation, we seek to identify simple, organizing principles underlying behavior.

2.2. RESULTS

2.2.1. NEMATODES PERFORM RANDOM WALKS OFF-FOOD WITH A BROAD RANGE OF DIFFUSIVITIES ACROSS STRAINS

In order to identify conserved and divergent aspects of motility strategies, we sampled motile behavior over a broad evolutionary range. We selected a phylogenetically diverse collection of nematodes with an increased sampling density closer to the laboratory strain *C. elegans* (Fig-

ure 2.1A, see also the Supplementary Information in [1]). To sample individual variation, we recorded the motility of up to 20 well-fed individuals per strain and each individual for 30 minutes on a food-free agar plate at 11.5 Hz with a resolution of 12.5 µm/px (see Methods).

We measured the centroid position ($\vec{x}(t)$) and calculated the centroid velocity ($\vec{v}(t)$), using image analysis techniques (see Methods). There was considerable variation in the spatial extent and degree of turning visible in the trajectories both within and across strains (Figure 2.1A, see also Fig. S2 in [1]).

As previously seen in *C. elegans* [33], the measured mean-squared displacement,

$$\langle [\Delta x(\tau)]^2 \rangle \equiv \langle |\vec{x}(t+\tau) - \vec{x}(t)|^2 \rangle, \tag{2.1}$$

revealed a transition from ballistic to diffusive motion within a 100 s timescale (Figure 2.1B, see also Fig. S3 in [1]). Over short times, the worm's path was relatively straight, with the mean-squared displacement scaling quadratically with the time lag τ and speed s as $\langle s^2 \rangle \tau^2$ (*i.e.* a log-log slope of 2). Over longer times, the slope decreased with τ reflecting the randomization of orientation characteristic of diffusion, and an effective diffusivity D_{eff} was extracted by fits to $\langle [\Delta x(\tau)]^2 \rangle = 4 D_{\text{eff}} \tau$ (see SI). Note that on the time scales at which the worms start encountering the walls of the observation arena, the slope of the mean-squared displacement decreased yet further, which has been shown to be a property of confined random walks [34]. Nonetheless, we have confirmed that the decay of the velocity autocorrelation function is not significantly affected by the confinement (see Figure S1 in [1]) and is consistent with a ballistic to diffusive transition as seen in [33]. Given how challenging it is to measure diffusive regimes experimentally [35], it should be noted that this is merely a high-level description of the dispersion of worms on the plate, and it remains to be shown whether worms exhibit pure diffusive behavior. Nonetheless, we use D_{eff} as a rough measure of the spatial extent of the worms' movements on the plate. This analysis reveals that in these 30-minute trajectories worms vary by nearly an order of magnitude in speed and two orders of magnitude in diffusivity (Figure 2.1C, see also Tables S1 & S2 in [1]).

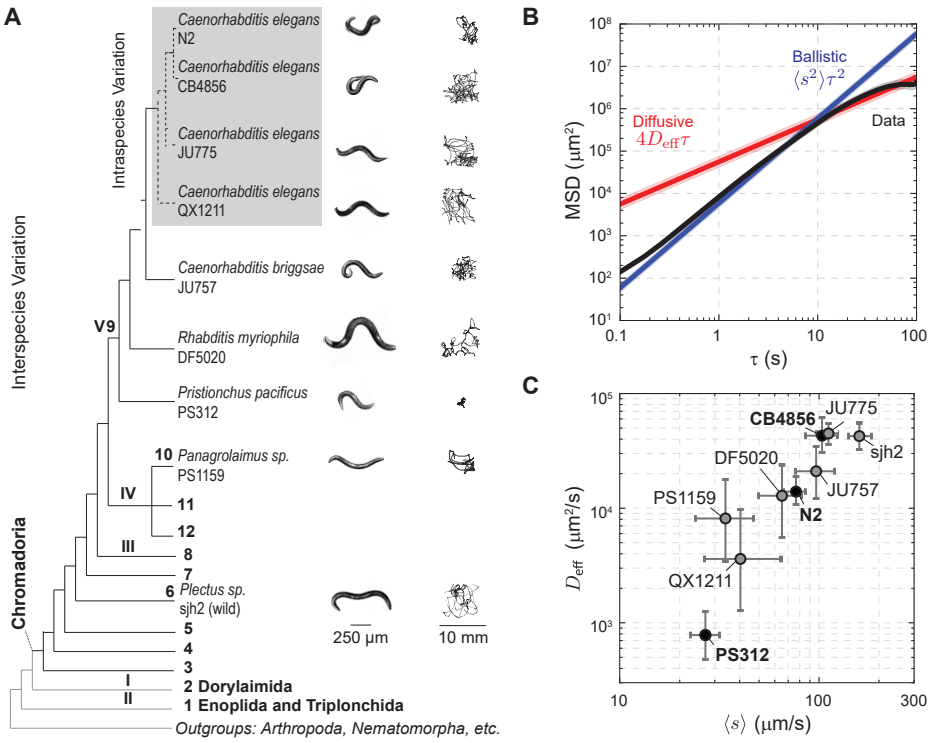

Figure 2.1: Nematodes perform random walks off-food with a mean speed and effective diffusivity that varies across strains. (A) Phylogenetic tree with the strains used in this study. The bold numbers are the major clades of *Nematoda*. The gray box indicates genetically distinct wild isolates of *C. elegans*. A representative worm image and 30 minute trajectory are shown to the right. (B) The average mean-squared displacement, MSD, across N2 individuals is shown in black. For comparison, we show the MSD expected from ballistic (blue) and diffusive (red) dynamics. The motility transitions from a ballistic to diffusive regime within a time scale of tens of seconds. Shaded regions indicate a 95% confidence interval. (C) Mean speed $\langle s \rangle$ and effective diffusivity D_{eff} (mean and 95% confidence intervals) for each strain, calculated from fits of the mean-squared displacement as in B. Across strains, both $\langle s \rangle$ and D_{eff} vary by orders of magnitude.

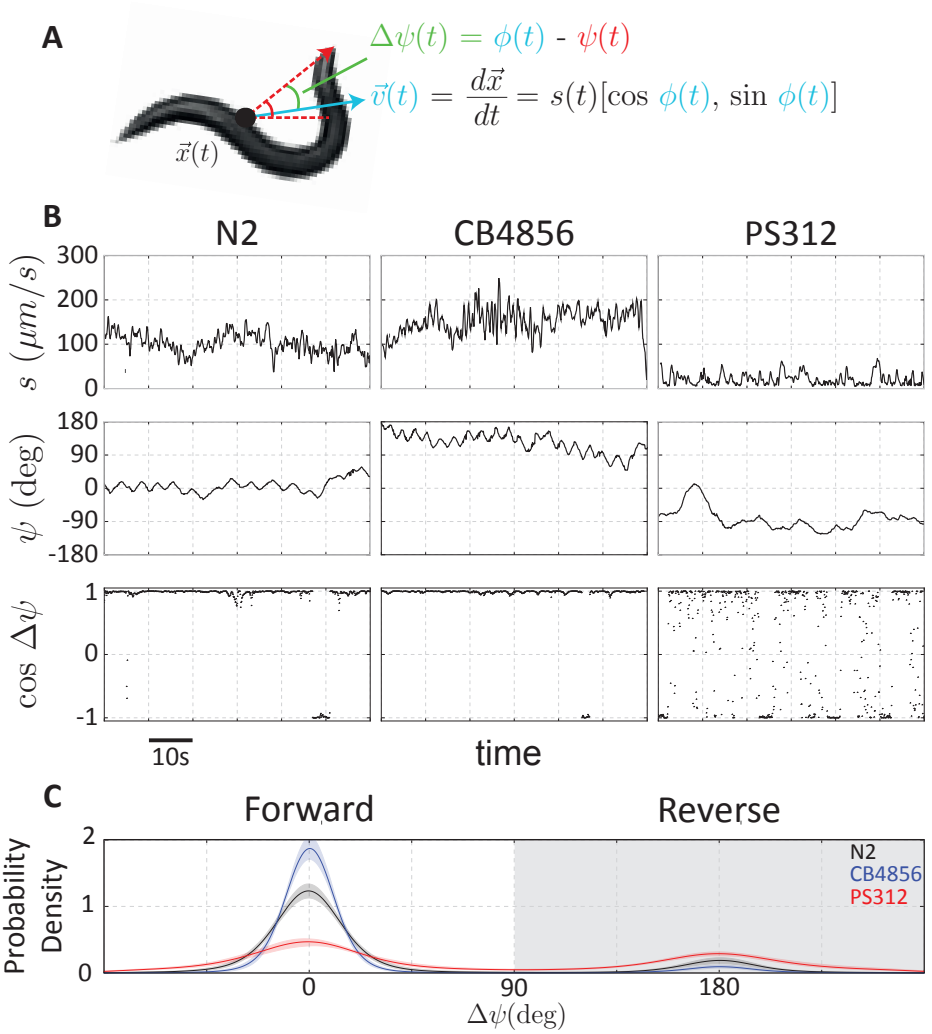

Figure 2.2: The random walk of nematodes is composed of speed, turning, and reversal dynamics. (A) We describe the motility of the worm by the time-varying quantities $s(t)$ (speed; black), $\psi(t)$ (orientation; red), and $\Delta\psi(t)$ (alignment; green) which measures the difference between the alignment of the velocity $\phi(t)$ (blue) and $\psi(t)$. (B) One minute examples of speed, orientation, and velocity alignment time series for individuals from three exemplar strains. (C) The probability distribution of $\Delta\psi(t)$ reveals bimodality corresponding to forward and reverse motion. Shaded regions indicate a 95% confidence interval.

2.2.2. THE RANDOM WALK OF NEMATODES CAN BE DECOMPOSED INTO SPEED, TURNING AND REVERSAL DYNAMICS

The broad range of observed speeds and diffusivities suggest that these diverse nematodes have evolved a variety of strategies for spatial exploration. To gain further insights into the manner in which such contrasting behaviors are implemented by each strain, we sought to extract a minimal model of the nematodes' random walk by further decomposing the trajectory statistics of all nine measured strains. In this and the following three sections, we illustrate our analysis and model development with data from three contrasting strains: CB4856 and PS312, which demonstrated two of the most extreme phenotypes, and the canonical laboratory strain N2 (see [1] for equivalent data for all strains).

The translational motion of the worm can be described by the time-varying centroid velocity $\vec{v}(t)$ which can in turn be decomposed into speed $s(t)$ and direction of motion (hereafter referred to as its "bearing") $\phi(t)$:

$$\vec{v}(t) = \frac{d\vec{x}(t)}{dt} = s(t)\left[\cos\phi(t), \sin\phi(t)\right] \tag{2.2}$$

To account for head-tail asymmetry in the worm's anatomy, we additionally define the body orientation ($\psi(t)$; hereafter referred to simply as "orientation") by the angle of the vector connecting the worm's centroid to the head (Figure 2.2A). The centroid bearing is related to this orientation of the worm by

$$\phi(t) = \psi(t) + \Delta\psi(t) \tag{2.3}$$

where the difference $\Delta\psi(t)$ is a measure of the alignment of the direction of movement with the worm's body orientation (hereafter referred to simply as "alignment"). We found for all strains that the distribution of $\Delta\psi(t)$ was bimodal with peaks at 0°and 180°(Figure 2.2C, see also Fig. S7 in [1]). These match the forward and reverse states of motion described in *C. elegans* [14, 15].

Each of the three components of the worm's motility (speed, orientation, and alignment) varied considerably over time and in qualitatively different ways between strains (Figure 2.2B). For example, the three strains shown in Figure 2.2B differed not only in their average speed, but also in the amplitude and timescale of fluctuations about the average speed. Similarly, the statistics of orientation fluctuations about the drifting mean

also differed visibly between strains. Finally, transitions between forward and reverse runs were far more frequent in PS312 as compared to N2 and CB4856. Given the apparently random manner in which these motility components varied over time, we proceeded to analyze the dynamics of each of these three components as a stochastic process.

2.2.3. SPEED DYNAMICS

Speed control has not been extensively studied in *C. elegans*, but it is known that worms move with a characteristic speed that is influenced by stimuli [22]. When intervals corresponding to transitions between forward and reverse runs were excluded from the time series, we found that the autocovariance in speed fluctuations decayed exponentially over a few seconds (Figure 2.3A, see Fig. S5 in [1] for data on other strains), a timescale similar to the period of the propulsive body wave. These dynamics are naturally captured by an Ornstein-Uhlenbeck process [36], which describes random fluctuations arising from white noise (increments of a diffusive Wiener process, dW_t [36]) with magnitude $\sqrt{2D_s}$ that relax with timescale τ_s back to an average value, $\mu_s = \langle s \rangle$:

$$ds(t) = \tau_s^{-1}\left[\mu_s - s(t)\right]dt + \sqrt{2D_s}dW_t \tag{2.4}$$

Numerical integration of this equation closely reproduced the observed speed distributions during runs (Figure 2.3A-inset. see Fig. S5 in [1] for data on other strains.).

2.2.4. DIFFUSIVE TURNING WITH DRIFT

The orientation $\psi(t)$ captures turning dynamics that are independent of abrupt changes in bearing $\phi(t)$ due to reversals. To change orientation, *C. elegans* executes a combination of large ventrally-biased Ω and δ-turns turns [14, 18, 37] and gradual "weathervaning" [19], both of which contribute to randomization of orientation over time. This random walk in orientation was not purely diffusive: the orientation correlation $C_\psi(\tau) = \langle \cos\left[\psi(t+\tau) - \psi(t)\right]\rangle$ does not decay exponentially (Figures 2.3B-inset, see Fig. S6B in [1] for data on other strains), and the mean-squared angular displacement, $\mathrm{MSAD}(\tau) = \langle[\psi(t+\tau) - \psi(t)]^2\rangle$, increases nonlinearly with time (Figures 2.3B, see Fig. S6A in [1] for data on other strains).

We found that this nonlinear MSAD of $\psi(t)$ could be well approximated by a quadratic function of the time delay τ: $\mathrm{MSAD}(\tau) = k_{\psi\mathrm{rms}}^2\tau^2 +$

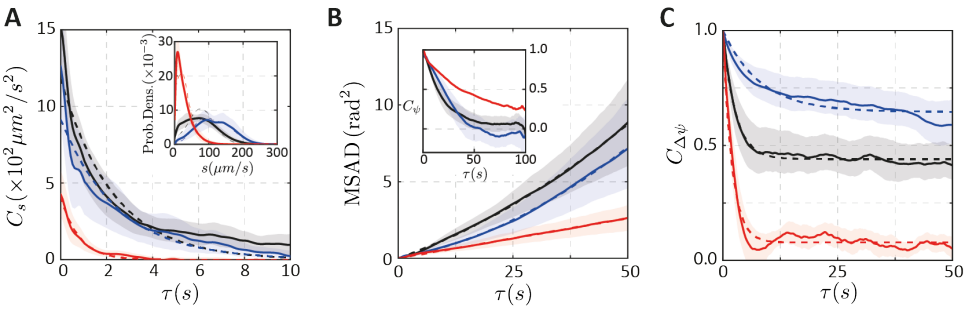

Figure 2.3: Statistical characterization of the motility dynamics. (A) The autocovariance of the speed indicated that fluctuations decayed exponentially over a few seconds. (A, inset) Speed distributions for three exemplar strains. Dashed lines result from numerical integration of eq. (2.4). (B) The mean-squared angular displacement (MSAD) increased quadratically. (B, inset) The orientation autocorrelation function did not decay exponentially, with some worms demonstrating significant undershoots below zero. (C) The velocity alignment autocorrelation decayed exponentially over tens of seconds to a positive constant. In each plot, the ensemble average for all individuals from the strains are shown with solid lines and trends are shown with dashed liens. Shaded regions indicate a 95% confidence interval.

$2D_\psi\tau$, corresponding to a diffusion-and-drift model with root-mean-square drift magnitude $k_{\psi\mathrm{rms}}$ and angular diffusion coefficient D_ψ (see Methods for derivation). A non-zero drift magnitude $k_{\psi\mathrm{rms}} \neq 0$ indicates that in addition to purely random (diffusive) changes in orientation, there is an underlying bias (i.e. directional persistence) in the worms' turning over 100 s windows, consistent with previous studies in larger arenas [20].

These observations lead to a simple model for the orientation dynamics that combines drift (approximated as a deterministic linear process over a 100 s window) with stochastic diffusion:

$$d\psi(t) = k_\psi dt + \sqrt{2D_\psi} dW_t, \tag{2.5}$$

where we set the drift magnitude $k_\psi = k_{\psi\mathrm{rms}}$ and dW_t represents increments of a Wiener process [36].

We note that while this model described well the orientation dynamics within 100 s windows, over longer timescales additional dynamics may be relevant. The magnitude of k_ψ in our data ($\sim 1\,^\circ\mathrm{s}^{-1}$) was similar to that of weathervaning excursions reported for *C. elegans* navigating in salt gradients [19].

2.2.5. FORWARD AND REVERSE RUNS

The observation that motion during runs switched abruptly between forward and reverse states (with $\Delta\psi \approx \{0°, 180°\}$, respectively; Figures 2.2B,C, see Fig. S7A in [1] for data on other strains) suggested that reversals could be described as a discrete stochastic process. The manner in which reversals contribute to randomization of bearing over a time lag τ is captured by the autocorrelation function of $\Delta\psi(t)$, $C_{\Delta\psi}(\tau) \equiv \langle\cos\big(\Delta\psi(t+\tau) - \Delta\psi(t)\big)\rangle$. We found that $C_{\Delta\psi}(\tau)$ decayed nearly exponentially to a non-zero baseline (Figure 2.3C, see Fig. S7A in [1] for data on other strains). This is the predicted behavior for the autocorrelation function of the simplest of two-state processes (a "random telegraph process"):

$$P(T_{\text{fwd}} > t) = \exp(-t/\tau_{\text{fwd}}) \tag{2.6}$$

$$P(T_{\text{rev}} > t) = \exp(-t/\tau_{\text{rev}}), \tag{2.7}$$

in which the distribution of forward and reverse run intervals (T_{fwd} and T_{rev}) are completely determined by a single time constant (τ_{fwd} and τ_{rev}, respectively). The random telegraph process yields an autocorrelation function that decays exponentially as $C_{\Delta\psi}(\tau) = C_{\Delta\psi}(\infty) + \big(1 - C_{\Delta\psi}(\infty)\big)\, e^{-\tau/\tau_{RT}}$ to a minimum value $C_{\Delta\psi}(\infty) \equiv ((\tau_{\text{fwd}} - \tau_{\text{rev}})/(\tau_{\text{rev}} + \tau_{\text{fwd}}))^2$ with a timescale $\tau_{RT} \equiv \left(\tau_{\text{fwd}}^{-1} + \tau_{\text{rev}}^{-1}\right)^{-1}$ [38]. Results obtained from fitting the autocorrelation function are consistent with those obtained from the distribution of time intervals between detected switching events (Fig. S7 in [1]). Note, however, that for some strains the run length distributions exhibits heavy-tails not captured by a simple random telegraph process, and that autocorrelation functions exhibit slight offsets around the $\sim 10\,\text{s}$ time scale, with the data exhibiting larger correlations that those predicted by this simple model. Nonetheless, the random-telegraph process is a good approximation of the overall statistics of the dynamics. In principle, the forward and reverse states could be characterized by differences in motility parameters of our model other than these transition times, as forward and reverse motion are driven by distinct command interneurons in *C. elegans* [39, 40]. However, we found that run speeds were nearly identical between forward and reverse runs (see Fig. S8 in [1]). While we expect that this symmetry will be broken under some specific conditions, such as the escape response [41], the strong speed correlation between the two states motivates the assumption, adopted in our model, that reversals change

only the bearing (by 180°) and the propensity to reverse direction, represented in our model by the time constants τ_{fwd} and τ_{rev}.

2.2.6. A MODEL WITH INDEPENDENT SPEED, TURNING AND REVERSALS CAPTURES THE BALLISTIC-TO-DIFFUSIVE TRANSITION IN NEMATODE MOTILITY

Given that the dynamics of the worm's speed, turning and reversals could be approximated by simple stochastic processes, we asked whether combining them as independent components in a model of the worms' random walk could sufficiently describe the observed motility statistics (Figure 2.4A). We simulated trajectories of worms by numerically integrating equations (2.4)-(2.7) for the speed, orientation, and reversal dynamics, respectively, which yields the worm's velocity dynamics through equations (2.2) and (2.3), with $\Delta\psi(t)$ equal to 0° during forward runs and 180° during reverse runs. Simulations of this model using parameters fit to individual worms produced trajectories that qualitatively resembled real trajectories and varied considerably in their spatial extent (Figure 2.4B).

Next, we quantitatively assessed the performance of the model in reproducing the statistics of the observed trajectories over the time scale of 100 s, within which all strains completed the transition from ballistic to diffusive motion (Figure 2.4C). We found that the model based on independent speed, turning and reversal dynamics closely reproduced not only the diffusivity of each strain but also the time evolution of the mean-squared displacement ($\langle[\Delta x(\tau)]^2\rangle$) across the ballistic-to-diffusive transition (Figure 2.4C, top). A closer inspection of the dynamics across this transition is possible by examining the velocity autocorrelation function ($C_{\vec{v}}(\tau)$), the time integral of which determines the slope of the mean-squared displacement through $(d/d\tau)\langle[\Delta x(\tau)]^2\rangle = 2\int_0^\tau d\tau' C_{\vec{v}}(\tau')$, a variant of the Green-Kubo relation [42, 43]. The transition from ballistic to diffusive motion is characterized by the manner in which the normalized velocity autocorrelation $C_{\vec{v}}(\tau)/C_{\vec{v}}(0)$ decays over the time lag τ from unity (at $\tau = 0$) to zero (as $\tau \to \infty$). We found that $C_{\vec{v}}(\tau)$ varied considerably across strains, not only in the overall ballistic-to-diffusive transition time, but also in the more detailed dynamics of the autocorrelation decay over time (Figure 2.4C, middle). Salient features, such as the transition time, of the measured velocity autocorrelation functions $C_{\vec{v},\text{obs}}$ were reproduced closely by the simulated velocity autocorrelation functions $C_{\vec{v},\text{model}}$, but

there were also subtle deviations in the detailed dynamics for a number of strains.

Given our model's simplifying assumption that dynamics for $s(t)$, $\psi(t)$, and $\Delta\psi(t)$ are independent stochastic processes, we asked whether the remaining discrepancies between the simulated and measured velocity autocorrelation dynamics could be explained by violations of this assumption of independence. As a model-free assessment of the degree of non-independence, we first calculated the predicted velocity autocorrelation for the case that the dynamics of all three components are independent, $C_{\vec{v},\mathrm{indep}}(\tau) = C_s(\tau)C_\psi(\tau)C_{\Delta\psi}(\tau)$, where $C_s(\tau)$, $C_\psi(\tau)$, and $C_{\Delta\psi}(\tau)$ are the autocorrelation functions of the measured data for each of the components (see Supporting Information for derivation). We then compared the differences $C_{\vec{v},\mathrm{obs}} - C_{\vec{v},\mathrm{indep}}$ (blue curve in Figure 2.4C, bottom) and $C_{\vec{v},\mathrm{obs}} - C_{\vec{v},\mathrm{model}}$ (red curve in Figure 2.4C, bottom). Indeed, there were subtle differences both on shorter (~1 s) and longer timescales (~10 s). However, these errors for the simulated model were very similar to, or less than, those for the model-free prediction from the data under the assumption of independence (*i.e.*, $C_{\vec{v},\mathrm{obs}} - C_{\vec{v},\mathrm{model}} \lesssim C_{\vec{v},\mathrm{obs}} - C_{\vec{v},\mathrm{indep}}$). These results demonstrate that modeling $s(t)$, $\psi(t)$, and $\Delta\psi(t)$ as independent stochastic processes provides a very good approximation to trajectory statistics across the ballistic-to-diffusive transition. The relatively subtle differences between the data and model arise primarily in instances where this assumption of independence between the three motility components breaks down. Consistent with these conclusions, inspection of cross-correlation functions computed from the data revealed that correlations between $s(t)$, $\psi(t)$, and $\Delta\psi(t)$ are largely absent, with only weak correlations between speed (s) and reversals ($\Delta\psi$) in a subset of strains (see Fig. S9 in [1]).

2.2.7. VARIATION OF EXPLORATORY BEHAVIOR ACROSS SPECIES

The results presented in the previous sections demonstrate that a random-walk model with seven parameters describing independent speed, turning and reversal dynamics, provides a good approximation of the worms' motile behavior over the ~100 s timescale spanning the ballistic-to-diffusive transition. The model parameters thus define a seven-dimensional space of motility phenotypes in which behavioral variation across strains and species can be examined. If components of behavior were physiologically regulated or evolutionarily selected for in a coordinated manner, we

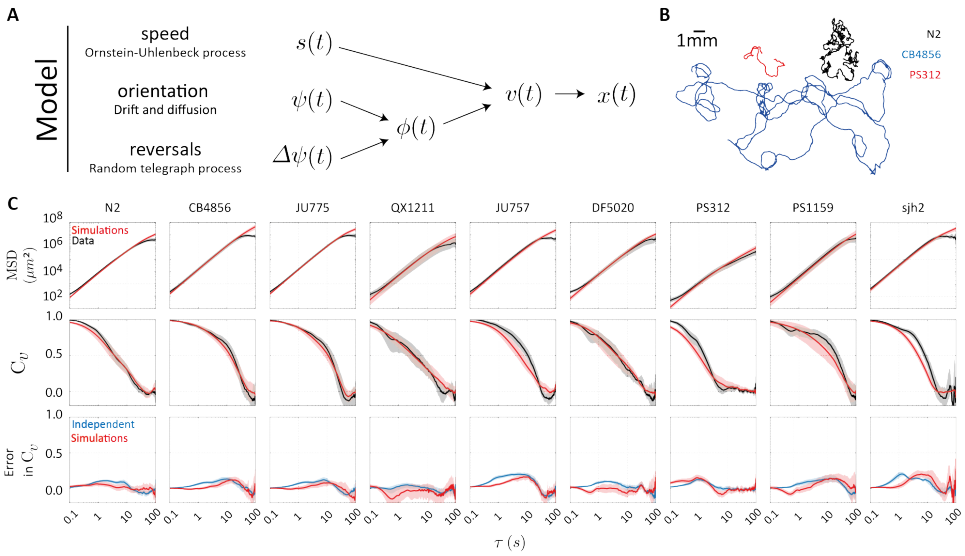

Figure 2.4: A model consisting of independent speed (Ornstein-Uhlenbeck process), turning (drift and diffusion), and reversal dynamics (random telegraph process) quantitatively captures nematode motility. (A) Summary of the model. (B) Simulated trajectories for the three exemplar strains. (C) Statistical comparison of the data (black) and simulations (red), ensemble averaged across individuals for each strain. (C, top) The mean-squared displacement (MSD) was closely reproduced in all cases. (C, middle) The normalized velocity autocorrelation, $C_{\vec{v}}(\tau)/C_{\vec{v}}(0)$, (VACF) was less well captured. (C, bottom) The relatively small errors in the simulated VACF (red) can be traced to the assumption of independence in the dynamics of the speed, orientation, and velocity alignment (blue). Shaded regions indicate a 95% confidence interval.

would expect to find correlated patterns in the variation of these traits.

We fit our model to the trajectory statistics of each individual worm and built a phenotype matrix of 106 worms x 7 behavioral parameters. The correlation matrix for these 7 parameters demonstrates that the strongest correlation were the forward and reverse state lifetimes (τ_{fwd}, τ_{rev}), followed by those describing speed and forward state life times (μ_s, τ_{fwd}). More broadly, there were extensive correlations among the model parameters, not only within the parameters of each motility component (speed, orientation, reversals) but also between those of different components.

We looked for dominant patterns in the correlations using principal component analysis [44] (Figure 2.5B), uncovering a single dominant mode of correlated variation (Figure 2.5B, left). This principal mode (mode 1), capturing nearly 40% of the total variation, described significant correlations among all the parameters except for D_s and D_ψ (Figure 2.5B, right, see also Table S5 in [1]).

We used numerical simulations to determine the effects on motile behavior of varying parameters along the principal mode. The measured trajectory phenotypes projected onto this mode in the range $\{-4, 2\}$ centered about the average phenotype located at the origin, and we performed simulations for parameter sets evenly sampled along this range. These largely reproduced the observed variation in the measured diffusivities D_{eff} as a function of the projection along the first mode. The agreement was particularly good at higher values (> -1) of the mode projection, but at lower values we noted a tendency for the D_{eff} from simulations to exceed that of the data. The latter discrepancy can be explained by elements of behavior not captured by our model (see Discussion). Nevertheless, as illustrated by simulated trajectories (Figure 2.5C, bottom), trajectories became more expansive as the mode projection increased, as did D_{eff} by nearly two orders of magnitude over the tested range. This suggested that the principal mode indicates exploratory propensity (Figure 2.5C), and we confirmed that it is indeed more strongly associated with changes in D_{eff} than expected for randomly generated parameter sets (see Fig. S10 in [1]). Interestingly, this mode of variation we found across individual phenotypes is reminiscent of "roaming" and "dwelling" behavioral variability that has been shown within individuals across time, in *C. elegans* [25, 27] as well as other organisms [45, 46].

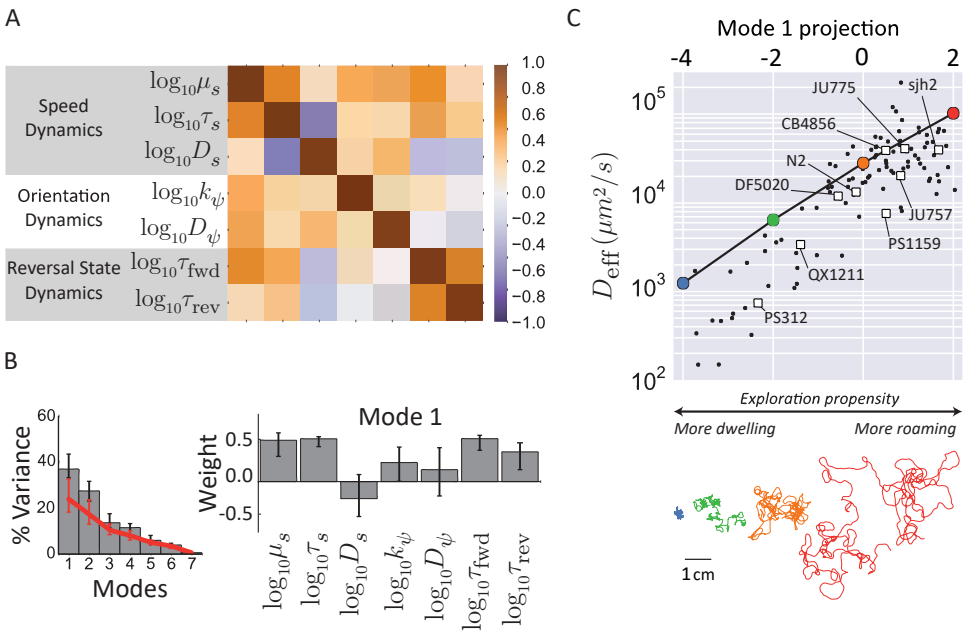

Figure 2.5: Motility parameters co-vary along an axis controlling exploratory behavior. (A) Correlation matrix of the behavioral parameters across the whole dataset. (B, left) Fraction of variance captured by each mode and the amount expected for an uncorrelated dataset (red line) (B, right) The loadings on the top eigenvector. (C) The effective diffusivity (top) and a 30 minute trajectory (bottom, colors match points on graph) from simulations in which the loading on the top eigenvector was varied; the principal mode can be used as an effective phenotype from a more *dwelling* to a more *roaming* behavior. The projections and effective diffusivity of the measured trajectories are shown as black points, and the average of each strain is shown as a square.

2.2.8. SPECIALIZED AND DIVERSIFIED BEHAVIORAL STRATEGIES ACROSS STRAINS

The principal behavioral mode discussed in the preceding section was identified by analyzing variation across all individual worms measured in this study, coming from diverse strains and species that differ in their average behavior (see Tables S2 - S4 in [1]). How does the variability among individuals of a given strain compare to differences between the average phenotypes of strains/species? On the one hand, each strain might be highly "specialized", with relatively small variation within strains as compared to that across strains. On the other hand, strains might implement "diversified" strategies in which genetically identical worms vary strongly in their behavior. To address these two possibilities, we analyzed the distribution of individual phenotypes within each strain, as well as that of the set of averaged species phenotypes.

For each measured individual, we computed the projection of its motility parameter set along the principal behavioral mode and estimated strain-specific distributions of this reduced phenotype (Figure 2.6, Table S6 in [1]). In principle, any detail in the shape of these distributions could be relevant for evolutionary fitness, but here we focused our analysis on the mean and standard deviation, given the moderate sampling density (≤ 20 individuals per strain). Further, we computed the principal-mode projection of the average phenotype of each species to define an interspecies phenotype distribution (Figure 2.6).

Strains varied considerably in both the position and breadth of their phenotypic distributions along the principal behavioral mode. Remarkably, variation across individuals within each strain was comparable in magnitude to that for the set of average phenotypes across species (Figure 2.6). Some strains were specialized towards roaming or dwelling behavior, such as CB4856 and PS312, respectively, with a strong bias in their behavior and comparatively low individual variability. Others, such as QX1211 and PS1159, appeared more diversified with an intermediate average phenotype and higher individual variability. These considerable differences in phenotype distributions across strains reveal the evolutionary flexibility of population-level heterogeneity in nematodes, and suggest a possible bet-hedging mechanism for achieving optimal fitness in variable environments [47, 48].

In assessing such variability of phenotypes, it is essential to ask how

uncertainty in the determined parameters (obtained from model fits) contribute to the observed variability in phenotypes. We therefore computed the contribution of uncertainties in the individual phenotype determination by bootstrap resampling of the 100 s windows of each individual's recorded trajectory (see Methods). The uncertainties thus computed reflect contributions from both parameter uncertainties in curve fitting of data, as well as temporal variability in an individual's parameters over timescales longer than the window size (100 s). With the exception of two strains (sjh2 and CB4856), this measure of uncertainty accounted for less than half of the individual variation within each strain (Figure 2.6B). These findings support the view that the phenotypic variation estimated in the current analysis largely represented stable differences in individual behavior.

2.3. DISCUSSION

We have presented a comparative quantitative analysis of motile behavior across a broad range of strains and species of the nematode phylum, ranging from the lab strain *C. elegans* N2 to *Plectus* sjh2 at the base of the chromadorean nematode lineage. Despite the vast evolutionary distances spanned by strains in this collection [49], we found that a behavioral model described by only seven parameters could account for much of the diversity of the worms' translational movement across the ~100 s timescale spanning the ballistic-to-diffusive transition. This simple model provides a basis for future studies aiming to capture more detailed aspects of nematode behavior, or to connect sensory modulation of behavior to the underlying physiology. More generally, our results demonstrate how quantitative comparisons of behavioral dynamics across species can provide insights regarding the design of behavioral strategies.

2.3.1. THE MINIMAL MODEL: WHAT DOES IT CAPTURE, AND WHAT DOES IT MISS?

We focused on a high-level output of behavior — translational and orientational trajectory dynamics — and sought to build the simplest possible quantitative model that could capture the observed behavioral statistics. We found that a model with only three independent components — (1) speed fluctuations that relax to a set point on a timescale of a few sec-

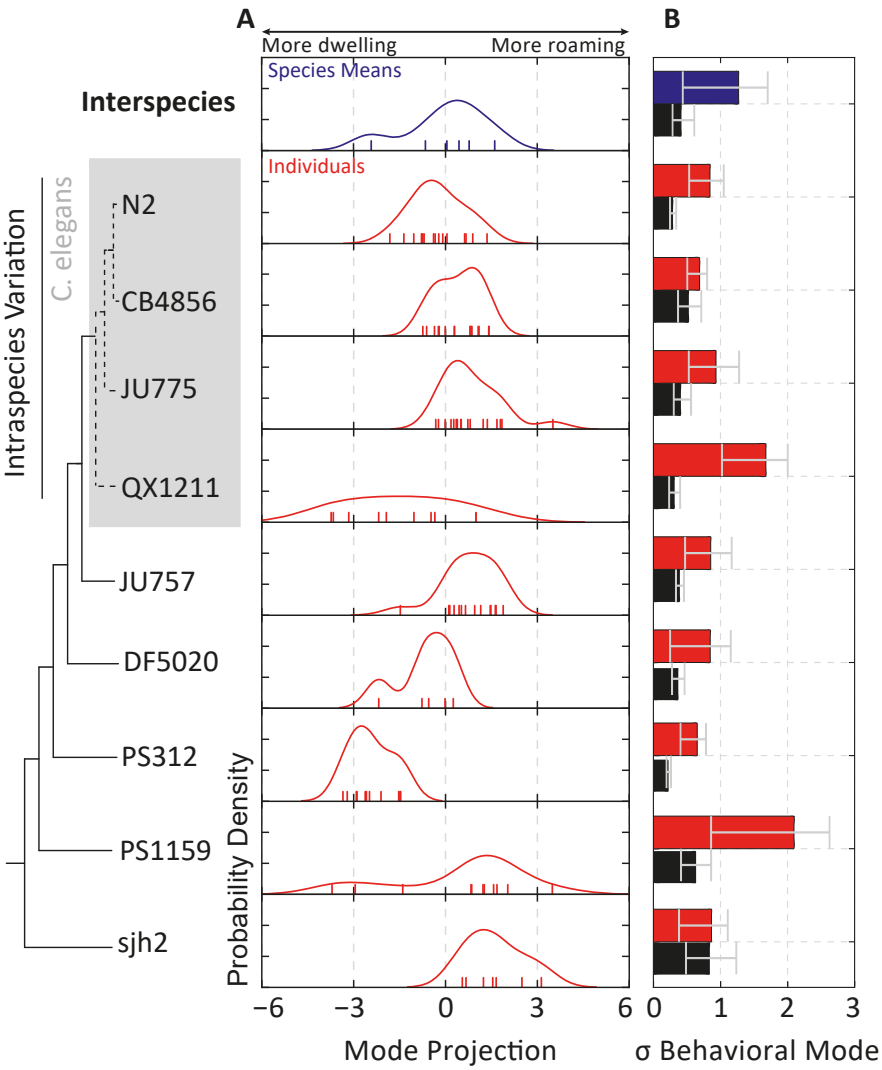

Figure 2.6: Variation of model parameters reveal specialized and diversified behavioral strategies across strains. (A) Distribution of the average phenotype for each species (*interspecies* variation, blue) or individuals within a strain (red). Note that the variation of individual phenotypes in some strains (e.g. QX1211, PS1159) is comparable in magnitude to that of interspecies variation. Observations are indicated with colored ticks. (B) Comparison of the width of the phenotype distributions (colored bars), quantified as the bootstrapped standard deviation of the data points in (A), with the uncertainty in the determination of the phenotype (black bars), quantified as the standard deviation of individual phenotype determinations over bootstrapped 100 s time windows. Error bars correspond to 95% confidence intervals across bootstrap samples.

onds, (2) orientation fluctuations with drift, and (3) stochastic switching between forward and reverse states of motion — describes well, overall, the trajectory statistics of all tested nematode species across the ballistic-to-diffusive transition (Figure 2.4).

Notably, we have not included explicit representations of some reorientation mechanisms that have been studied in the past, such as the deep turns (omega- and delta-turns) [14, 18], or the combination of such turns with reversals (pirouettes) [21]. In our data, we find that the timing of the initiation and termination of reversals, which would both count as runs in the pirouette description, follow exponential distributions with similar time constants as previously reported for the pirouette run distribution. While omega and delta turns must indeed be mechanistically distinct from gradual turns, we have chosen here not to explicitly model their occurrence since orientation changes in our trajectory data were adequately described by a continuous diffusion-drift process (Figures 2.3B, S6A). It is possible, however, that explicit representations of pirouettes and/or omega turns would be important in other experimental scenarios, e.g. those that include navigation in the presence of gradient stimuli.

In our model, "roaming" and "dwelling" were not assigned discrete behavioral states (as was done *e.g.* in [25–27]), but instead emerged as a continuous pattern of variation among motility parameters describing the worm's random walk. However, robust extraction of motility parameters required pre-filtering of trajectory data that likely biased them towards more "roaming" phenotypes (see SI), which we believe account for the noted tendency of model simulations to overestimate D_{eff} that was more pronounced for trajectories at the "dwelling" end of the spectrum (Figure 2.5C).

In its current form, our simple model does not account for possible correlations between the dynamics of the three motility components (speed, orientation, and reversals). Indeed, at least weak correlations do exist between the components (see Fig. S9 in [1]). Comparisons of simulated versus measured trajectories demonstrated that the effects of such correlations on the motility statistics are small but detectable (Figure 2.4C). The differences were most significant for the velocity-autocorrelation dynamics on a ~10 s timescale, and were similar to those for model-free predictions obtained by combining component-wise correlation functions under the assumption of independence. Discrepancies on this intermediate

timescale occurred most often in fast-moving strains that frequently approached the repellent boundary. Therefore, we suspect that the discrepancy arises from a stereotyped sequence, such as the escape response[41], that introduces temporal correlations between speed changes, turning, and reversals.

While here we have focused on the transition to diffusive motion, some recent experiments suggest that *C. elegans* might engage in superdiffusive behavior on timescales longer than 100 s [20, 28]. Superdiffusive behavior could arise from nonstationarities in motile behavior, such as the roaming/dwelling transitions on timescales of several minutes [27]. Another mechanism for superdiffusion is *directed* motility [20] in response to external stimuli such as chemical or thermal gradients. In such environments, nematodes are known to use at least two distinct mechanisms for navigation [19, 21] and the model here could be extended by studying the dependence of motility parameters on environmental statistics.

Information about the body shape can be incorporated to build a more complete behavioural model that also includes dynamics hidden by centroid behaviour [33, 50]. Indeed, work by Brown et al. showed that a rich repertoire of dynamics can be identified as temporal "motifs" in the postural time series of *C. elegans* and used to classify mutants with high discriminatory power[51]. We have found that all of the species tested here can also be described with a common set of postural modes (not shown), suggesting future directions on the evolutionary space of postural dynamics.

2.3.2. THE EXPLORATORY BEHAVIORAL MODE: VARIABILITY AND ITS PHYSIOLOGICAL BASIS

While we found that a single behavioral model could be used to characterize nematode motility across the chromadorean lineage, the parameters of the model varied extensively from strain to strain. Quantitatively, about 37% of the variation corresponded to a correlated change in the parameters underlying the timing of forward and reverse runs and the dynamics controlling speed and turning (Figure 2.4B). We find that this principal mode of variation is associated with strong changes in exploratory propensity, as characterized by D_{eff} (Figure 2.5C). This pattern of parameter variation drove a change from low speed short runs to high speed long runs, resembling the canonical descriptions of roaming and dwelling in

C. elegans [27].

Roaming and dwelling are thought to represent fundamental foraging strategies reflecting the trade-off between global exploration and local exploitation of environmental resources [52]. Recent work has suggested that such archetypal strategies can be recovered by quantitatively analyzing the geometry of phenotypic distributions in parameter space [26, 29]. The motility phenotypes we found in the present study were biased along one principal dimension, with the extremes corresponding to roaming and dwelling behaviors. This observation compels us to suggest that an exploration-exploitation trade-off is the primary driver of phenotypic diversification in the motility of chromadorean nematodes in the absence of stimuli. Interestingly, a recent study on the motility of a very different class of organisms (ciliates) yielded a similar conclusion[46]: across two species and different environments, the diversity of motility phenotypes was found to be distributed principally along an axis corresponding to roaming and dwelling phenotypes. The emergence of roaming/dwelling as the principal mode of variation in such disparate species underscores the idea that the exploration-exploitation trade-off is a fundamental constraint on biological motility strategies.

A surprising finding in our study was that, for a majority of strains, the extent of behavioral variability across individuals within a strain was comparable to that for variation of phenotypes across species (Figure 2.6). In slowly changing environments, the most evolutionarily successful species are those that consistently perform well in that environment. This can be achieved by evolving a specialized, high fitness phenotype that varies little among individuals (such as with PS312 and sjh2). However, increased phenotypic variability among individuals can improve fitness in more variable environments if some individuals perform much better in each condition: a so-called "bet-hedging" strategy [47, 48]. The large variability we observed among individual phenotypes within each strain might reflect such a bet-hedging strategy in nematode exploratory behavior.

The observation that the variation among genetically identical individuals can be comparable to that between disparate species raises the intriguing possibility that there exist conserved molecular and/or physiological pathways driving diversification of spatial exploration strategies. Analogous variation in exploratory behavior was also detected in an analysis of nonstationarity in the behavior of wild-type and mutant *C. elegans*

under various nutritional conditions [26]. Physiologically, protein kinase G (PKG) signaling and DAF-7 (TGF-β) signaling from the ASI neuron are thought to be major mechanisms controlling roaming and dwelling in *C. elegans* [25, 26]. PKG signaling is also involved in controlling foraging in *Drosophila* and other insects as well as many aspects of mammalian behavior [53, 54]. Flavell et al. also elucidated a neuromodulatory pathway involving serotonin and the neuropeptide pigment dispersing factor (PDF) controlling the initiation and duration of roaming and dwelling states [27].

Perturbations to the molecular parameters of such pathways underlying global behavioral changes might provide a mechanism for the observed correlated variations at the individual, intra-, and inter-species levels. The identification of such conserved pathways affecting many phenotypic parameters is of fundamental interest also from an evolutionary perspective, as they have been proposed to bias the outcome of random mutations towards favorable evolutionary outcomes [55, 56]. Our simple model provides a basis for future investigations to uncover conserved mechanisms that generate behavioral variability, by defining a succinct parameterization of behavior that can be combined with genetic and physiological methods.

2.4. METHODS

CULTIVATION OF WORMS

Worms were grown on NGM-SR plates seeded with *E. coli* HB101, as previously described [57]. *E. coli* HB101 was first cultured in M9 minimal media supplemented with 10% Luria broth and 10 mg mL^{-1} streptomycin [S8] [58]. Plates were incubated with a light circle of HB101 culture for a day at 37 °C and then stored at 4 °C. For *Plectus sp.* sjh2, low salt plates were used as previously described [59]. On NGM-SR plates, these worms became shriveled and died. As the plates did not have nutrients for the bacteria to grow, HB101 was grown to high density in Luria broth overnight at 37 °C, washed 3X in water, resuspended at 10X concentration, and applied to the plates. Nematodes were cultured by either transferring a few worms by worm pick or a chunk of agar to a new plate after the worms reached adulthood. The plates were then incubated at 20 °C. The growth rate varied considerably among strains, with *Plectus sp.* sjh2 taking nearly

two weeks to reach adulthood. We avoided starving the worms at any point during their cultivation, especially in the period before behavioral experiments were performed, as this can induce transgenerational phenotypic changes [60, 61] and we have observed transient effects on motility lasting at least a couple of generations (data not shown).

IMAGING

The imaging experiments were done on 3.5 cm plates containing the same media used for cultivation. A 2×2 10 mm repellant grid was made by etching the plate with a tool dipped in 1% sodium dodecyl sufate, a detergent that *C. elegans* and most other nematodes avoided. (Whereas many *C. elegans* studies have used copper rings as a repellant boundary [62], we found that it did not sufficiently repel other nematodes; data not shown). Four young adult, well-fed nematodes were transferred individually by worm pick to a 10 µL drop of M9 (water for *Plectus sp.* sjh2) to remove bacteria stuck to the worms. The worms were then transferred by pipette in a minimal amount of buffer to the imaging plate, and excess buffer was removed as much as possible. The plate was imaged 10-20 minutes after picking the worms, minimizing most transient behaviors. The plate was placed on a custom imaging rig in an inverted, uncovered configuration with illumination by a Schott MEBL-CR50 red LED plate. The behavior was recorded for 30 minutes using a Point Grey Grasshopper Express GX-FW-60S6M-C camera equipped with an Edmund Optics NT54-691 lens (set to a magnification of 0.5X) at a resolution of 2736x2192 (12.5 µm/px) at 11.5 frames/s using a custom National Instruments LabView acquisition program. The video was subsequently compressed using the open-source XVid MPEG-4 compression algorithm using maximal quality settings.

TRACKING AND IMAGE ANALYSIS

The behavioral videos were analyzed using a custom automated analysis program in MathWorks Matlab. The average background was calculated from 50 frames evenly sampled across the entire video. The background was then subtracted from each frame and a global threshold was applied. The thresholded image was cleaned by applying a series of morphological operations: Incomplete thresholding of the worm was smoothed by applying morphological closing with a disk with a similar radius as the

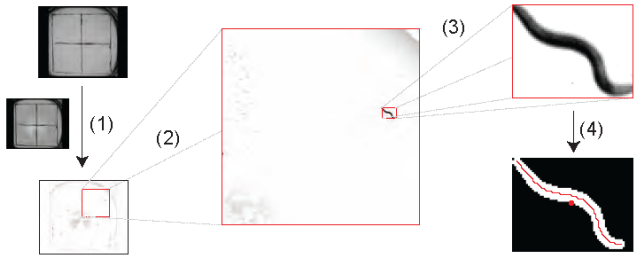

Figure 2.7: An Overview of the image processing steps. The video frames were processed by (1) subtracting the average of 50 frames evenly sampled from the entire movie and (2) cropping to each of the SDS-enclosed regions. (3) The largest worm-sized object was identified following several image morphology operations, and (4) the centroid and image skeleton were measured.

worm. Any remaining holes were filled in using a hole-filling algorithm. Small holes or ones with a low perimeter to area ratio were excluded as they sometimes fill in worms undergoing an omega turn, as described in [63]. Finally, regions in which the worm was just barely touching itself were split by sequentially applying open, diagonal fill, and majority morphological operations. The worm was then identified as the largest connected component with an area within 2-fold of the expected value. The centroid was tracked across frames to obtain $\vec{x}(t)$. In addition, the image skeleton was calculated. Sample images from each of the processing steps are shown in Figure 2.7.

The head of the worm was automatically identified using two statistical properties of the worm's behavior, namely (i) on average, the head of the worm moves more than the tail, and (ii) on average, worms spend more time moving forward (in the direction of their head) than they do moving in reverse. The procedure is based on skeletonization and centroid detection of the worm image, which can fail in situations where image contrast is low (e.g. due to non-uniform background), so trajectories were first divided into segments that contain no more than 3 frames missing the skeleton and centroid information, and the head orientation was assigned within each segment based on local behavioral statistics. Finding statistical criteria that allow unambiguous assignment of head orientation across all strains studied here was challenging because of the diversity in their behavior, but the following procedure was found to work

well empirically. The identity of the two ends of the skeleton across image frames were accounted for by a simple tracking algorithm based on minimizing the total distance between skeleton points. For segments longer than 150 frames (with no more than ten consecutive missing skeletons), we found that we could apply property (i) by computing the variance in body angles within 10% of the body length from the ends, and assigning the head to the end with the greater summed variance. However, manual inspection revealed that this sporadically resulted in misassignment of the head, identifiable as long reversals interrupted by short forward runs. Therefore, in addition, for segments longer than 200 frames (with no more than five consecutive missing centroids), we used property (ii), defining the head as the end of the skeleton that spent the majority of the trajectory at the leading edge of movement. Segments shorter than 150 frames were discarded from further analysis.

When the worm's speed $s(t) = |\vec{v}(t)|$ is very low, its projections on the lab-frame x- and y-axes $v_x = \vec{v}(t) \cdot \hat{x}$ and $v_y = \vec{v}(t) \cdot \hat{y}$ become dominated by discretization (pixelation) noise, and the bearing $\phi(t) = \tan^{-1}(v_y/v_x)$ is poorly defined. This in turn leads to large fluctuations in $\Delta\psi(t) = \phi(t) - \psi(t)$, which can introduce a large number of false reversal events, noticeable as a steep decrease in the autocorrelation $C_{\Delta\psi}(\tau) = \langle \cos\big(\Delta\psi(t+\tau) - \Delta\psi(t)\big)\rangle$ at small values of the delay τ. We therefore exclude segments of the trajectories corresponding to run intervals shorter than six frames (less than half a second). When these artifacts are filtered out in this manner, the $\Delta\psi$ autocorrelation functions were well described by single exponentials (see Fig. S7 of [1]). We note that the exclusion of short runs effectively excludes segments of data in which the worm remains stopped (or at a very low speed) — a feature that is more pronounced in some strains than others — and this leads to a systematic bias for simulated model trajectories to have a higher effective diffusivity D_{eff} than the data for the corresponding strain (as can be seen in Figure 2.5C).

CALCULATION OF BEHAVIORAL STATISTICS

The worm's behavior fluctuated or sometimes drifted over long times (see Fig. (S4) in [1]), but the average statistics over 100 s windows were approximately stationary. In order to focus on dynamics within the 100 s timescale, the mean-squared displacement and all auto- and cross-correlation functions were calculated for 100 s windows and then averaged. This re-

duced the influence of longer timescale fluctuations in the speed and reversal rate. For all calculations, observations near the boundaries and pairs of points between which the worm approached the boundary were excluded. The uncertainty of each individual's phenotype projection on the principal behavioral mode was computed by projecting the motility parameters after bootstrapping over the 100s windows of each individual's trajectory. The standard deviation of the bootstrapped projections is used as uncertainty.

CALCULATION OF EFFECTIVE DIFFUSIVITY, D_{EFF}

To estimate the effective diffusivity D_{eff}, we fit the mean-squared displacement $\langle[\Delta x(\tau)]^2\rangle$ over the diffusive regime. For this purpose, we defined the diffusive regime as the time-lag interval after which the normalized velocity autocorrelation $C_{\vec{v}}(\tau)/C_{\vec{v}}(0)$ decayed to below 0.1. We note that in some cases (especially for fast-moving strains such as CB4856, JU775 and sjh2) the fit to $\langle[\Delta x(\tau)]^2\rangle = 4D_{\text{eff}}\tau$ in this regime was poor due to boundary effects arising from the finite size of the behavioral arena. For these strains, D_{eff} should be regarded as a lower bound for the true diffusivity.

REVERSAL ANALYSIS

The reversal state was assigned as described in the main text by analysis of $\Delta\psi(t)$. Assuming a random telegraph process that generates states $\Delta\psi = 0$ (forward) and $\Delta\psi = \pi$ (reverse) with probabilities $1 - f_{rev}$ and f_{rev}, respectively, the autocorrelation at long time lags is $C_{\Delta\psi}(\tau \to \infty) = (1 - 2f_{rev})^2$. For the proposed telegraph process, each state has an exponentially distributed lifetime $(\tau_{\text{fwd}}, \tau_{\text{rev}})$ and therefore $f_{rev} = \dfrac{\tau_{\text{rev}}}{\tau_{\text{rev}} + \tau_{\text{fwd}}}$. The expected correlation timescale for the mixture of the two states is $\tau_{RT}(\tau_{\text{rev}}, \tau_{\text{fwd}}) = \left(\tau_{\text{fwd}}^{-1} + \tau_{\text{rev}}^{-1}\right)^{-1}$. The $\Delta\psi$ autocorrelation function was therefore fit to

$$C_{\Delta\psi}(\tau) = [1 - C_{\Delta\Psi\infty}(\tau_{\text{rev}}, \tau_{\text{fwd}})] \exp\left[-\frac{\tau}{\tau_{RT}(\tau_{\text{rev}}, \tau_{\text{fwd}})}\right] + C_{\Delta\Psi\infty}(\tau_{\text{rev}}, \tau_{\text{fwd}}) \tag{2.8}$$

where $C_{\Delta\Psi\infty}(\tau_{\text{rev}}, \tau_{\text{fwd}}) = (\dfrac{\tau_{\text{fwd}} - \tau_{\text{rev}}}{\tau_{\text{fwd}} + \tau_{\text{rev}}})^2$. The fraction of time spent reversing is: $f_{\text{rev}} = 0.5 - \sqrt{C_{\Delta\Psi\infty}(\tau_{\text{rev}}, \tau_{\text{fwd}})/4}$, where $f_{\text{rev}} \in [0, 0.5]$. The transition time constants are then $\tau_{\text{rev}} = \dfrac{\tau_{RT}(\tau_{\text{rev}}, \tau_{\text{fwd}})}{1 - f_{\text{rev}}}$ and $\tau_{\text{fwd}} = \dfrac{\tau_{RT}(\tau_{\text{rev}}, \tau_{\text{fwd}})}{f_{\text{rev}}}$.

The parameters obtained with our fitting procedure are in agreement

with those obtained from the distribution of time intervals between detected switching events (see Fig. S7 in [1]).

SPEED ANALYSIS

Transitions between forward and reverse runs tended to be excluded from the analysis because the speed crosses zero, rendering ϕ a noisy variable generating many short runs below our exclusion threshold of 6 frames (see above). The speed set point μ_s was fit by taking the mean. The remaining parameters of the speed dynamics (3) were fit by its analytical autocovariance function: $C_s(\tau) = D_s\tau_s \exp(-\tau/\tau_s)$.

ORIENTATION ANALYSIS

Changes in orientation during runs (*i.e.* intervals between reversal events) were analyzed with respect to their mean-squared angular displacements (MSAD) over time, corresponding to a model for angular diffusion with drift.

For an object lying on a two-dimensional plane, rotational diffusion about an axis normal to the plane leads to fluctuations in the orientation (an angle measured in the lab frame) $\psi(t)$ over time according to:

$$d\psi(t) = \sqrt{2D_\psi}\,dW_t, \tag{2.9}$$

where D_ψ is the rotational diffusion coefficient, and dW_t represents increments of a Wiener process. Bias in these fluctuations over time can be captured, to first order, by adding a linear drift term so that

$$d\psi(t) = k_\psi\,dt + \sqrt{2D_\psi}\,dW_t, \tag{2.10}$$

with k_ψ the drift coefficient.

If k_ψ and D_ψ are constant in time, the mean-squared angular displacement $\mathrm{MSAD}(\tau) = \langle[\psi(t+\tau) - \psi(t)]^2\rangle$, is a quadratic function of the time delay τ:

$$\langle[\psi(t+\tau) - \psi(t)]^2\rangle = \langle[k_\psi\tau + \sqrt{2D_\psi}(W_{t+\tau} - W_t)]^2\rangle = k_\psi^2\tau^2 + 2D_\psi\tau, \tag{2.11}$$

where $\langle\cdot\rangle$ denotes averaging over all time pairs separated by τ and the last equality follows from the Wiener process properties $\langle W_{t+\tau} - W_t\rangle = 0$ and $\langle[W_{t+\tau} - W_t]^2\rangle = \tau$.

More generally, if $k_\psi(t)$ and $D_\psi(t)$ are time-varying quantities, we can still approximate within a finite time window (centered about time t_w) the "local" values $k_{\psi,w} \approx k_\psi(t_w)$ and $D_{\psi,w} \approx D_\psi(t_w)$. In this study, we extract estimates of these (possibly time varying) parameters from fits to the averaged MSAD computed over time windows:

$$W^{-1} \sum_{w=1}^{w=W} \langle [\psi(t+\tau) - \psi(t)]^2 \rangle = \langle k_\psi^2 \rangle_w \tau^2 + 2 \langle D_\psi \rangle_w \tau, \tag{2.12}$$

where W is the number of windows and $\langle x \rangle_w = W^{-1} \sum_{w=1}^{w=W} x_w$ represents averages over windows. By fitting this averaged MSAD by a quadratic function $a\tau + b\tau^2$, we thus obtain the estimates $a/2 = \langle D_\psi \rangle_w$ and $\sqrt{b} = \langle k_\psi^2 \rangle_w^{1/2}$. Note that $a/2$ obtained by this procedure yields an estimate of the mean value for D_ψ, but $\sqrt{b}$ corresponds to an estimate not of the mean value, but the root-mean-square (rms) value for k_ψ. Throughout the text, we therefore explicitly refer to the latter estimate as $k_{\psi\mathrm{rms}}$ (and refer to the former simply as D_ψ).

SIMULATIONS

Reversals, orientation, and speed dynamics were all simulated independently using the model described. Forward and reverse run durations were chosen according to eq. (2.6) and eq. (2.7) by drawing exponential random numbers with mean value τ_{fwd} or τ_{rev}. During reverse runs, $\Delta\psi$ was set to π. The orientation, eq. (2.5), and speed, eq. (2.4), dynamics were simulated using the Euler-Maruyama method [64] with a time step that matched the frame rate. To prevent negative speeds, a reflective boundary condition was imposed by taking the absolute value of the speed at each simulation step. The velocity was then calculated from the decomposition in eq. (2.2) and trapezoidally integrated to give the centroid position $\vec{x}(t)$.

BEHAVIORAL MODE ANALYSIS

The model parameters were fit to each trajectory to give a phenotypic matrix $\mathbf{T}$. The phenotypic matrix was centered by subtracting the mean phenotype, $\hat{\mathbf{T}} = \mathbf{T} - \langle \mathbf{T} \rangle_{\mathrm{indiv.}}$. The correlation matrix was then calculated, $\mathbf{C_T} = \mathrm{corr}\hat{\mathbf{T}}$, and decomposed into eigenvalues λ and eigenvectors (behavioral modes) $\mathbf{b}$, $\mathbf{C_T b} = \lambda \mathbf{b}$. To reduce any bias coming from a single

trajectory, this calculation was bootstrapped 1000 times. The significance of the k-th top mode is assessed by a comparison with the expected variance explained of the k-th top mode of randomly chosen directions in the behavioral space. We use the explained variance of the k-th mode of a newly created set of modes where the first $k-1$ modes are equal to the top behavioral modes and the remaining modes are pointing in randomly chosen orthogonal directions. This process is repeated 1000 times. The projections of each trajectory on these behavioral modes were calculated by $\mathbf{P} = \hat{\mathbf{T}}\mathbf{b}$. The uncertainty in the locus of each individual phenotype along the behavioral mode was computed by projecting the motility parameters after bootstrapping over the 100 second windows and taking the standard deviation.

STATISTICS

Unless otherwise indicated, errorbars and confidence intervals represent the 2.5% and 97.5% percentiles (spanning the 95% confidence interval) estimated from 1000 bootstrap samples. All probability distributions were empirically estimated using kernel density methods in Python's Seaborn package with a bandwidth automatically selected using Scott's rule of thumb [65]. Tabulated mean values of the effective diffusivity model and the motility model (Table S1-S4 in [1]) represent geometric rather than arithmetic means was used as the parameters varied log-normally.

DERIVATION OF THE VELOCITY AUTOCORRELATION FUNCTION UNDER THE ASSUMPTION OF INDEPENDENCE

The velocity autocorrelation function can be written in terms of the motility components,

$$\begin{aligned} C_{\vec{v}}(\tau) &= \langle \vec{v}(0) \cdot \vec{v}(\tau) \rangle \\ &= \langle s(0) \left[\cos\left[\psi(0) + \Delta\psi(0)\right], \sin\left[\psi(0) + \Delta\psi(0)\right] \right] \times \\ &\times s(\tau) \left[\cos\left[\psi(\tau) + \Delta\psi(\tau)\right], \sin\left[\psi(\tau) + \Delta\psi(\tau)\right] \right] \rangle \end{aligned} \tag{2.13}$$

The expected value of the product of independent random variables is the product of the expected value of each variable, i.e. $\langle xy \rangle = \langle x \rangle \langle y \rangle$. Therefore we can factor out $C_s = \langle s(0)s(\tau) \rangle$, leaving the vector product

with ψ and $\Delta\psi$. The expanded vector product is:

$$C_{\vec{v}}(\tau) = C_s(\tau) \times \langle \cos\left[\psi(0) + \Delta\psi(0)\right] \cos\left[\psi(\tau) + \Delta\psi(\tau)\right] + \sin\left[\psi(0) + \Delta\psi(0)\right] \sin\left[\psi(\tau) + \Delta\psi(\tau)\right] \rangle \tag{2.14}$$

The trigonometric functions on $\psi(t) + \Delta\psi(t)$ can be rewritten as products of trigonometric functions of the terms:

$$\begin{aligned} \cos\left[\psi(t) + \Delta\psi(t)\right] &= \cos\psi(t)\cos\Delta\psi(t) - \sin\psi(t)\sin\Delta\psi(t) \\ \sin\left[\psi(t) + \Delta\psi(t)\right] &= \sin\psi(t)\cos\Delta\psi(t) + \cos\psi(t)\sin\Delta\psi(t) \end{aligned}$$

However, since $\Delta\psi(t) = \{0, \pi\}$, $\sin\Delta\psi(t) = 0$:

$$\begin{aligned} \cos\left[\psi(t) + \Delta\psi(t)\right] &= \cos\psi(t)\cos\Delta\psi(t) \\ \sin\left[\psi(t) + \Delta\psi(t)\right] &= \sin\psi(t)\cos\Delta\psi(t) \end{aligned}$$

Substituting into (2.14),

$$C_{\vec{v}}(\tau) = C_s(\tau) \times \langle \cos\psi(0)\cos\psi(\tau)\cos\Delta\psi(0)\cos\Delta\psi(\tau) + \sin\psi(0)\sin\psi(\tau)\cos\Delta\psi(0)\cos\Delta\psi(\tau) \rangle \tag{2.15}$$

We can now factor out $C_\psi(\tau) = \langle \cos\left[\psi(\tau) - \psi(0)\right] \rangle = \langle \cos\psi(0)\cos\psi(\tau) + \sin\psi(0)\sin\psi(\tau) \rangle$ to get:

$$C_{\vec{v}}(\tau) = C_s(\tau) C_\psi(\tau) \langle \cos\Delta\psi(0)\cos\Delta\psi(\tau) \rangle$$

Finally, we substitute (again dropping $\sin\Delta\psi(t)$ terms):

$$C_{\Delta\psi}(\tau) = \langle \cos\left[\Delta\psi(0) - \Delta\psi(\tau)\right] \rangle = \langle \cos\Delta\psi(0)\cos\Delta\psi(\tau) \rangle$$

to get:

$$C_{\vec{v},\mathrm{indep}}(\tau) = C_s(\tau) C_\psi(\tau) C_{\Delta\psi}(\tau)$$

ACKNOWLEDGMENTS

We thank Massimo Vergassola, Vasily Zaburdaev, Alon Zaslaver, and Jeroen van Zon for helpful suggestions and critical reading of the manuscript, Will Ryu, Aravi Samuel and Andre Brown for inspiration and encouragement, and members of the Shimizu lab for discussions. Casper Quist and Hans Helder of Wageningen University provided wild nematodes isolated from soil and useful information regarding the ecology of nematodes. This work was supported by the research program of the Foundation for Fundamental Research on Matter (FOM), which is part of the Netherlands Organization for Scientific Research (NWO).

REFERENCES

[1] S. J. Helms, W. M. Rozemuller, A. C. Costa, L. Avery, G. J. Stephens, and T. S. Shimizu, *Modelling the ballistic-to-diffusive transition in nematode motility reveals variation in exploratory behaviour across species,* Journal of The Royal Society Interface **16**, 20190174 (2019).

[2] H. C. Berg and D. A. Brown, *Chemotaxis in Escherichia coli analysed by Three-dimensional Tracking,* Nature **239**, 500 (1972).

[3] P. S. Lovely and F. W. Dahlquist, *Statistical measures of bacterial motility and chemotaxis.* J. Theor. Biol. **50**, 477 (1975).

[4] M. Schnitzer, S. Block, H. Berg, and E. Purcell, *Strategies for chemotaxis.* Symp. Soc. Gen. Microbio. **46**, 15 (1990).

[5] P. G. De Gennes, *Chemotaxis: The role of internal delays,* Eur. Biophys. J. **33**, 691 (2004).

[6] A. Celani, T. S. Shimizu, and M. Vergassola, *Molecular and Functional Aspects of Bacterial Chemotaxis,* J. Stat. Phys. **144**, 219 (2011).

[7] M. H. Gail and C. W. Boone, *The locomotion of mouse fibroblasts in tissue culture,* Biophys. J. **10**, 980 (1970).

[8] R. T. Tranquillo, D. A. Lauffenburger, and S. H. Zigmond, *A stochastic model for leukocyte random motility and chemotaxis based on receptor binding fluctuations,* J. Cell Biol. **106**, 303 (1988).

[9] D. Selmeczi, S. Mosler, P. H. Hagedorn, N. B. Larsen, and H. Flyvbjerg, *Cell motility as persistent random motion: theories from experiments,* Biophys. J. **89**, 912 (2005).

[10] P. H. Wu, A. Giri, S. X. Sun, and D. Wirtz, *Three-dimensional cell migration does not follow a random walk,* Proceedings of the National Academy of Sciences of the United States of America **111**, 3949 (2014).

[11] A. E. Brown and B. De Bivort, *Ethology as a physical science,* Nature Physics , 1 (2018).

[12] J. Gjorgjieva, D. Biron, and G. Haspel, *Neurobiology of caenorhabditis elegans locomotion: Where do we stand?* BioScience **64**, 476 (2014).

[13] N. Cohen and T. Sanders, *Nematode locomotion: dissecting the neuronal–environmental loop,* Curr. Opin. Neurobiol. **25**, 99 (2014).

[14] N. A. Croll, *Behavioural analysis of nematode movement,* Adv. Parasitol. **13**, 71 (1975).

[15] N. A. Croll, *Behavioural analysis of nematode movement.* Adv. Parasitol. **13**, 71 (1975).

[16] W. M. Roberts, S. B. Augustine, K. J. Lawton, T. H. Lindsay, T. R. Thiele, E. J. Izquierdo, S. Faumont, R. A. Lindsay, M. C. Britton, N. Pokala, *et al.*, *A stochastic neuronal model predicts random search behaviors at multiple spatial scales in C. elegans,* Elife **5**, e12572 (2016).

[17] J. Gray and H. W. Lissmann, *The locomotion of nematodes,* J. Exp. Biol. **41**, 135 (1964).

[18] O. D. Broekmans, J. B. Rodgers, W. S. Ryu, and G. J. Stephens, *Resolving coiled shapes reveals new reorientation behaviors in c. elegans,* eLife **5(e17227)** (2016), 10.7554/eLife.17227.

[19] Y. Iino and K. Yoshida, *Parallel use of two behavioral mechanisms for chemotaxis in Caenorhabditis elegans.* J. Neurosci. **29**, 5370 (2009).

[20] M. Peliti, J. S. Chuang, and S. Shaham, *Directional locomotion of C. elegans in the absence of external stimuli,* PLoS ONE **8** (2013), 10.1371/journal.pone.0078535.

[21] J. T. Pierce-Shimomura, T. M. Morse, and S. R. Lockery, *The fundamental role of pirouettes in Caenorhabditis elegans chemotaxis.* J. Neurosci. **19**, 9557 (1999).

[22] S. Faumont, T. Lindsay, and S. Lockery, *Neuronal microcircuits for decision making in C. elegans.* Curr. Opin. Neurobiol. **22**, 580 (2012).

[23] W. S. Ryu and A. D. T. Samuel, *Thermotaxis in Caenorhabditis elegans analyzed by measuring responses to defined thermal stimuli.* J. Neurosci. **22**, 5727 (2002).

[24] A. J. Calhoun, S. H. Chalasani, and T. O. Sharpee, *Maximally informative foraging by Caenorhabditis elegans.* Elife **3** (2014), 10.7554/eLife.04220.

[25] M. Fujiwara, P. Sengupta, and S. L. McIntire, *Regulation of body size and behavioral state of C. elegans by sensory perception and the EGL-4 cGMP-dependent protein kinase.* Neuron **36**, 1091 (2002).

[26] T. Gallagher, T. Bjorness, R. Greene, Y. J. You, and L. Avery, *The Geometry of Locomotive Behavioral States in C. elegans,* PLoS ONE **8** (2013), 10.1371/journal.pone.0059865.

[27] S. W. Flavell, N. Pokala, E. Z. Macosko, D. R. Albrecht, J. Larsch, and C. I. Bargmann, *Serotonin and the neuropeptide PDF initiate and extend opposing behavioral states in C. elegans,* Cell **154**, 1023 (2013).

[28] L. C. M. Salvador, F. Bartumeus, S. A. Levin, and W. S. Ryu, *Mechanistic analysis of the search behaviour of Caenorhabditis elegans,* J. R. Soc. Interface **11**, 20131092 (2014).

[29] O. Shoval, H. Sheftel, G. Shinar, Y. Hart, O. Ramote, A. Mayo, E. Dekel, K. Kavanagh, and U. Alon, *Evolutionary trade-offs, Pareto optimality, and the geometry of phenotype space.* Science **336**, 1157 (2012).

[30] P. De Ley, *A quick tour of nematode diversity and the backbone of nematode phylogeny.* WormBook (2006), 10.1895/wormbook.1.41.1.

[31] A. K. Corsi, B. Wightman, and M. Chalfie, *A Transparent Window into Biology: A Primer on Caenorhabditis elegans,* Genetics **200**, 387 (2015).

[32] I. Rabinowitch and W. Schafer, *Neuronal remodeling on the evolutionary timescale.* J. Biol. **7**, 37 (2008).

[33] G. J. Stephens, B. Johnson-Kerner, W. Bialek, and W. S. Ryu, *From modes to movement in the behavior of Caenorhabditis elegans.* PLoS One **5**, e13914 (2010).

[34] M. Vahabi, J. H. Schulz, B. Shokri, and R. Metzler, *Area coverage of radial Lévy flights with periodic boundary conditions,* Physical Review E - Statistical, Nonlinear, and Soft Matter Physics **87**, 1 (2013).

[35] V. Artale, G. Boffetta, A. Celani, M. Cencini, and A. Vulpiani, *Dispersion of passive tracers in closed basins: Beyond the diffusion coefficient,* Physics of Fluids **9**, 3162 (1997).

[36] N. V. Kampen, *North-holl. Pers. Libr.* (North Holland, 2007).

[37] J. M. Gray, J. J. Hill, and C. I. Bargmann, *A circuit for navigation in Caenorhabditis elegans.* Proceedings of the National Academy of Sciences of the United States of America **102**, 3184 (2005).

[38] A. Papoulis, *Probability, Random Variables, and Stochastic Processes*, 2nd ed. (McGraw-Hill, New York, 1984) pp. 392–393.

[39] M. Chalfie, J. Sulston, J. White, E. Southgate, J. Thomson, and S. Brenner, *The neural circuit for touch sensitivity in Caenorhabditis elegans,* J. Neurosci. **5**, 956 (1985).

[40] B. J. Piggott, J. Liu, Z. Feng, S. A. Wescott, and X. S. Xu, *The neural circuits and synaptic mechanisms underlying motor initiation in C. elegans,* Cell **147**, 922 (2011).

[41] J. G. Culotti and R. L. Russell, *Osmotic avoidance defective mutants of the nematode Caenorhabditis elegans.* Genetics **90**, 243 (1978).

[42] M. S. Green, *Markoff Random Processes and the Statistical Mechanics of Time-Dependent Phenomena. II. Irreversible Processes in Fluids,* J. Chem. Phys. **22**, 398 (1954).

[43] R. Kubo, *Statistical-Mechanical Theory of Irreversible Processes. I. General Theory and Simple Applications to Magnetic and Conduction Problems,* J. Phys. Soc. Japan **12**, 570 (1957).

[44] K. P. Murphy, *Mach. Learn. A Probabilistic Perspect.* (The MIT Press, Cambridge, MA, 2012).

[45] K. a. Osborne, A. Robichon, E. Burgess, S. Butland, R. A. Shaw, A. Coulthard, H. S. Pereira, R. J. Greenspan, and M. B. Sokolowski, *Natural behavior polymorphism due to a cGMP-dependent protein kinase of Drosophila.* Science **277**, 834 (1997).

[46] D. Jordan, S. Kuehn, E. Katifori, and S. Leibler, *Behavioral diversity in microbes and low-dimensional phenotypic spaces.* Proceedings of the National Academy of Sciences of the United States of America **110**, 14018 (2013).

[47] M. Slatkin, *Hedging one's evolutionary bets,* Nature **250**, 704 (1974).

[48] T. Philippi and J. Seger, *Hedging one's evolutionary bets, revisited.* Trends Ecol. Evol. **4**, 41 (1989).

[49] K. Kiontke and D. H. Fitch, *Nematodes,* Curr. Biol. **23**, R862 (2013).

[50] G. J. Stephens, B. Johnson-Kerner, W. Bialek, and W. S. Ryu, *Dimensionality and dynamics in the behavior of C. elegans.* PLoS Comput. Biol. **4**, e1000028 (2008).

[51] A. E. X. Brown, E. I. Yemini, L. J. Grundy, T. Jucikas, and W. R. Schafer, *A dictionary of behavioral motifs reveals clusters of genes affecting Caenorhabditis elegans locomotion,* Proceedings of the National Academy of Sciences of the United States of America **110**, 791 (2013).

[52] N. B. Davies, J. R. Krebs, and S. A. West, *An Introduction to Behavioural Ecology*, 4th ed. (Wiley-Blackwell, 2012).

[53] C. J. Reaume and M. B. Sokolowski, *cGMP-dependent protein kinase as a modifier of behaviour.* Handb. Exp. Pharmacol. **191**, 423 (2009).

[54] K. R. Kaun and M. B. Sokolowski, *cGMP-dependent protein kinase: linking foraging to energy homeostasis.* Genome **52**, 1 (2009).

[55] M. Kirschner and J. Gerhart, *Evolvability,* Proc. Natl. Acad. Sci. U.S.A. **95**, 8420 (1998).

[56] J. Gerhart and M. Kirschner, *The theory of facilitated variation.* Proc. Natl. Acad. Sci. U. S. A. , 8582 (2007).

[57] M. W. Davis, D. Somerville, R. Y. Lee, S. Lockery, L. Avery, and D. M. Fambrough, *Mutations in the Caenorhabditis elegans Na,K-ATPase alpha-subunit gene, eat-6, disrupt excitable cell function.* J. Neurosci. **15**, 8408 (1995).

[58] T. Stiernagle, *Maintenance of C. elegans,* WormBook (2006), doi/10.1895/wormbook.1.101.1.

[59] V. Lahl, C. Halama, and E. Schierenberg, *Comparative and experimental embryogenesis of Plectidae (Nematoda).* Dev. Genes Evol. **213**, 18 (2003).

[60] S. E. Hall, M. Beverly, C. Russ, C. Nusbaum, and P. Sengupta, *A cellular memory of developmental history generates phenotypic diversity in C. elegans.* Curr. Biol. **20**, 149 (2010).

[61] O. Rechavi, L. Houri-Ze'evi, S. Anava, W. S. S. Goh, S. Y. Kerk, G. J. Hannon, and O. Hobert, *Starvation-Induced Transgenerational Inheritance of Small RNAs in C. elegans,* Cell **158**, 277 (2014).

[62] A. Hart, *Behavior,* WormBook (2006), 10.1895/wormbook.1.87.1.

[63] K.-M. Huang, P. Cosman, and W. R. Schafer, *Machine vision based detection of omega bends and reversals in C. elegans.* J. Neurosci. Methods **158**, 323 (2006).

[64] P. E. Kloeden and E. Platen, *Numerical Solution of Stochastic Differential Equations* (Springer Berlin Heidelberg, Berlin, Heidelberg, 1992).

[65] D. W. Scott, *Multivariate density estimation: theory, practice, and visualization* (John Wiley & Sons, 1992).

3

ADAPTIVE LOCALLY-LINEAR MODELS OF COMPLEX DYNAMICS

3.1. INTRODUCTION

In the previous chapter we have seen how a simple stochastic model of the position and orientation of *C. elegans* moving on a featureless environment captures coarse-grained features of the dynamics on ~ 100s time scales. This approach uncovered patterns of variation across distantly related nematodes, and a trade-off between exploration and exploitation. We will now take a finer scale look at *C. elegans* motility, by studying changes in its body posture. Posture takes us one step closer to the underlying neuromuscular mechanisms that control fine-scale movements, as well as the origins of its unpredictability. However, the high dimensional nature of a rich representation of posture presents novel challenges to quantitative understanding, and here we will describe a novel approach for the understanding of complex dynamical patterns, from data.

Complex dynamics are ubiquitous in nature; their diversity in systems ranging from fluids and turbulence [2, 3], to collective motion [4] and brain dynamics [5], is unified by common challenges of analysis which include high dimensionality, nonlinearity and nonstationarity. But how do we capture the quantitative details of the dynamics of complex systems with models simple enough to offer substantial intepretability?

Parts of this chapter have been published in the Proceedings of the National Academy of Sciences **116**(5), 1501-1510 (2019) [1]

Motivated by the remarkable increase in data quantity and quality as well as growing computational power, one approach is to fit a single global model to the dynamics with properties extracted from data. For example, deep neural networks and other machine learning techniques [6, 7] often produce high dimensional nonlinear models, which can precisely represent complex dynamics and yield accurate predictions. While powerful however, these methods can create representations of the dynamics that are too intricate for simple conceptual understanding. Another approach uses sparse regression to find a system of differential equations governing a nonlinear dynamical system [8]. Also, short time brain oscillations were studied using jPCA [9], a method that approximates the dynamics as a linear model with skew-symmetric couplings. Although promising, global methods are unable to handle non-stationarities, such as when a time series is composed of a set of distinct dynamics that change in time.

An alternative to global methods is to segment the dynamics into simpler components which change in time. For example, a low-dimensional representation of the spatiotemporal patterns found in the human brain was obtained through dynamic mode decomposition [10] in short temporal segments [11]. Studies on self-regulated dynamical criticality in the human brain used vector autoregressive models locally in time [12]. Behavioral motifs in *Drosophila melanogaster* were found using local-time wavelet analysis [13]. In these methods however, the local windows are defined phenomenologically, which may conflate distinct dynamical behaviors.

Principled approaches for the segmentation of time series include those of change-point detection [14–21], which aim to identify structural changes in the time series but often focus on the location of change-points or forecasting, instead of the underlying dynamics [16–21]. Other techniques such as hidden Markov models [22–24], assume that the global dynamics are composed of a set of underlying dynamical states which the system revisits, without providing a parameterization of the underlying dynamical patterns [24]. More recently, switching linear dynamical systems and autoregressive hidden Markov models [25–27] were developed with the aim of providing such a parameterization, but they do so either by setting the number of breaks from the onset [28, 29], or by assuming that there is a set of underlying dynamical regimes and that the system switches between them [22, 23, 25–27, 30].

Here, we combine the simplicity of linear dynamical systems with a likelihood-based algorithm for identifying dynamical breaks to construct interpretable, data-driven models of complex dynamics, with minimal *a priori* assumptions about the breakpoints or the number of states. We approximate the full dynamics with first-order linear dynamical systems in short windows and use a likelihood-ratio test to estimate to what extent newly added observations fit the same linear model, thus adaptively determining the size of the local windows. The global dynamics is therefore parameterized as a set of linear couplings within windows of various lengths. We analyze the resulting model space using hierarchical clustering with a new likelihood-based similarity measure and by examining the dynamical eigenvalue spectra in three illustrative systems: the Lorenz dynamical system and both posture and whole brain dynamics of the nematode *C. elegans*. In addition, we extend our analysis to higher-dimensional dynamics: electrocorticography (ECoG) recordings in non-human primates and a population of hundreds of neurons in mouse visual cortex.

3.2. LOCALLY-LINEAR, ADAPTIVE SEGMENTATION TECHNIQUE

An overview of the segmentation technique is given in Fig. (3.1) and a detailed description as well as links to publicly available code are in Methods. Briefly, we iterate over pairs of consecutive windows, Fig. (3.1A), and estimate whether the linear model fit in the larger window θ_{k+1} is significantly more likely to model the observations in the larger window when compared to the model found in the smaller window θ_k, Fig. (3.1B). We compare the two models by the log-likelihood ratio Λ_{data} and assess the significance of Λ_{data} by using Monte Carlo methods to construct a likelihood ratio distribution $P_{\text{null}}(\Lambda)$ under the null hypothesis of no model change. This null distribution is used to define Λ_{thresh} according to a threshold probability, or significance level $P_{\text{null}}(\Lambda_{\text{thresh}})$. We identify a dynamical break when $\Lambda_{\text{data}} > \Lambda_{\text{thresh}}$ in which case we save the model parameters and start a new modeling process from the break location. If $\Lambda_{\text{data}} \leq \Lambda_{\text{thresh}}$ then no break is identified and we move to the next window pair $\{\theta_{k+1}, \theta_{k+2}\}$. Over the entire time series, our procedure yields a set of N windows of varying sizes with their respective linear model parameters,

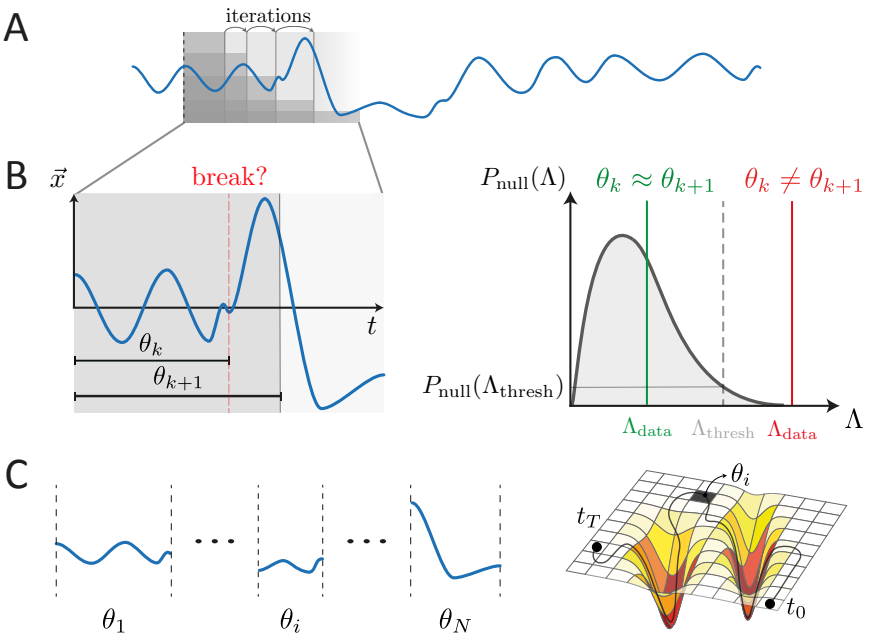

Figure 3.1: **Schematic of the adaptive, locally-linear segmentation algorithm.** (A) A d-dimensional time series is depicted as a blue line. We iterate over pairs of subsequent windows and use a likelihood-ratio test to assess whether there is a dynamical break between windows. (B) We compare linear models θ_k and θ_{k+1}, found in the windows X_k and X_{k+1}, by the log-likelihood ratio Λ_{data}, (3.3). To assess significance we compute the distribution of log-likelihood ratios under the null hypothesis of no model change $P_{\text{null}}(\Lambda)$ and identify a dynamical break when $\Lambda_{\text{data}} > \Lambda_{\text{thresh}}$ where $P_{\text{null}}(\Lambda_{\text{thresh}}) = 0.05$. If no break is identified, we continue with the windows $\{\theta_{k+1}, \theta_{k+2}\}$. (C) The result of the segmentation algorithm is a set of windows of varying lengths and model parameters $\{\theta_1, \ldots, \theta_N\}$. Our approach is similar to approximating a complex-shaped manifold by a set of locally flat patches, and encodes a nonlinear time series through a trajectory within the space of local linear models.

$\{\theta_1, \ldots, \theta_N\}$, Fig. (3.1C) and is analogous to tiling a complex shaped manifold into local flat regions. We thus trade the complexity of the nonlinear time series for a space of simpler local linear models that captures important properties of the full dynamics.

3.2.1. SURVEYING THE SPACE OF MODELS

The application of locally-linear, adaptive segmentation generally results in a large set of linear dynamical systems (LDS) and we explore this space both through the eigenvalues of the coupling matrices and by model clustering through a novel, likelihood-based measure of similarity. Despite a typically large number of models, the dynamical eigenvalues offer a direct measure of local oscillations and stability. Complex conjugate eigenvalues represent oscillations, with frequency $f = \mathrm{Im}(\lambda)/(2\pi)$. A negative real part implies stable damped dynamics along that mode, while a positive real part implies unstable exponentially growing trajectories. As the least stable eigenvalue approaches 0 the system becomes sensitive to external perturbations. At the bifurcation point, $\mathrm{Re}(\lambda) = 0$, the susceptibility diverges and we enter a critical dynamical state [31–33]. The full spectrum of eigenvalues across models thus provides not only information about oscillatory patterns but also stability and criticality.

To cluster the models, we note that simply using the Euclidean metric is inappropriate, since the space of linear models is invariant under the action of the GL(n) group[1]. Instead, we define dissimilarity as the loss in likelihood when two windows are modeled by a single linear model constructed fitting within the combination of windows. Given two windows, X_a and X_b, we define the dissimilarity as $d_{a,b} = \Lambda_{c,a} + \Lambda_{c,b}$, where Λ is the log-likelihood ratio and c is the union of the windows $X_c = X_a \cup X_b$. We note that this measure is symmetric $d_{a,b} = d_{b,a}$, positive semi-definite $d_{a,b} \geq 0$ and does not require the windows to be the same size. If the dynamics in both windows are similar, then the combined model will still accurately fit each window. If not, then it will be far less likely to model the windows, resulting in a higher disparity between models. Once the dis-

[1] The action of $P \in \mathrm{GL}(n)$ to the matrix of linear couplings A results in new coupling matrix PA that is very different according to the euclidean metric, while representing the same linear dynamics. Therefore, using the Euclidean distance is deeply misleading as two matrices that are distant in euclidean metric can represent the same linear dynamical system.

similarity is computed between all models we perform hierarchical clustering by combining models according to Ward's minimum variance criterion [34].

3.3. LORENZ SYSTEM

As a demonstration of the locally-linear approach, we analyze the time series generated from the Lorenz dynamical system [35]:

$$\begin{aligned}\dot{x} &= \sigma(y-x)\\ \dot{y} &= x(\rho-z)-y\\ \dot{z} &= xy-\beta z,\end{aligned}$$

with $\beta = 8/3$ and $\sigma = 10$. We explore two dynamical regimes: transient chaos with late-time, stable spiral dynamics at $\rho = 20$ and the standard chaotic attractor with $\rho = 28$. For spiral dynamics, we vary the initial conditions to sample the dynamics approaching the fixed point at the center of each lobe, Fig. (3.2A), which have the same period but vary in their phase space trajectories. We apply adaptive segmentation and show the result of model-space clustering in Fig. (3.2B). We find a single dominant split in the clustering dendrogram, which corresponds to approaching the two different fixed points. Inside each branch the different linear models are all quite similar. In the chaotic regime however, we find substantially more structure and large dissimilarities between models even at the lower branches of the tree. Notably, the first split occurs between the two lobes of the attractor and more generally, the linear model clustering provides a partition of the Lorenz phase space with different levels of description depending on the depth in the dendrogram.

Further insight into the dynamics is reflected in the distribution of the spectrum of eigenvalues across the local linear models, Fig. (3.2C). In the spiral dynamics, we find two peaks reflecting a dominant pair of complex conjugate eigenvalues and these correspond to a decaying oscillation ($\mathrm{Re}(\lambda) < 0$). We note that while the local coupling matrix is constructed from finite temporal windows and is not the instantaneous Jacobian, the dynamical eigenvalues are close to those derived from linear stability of the fixed points (Methods). In contrast, the spectrum in the chaotic regime reflects a complexity of behaviors, with many models

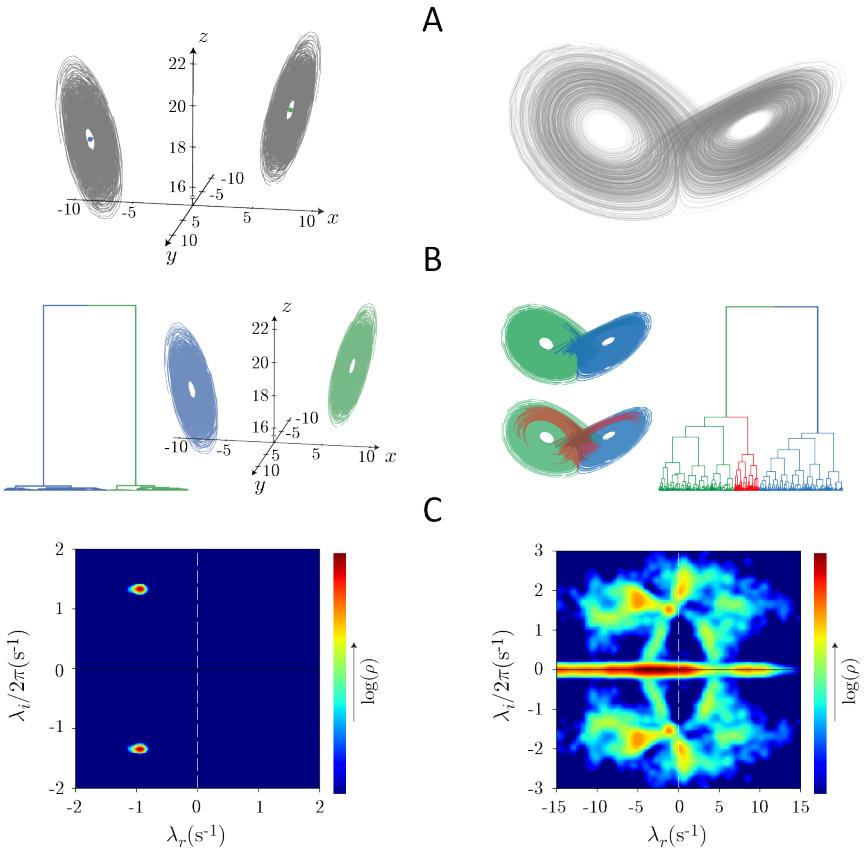

Figure 3.2: **Adaptive segmentation of the Lorenz dynamical system and likelihood-based clustering of the resulting model space.** (A) Simulated Lorenz system for stable spiral dynamics (left) $\{\rho = 20, \beta = 8/3, \sigma = 10\}$ and the standard chaotic regime (right) $\{\rho = 28, \beta = 8/3, \sigma = 10\}$. (B) Likelihood-based hierarchical model clustering. In the spiral dynamics there is a large separation between models from each lobe, while the dynamics within lobe are very similar. In the chaotic regime, the model-space clustering first divides the two lobes of the attractor and the full space is intricate and heterogeneous. (C) Dynamical eigenvalue spectrum for each regime, λ_r and λ_i respectively represent the real and imaginary eigenvalues. The spiral dynamics (left) exhibits a pair of stable, complex conjugate peaks while in the chaotic regime (right) we find a broad distribution of eigenvalues, often unstable, reflecting the complexity of the chaotic attractor.

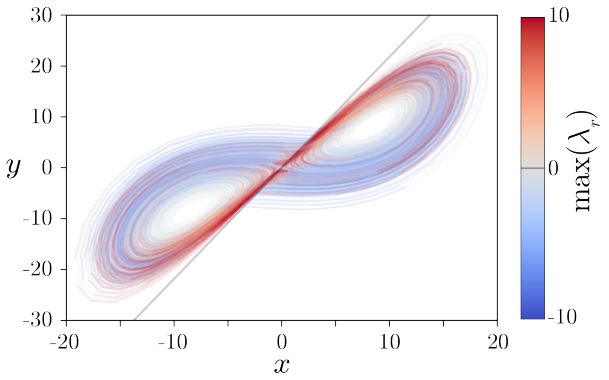

Figure 3.3: **Unstable linear models in the chaotic regime of the Lorenz system lie along the unstable manifold of the origin.** We plot the xy projection of the Lorenz system in the chaotic regime, color coded by the magnitude of the maximum real eigenvalue λ_r of the linear model found in each window resulting from the adaptive segmentation. Most unstable models are found close to the origin, along its $1d$ unstable manifold (gray line).

displaying unstable dynamics along the one-dimensional unstable manifold of the origin, Fig. (3.3). In the locally-linear perspective, the complexity of chaotic dynamics is associated with both substantial structure in the space of models as revealed through hierarchical clustering, as well as a wide range of dynamics, including eigenvalues that are broadly distributed across the instability boundary.

3.4. POSTURE DYNAMICS OF *C. elegans*

The posture dynamics of the nematode *C. elegans* is accurately represented by a low dimensional time series of "eigenworm" projections [36], Fig. (3.4A), though a quantitative understanding of the behaviors in these dynamics remains a topic of active research [37–40]. More broadly, principled behavioral analysis is the focus of multiple recent advances in the video imaging of unconstrained movement across a variety of organisms [13, 25, 41–48]. Here, we apply adaptive locally-linear analysis to the eigenworm time series and find short model window lengths ranging from approximately 0.6 s to 1.2 s, Fig. (3.4B). Notably the median model window size is similar to the duration of half a worm's body wave suggesting that the body wave dynamics provide an important timescale of movement

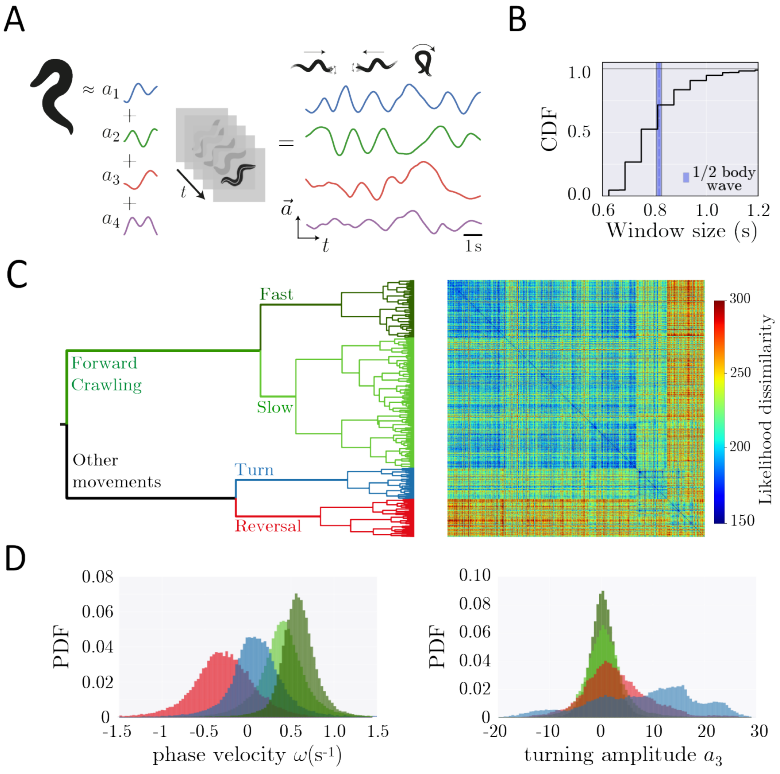

Figure 3.4: **Locally-linear analysis of *C. elegans* posture dynamics reveals a rich space of behavioral motifs.** (A) We transform image sequences into a 4D posture dynamics using "eigenworm" projections [36] where the first two modes (a_1, a_2) describe a body wave, with positive phase velocity ω for forward motion and negative ω when the worm reverses. High values of $|a_3|$ occur during deep turns, while a_4 captures head and tail movements. (B) The cumulative distribution (CDF) of window sizes reveals rapid posture changes on the timescale of the locomotor wave (the average duration of a half body wave is shown for reference). (C) Likelihood-based hierarchical clustering of the space of linear posture dynamics. At the top of the tree, forward crawling models separate from other behaviors. At the next level, forward crawling splits into fast and slower body waves, while the other behaviors separate into turns and reversals. Hierarchical clustering results in a similarity matrix with weak block structure; while behavior can be organized into broad classes, large variability remains within clusters. (D) Cluster branches reveal interpretable worm behaviors. We show the probability distribution (PDF) of body wave phase velocities and turning amplitudes at the 4-branch level of the tree. In the first forward state (dark green) worms move faster than in the second branch (light green). In the turn branch (blue), the phase velocity is centered around zero and high values of $|a_3|$ indicate larger turning amplitudes. In the reversal branch (red) we find predominantly negative phase velocities.

control.

Likelihood-based model clustering reveals that forward crawling separates from other worm behaviors at the top level of the hierarchy, Fig. (3.4C). At a finer scale, forward crawling breaks into faster and slower models, while turns and reversals emerge from the other branch. To clarify the structure of the model space we leverage the interpretability of the eigenworm projections where the first two modes (a_1 and a_2) capture a primary body wave oscillation with phase velocity $\omega = -\frac{d}{dt}\tan^{-1}(a_2/a_1)$ while a third projection a_3 captures broad body turns [36]. In Fig. (3.4D) we show ω and a_3 for each cluster. We note that there are a few low amplitude positive phase velocities in the reversal branch: the adaptive segmentation detects a dynamical break when the worm starts slowing down in preparation for a reversal, and those first frames are included in the reversal window. We note that changes in the activity of AIB, RIB and AVB neurons also precede the reversal event [49]. At a coarse level, the canonical behavioral states described since the earliest observations of the movements of *C. elegans* [50, 51] are identified here using data-driven, quantitative methods.

The full structure of the model dendrogram reveals that the behavioral repertoire of *C. elegans* is far more complicated than the canonical states of forward, reversal and turning locomotion. For example, forward crawling behavior is rich and variable: two forward crawling models can be almost as dissimilar as a turn is from a reversal. While the worm's behavior is stereotyped at a coarse-grained level, there is significant variation within each of the broad behavioral classes. For example at the 12-branch level of the tree, the reversal class splits into faster and slower reversals as well as new behavioral motif: a reversal-turn, Fig. (3.5). Certainly, some of these "states" simply reflect the linear basis of the segmentation algorithm. However, longer nonlinear behavioral sequences can emerge from analysis of the resulting symbolic dynamics.

We analyze the spectrum of eigenvalues across the entire model space, Fig. (3.6A), and find that the worm's dynamics includes both stable and unstable eigenvalues with a broad peak at $f \sim 0.6\,\mathrm{s}^{-1}$, in agreement with the average forward undulatory frequency of the worm in these food-free conditions [36]. Some of these unstable dynamics are explained by coarse behavioral transitions and we align reversal trajectories by the moment when the body wave phase velocity ω crosses zero from above in or-

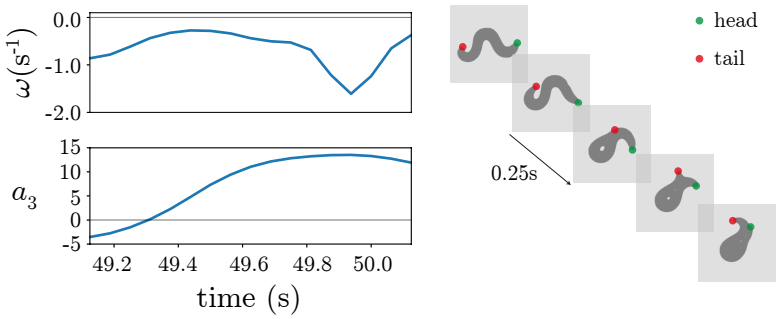

Figure 3.5: **At a 12-branch level of the dendrogram the reversal branch exhibits a reversal-turn behavioral motif.** (left) Example trajectory of a reversal-turn. A negative phase velocity ω is accompanied by a peak in a_3 for which the body is bent as in an Ω-turn. (right) Worm images from the example trajectory sampled each 0.25 s. The head and tail are identified with a green and red dot, respectively.

der to follow the median of the least stable eigenvalues during this transition, Fig. (3.6B). We see that the reversal behavior is accompanied by an apparent Hopf bifurcation: a pair of complex conjugate eigenvalues crosses the instability boundary. More generally, we find that the dynamics rapidly switches stability, Fig. (3.6C). Indeed the spectrum of eigenvalues shows that the worm's dynamics is generically near the instability boundary which is suggestive of a general feature of flexible movement control.

NEURAL DYNAMICS OF *C. elegans*

With recent progress in neural imaging, *C. elegans* also provides the opportunity to observe whole-brain dynamics at cellular resolution [49, 52–56] and we apply our techniques to analyze the differences between active and quiescent brain states driven by changes in oxygen (O_2) concentration [53]. In these experiments, worms enter a "sleep"-like state when the O_2 levels are lowered to 10%, and were aroused when the O_2 concentration is increased to 21%. These conditions offer a probe of the neural dynamics of *C. elegans* and also suggest qualitative comparisons with sleep transitions measured through electrocorticography (ECoG) in human and non-human primates [12, 57, 58].

In Fig. (3.7A) we show an example trace of the recorded neural activity and further details are available in Methods. We analyze the stability

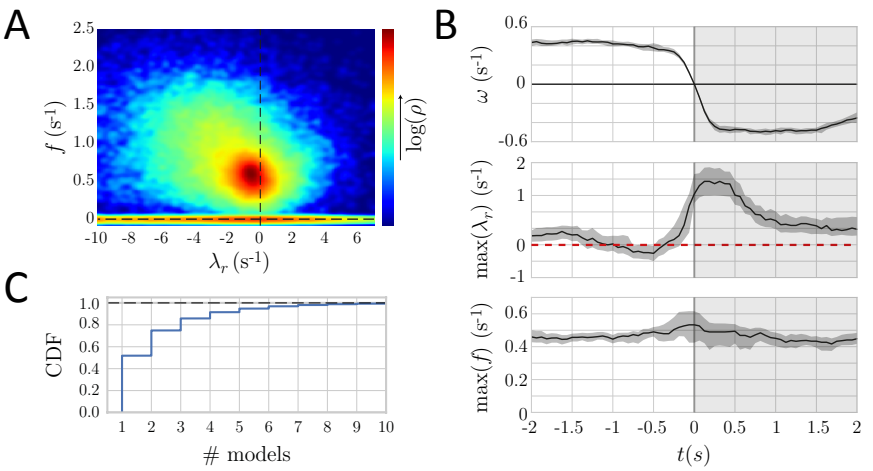

Figure 3.6: **Linear posture dynamics in *C. elegans* is distributed across an instability boundary with spontaneous reversals evident as a bifurcation.** (A) The eigenvalues of the segmented posture time series reveal a broad distribution of frequencies $f = |\mathrm{Im}(\lambda)|/2\pi$ with a peak $f \sim 0.6\,\mathrm{s}^{-1}$ that spills into the unstable regime. (B) We align reversal events and plot the maximum real eigenvalue (λ_r) and the corresponding oscillation frequency. As the reversal begins, the dynamics become unstable, indicating a Hopf-like bifurcation in which a pair of complex conjugate eigenvalues crosses the instability boundary. The shaded region corresponds to a bootstrapped 95% confidence interval. (C) Instabilities are both prevalent and short-lived. We show the cumulative distribution of the number of consecutive stable or unstable models demonstrating that bifurcations also occur on short-times between fine-scale behaviors.

of the neural dynamics using "active" and "quiescent" global brain states identified previously [53] and we show the distribution of least-stable dynamical eigenvalues for each condition, Fig. (3.7B). To further characterize the transition between states, we align the maximum real dynamical eigenvalues by the time of increased O_2 concentration and show the mean of this distribution, Fig. (3.7C). As activity increases from the quiescent state, the dynamics move towards the instability boundary, eventually crossing and remaining nearly unstable in the aroused state. While the neural imaging occurred in paralyzed worms, the broad distribution of eigenvalues across the instability boundary in the active brain state is consistent with the complexity of the behavioral dynamics. Notably, the model space also contains clusters in good correspondence with previously hand-labelled states, both in these experiments [53] and in worms exhibiting more complex natural behaviors [49], see Fig. (S5) and Fig. (S10) of [1].

3.5. HIGHER DIMENSIONAL SYSTEMS

Beyond the previous examples, there are situations where high dimensionality and low sampling rate (relative to the signal correlation time) yield a minimum window size which is too large to capture important dynamics. This is as expected–more dimensions generally require more statistical samples–and our minimum window size is chosen conservatively to result in a good model fit without regularization and thus without bias. If the sampling rate is adequate then we can easily apply our technique to higher dimensional data, as we demonstrate in Fig. (3.8A) where we show the analysis of 40 components from ECoG recordings in non-human primates. In two sessions, the same monkey was subject to the injection of an anesthetic drug (propofol) and induced into an unconscious state. The locally-linear dynamics exhibits a wide range of frequencies and is poised at the boundary between stability and instability, Fig. (3.8B). Clustering the model space yields interpretable dynamics, with different levels of awareness corresponding to different model clusters, Fig. (3.8C,E). The injection of propofol stabilizes the dynamics, with the largest real eigenvalue dropping momentarily, Fig. (3.8D-top). The stabilization of the dynamics is accompanied by an increase in the window sizes, Fig. (3.8) and a reduction in the excited frequencies, with the whole-brain dynamics entering low frequency states s_1 and s_2, Figs. (3.8D-bottom,3.8E). The two

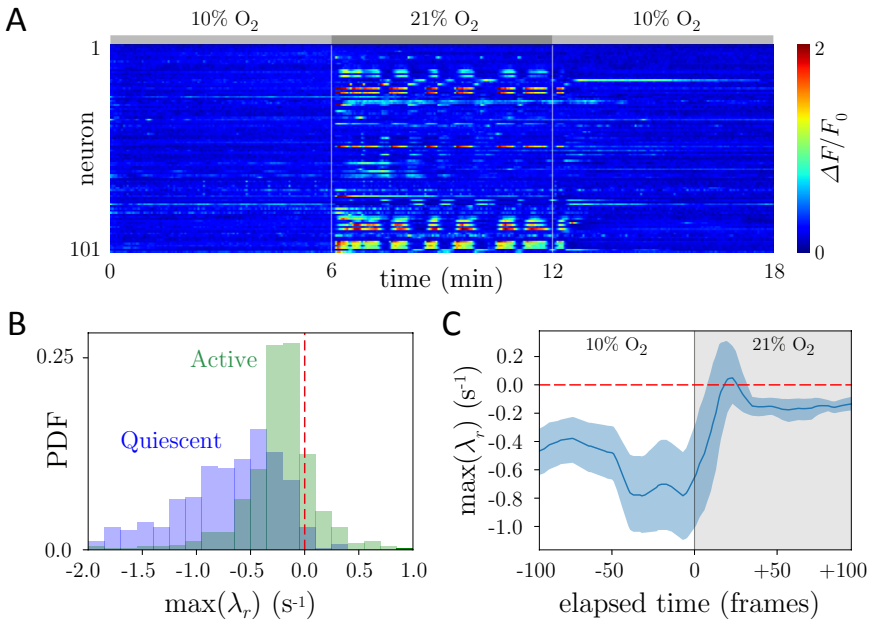

Figure 3.7: **Quiescence stabilizes global brain dynamics in *C. elegans*.** (A) We analyze whole-brain dynamics from previous experiments in which worms were exposed to varying levels of O_2 concentration [53]. We show the background subtracted fluorescence signal $\Delta F/F_0$ from 101 neurons while O_2 concentration changed in 6 minute periods: low O_2 (10%) induces a quiescent state; high O_2 (21%) induces an active state. (B) We plot the distribution of maximum real eigenvalues (λ_r) for the active and quiescent states. The active state is associated with substantial unstable dynamics, while the dynamics of the quiescent state is predominately stable which is consistent with putative stable fixed point dynamics. (C) We plot the average maximum real eigenvalue as the O_2 concentration is changed. We align the time series from different worms to the first frame of increased O_2 concentration and show the accompanying increase in the maximum real eigenvalue, which crosses and remains near to the instability boundary. The shaded region corresponds to a bootstrapped 95% confidence interval and curves were smoothed using a 5-frame running average.

different sessions differ in their average anesthetized state: while in session 1 the dynamics sits more in s_1, in session 2 we find a higher occupancy of s_2. Nonetheless, compared to any other cluster, both s_1 and s_2 have their high frequency dynamics significantly more damped. This loss of power in the β band has been associated with loss of consciousness [59, 60] and is naturally captured by our technique. The dynamics then slowly relaxes towards higher frequency states (s_3, s_4 and s_5) and the eigenvalue spectrum moves towards the instability boundary Figs. (3.8Dtop,3.8E).

For sparsely sampled systems on the other hand, regularization is generally required to accurately compute the inverse of the data and error covariance matrices. We offer one straightforward procedure which is motivated by Principal Component Regression [61] where we reduce the dimension locally, within each window. We detail this idea in Methods and provide a demonstration from recordings of hundreds of neurons in mouse visual cortex Figs. (3.9B), see also Fig. (S7) in [1]. In both of these high-dimensional systems, the local-linear analysis yields model dynamics that sit near the instability boundary, with a large fraction of unstable models, Figs. (3.8,3.9).

3.6. DISCUSSION

Simple linear models form the foundation for our analysis of complex time series based upon interpretable dynamics in short segments determined adaptively from data. The trajectories of a single model can only exponentially grow, decay or oscillate. Yet, by tiling the global dynamics with many such models we faithfully reproduce nonlinear, multidimensional and nonstationary behavior and parameterize the full dynamics with the set of local couplings. To elucidate the resulting space of models, we constructed hierarchical clusters with a new likelihood-based dissimilarity measure between local dynamics, and we examined the distribution and stability of the dynamical eigenvalues.

In the Lorenz system, chaos is distinguished by an increased model variety, including many with instabilities. In the chaotic attractor, the model hierarchy naturally splits across the two lobes with the clusters at deeper levels forming a progressively finer partition of the phase space. These partitions, as well as the recurrence structure in the space of models, can be used to estimate ergodic properties of the attractor such as the

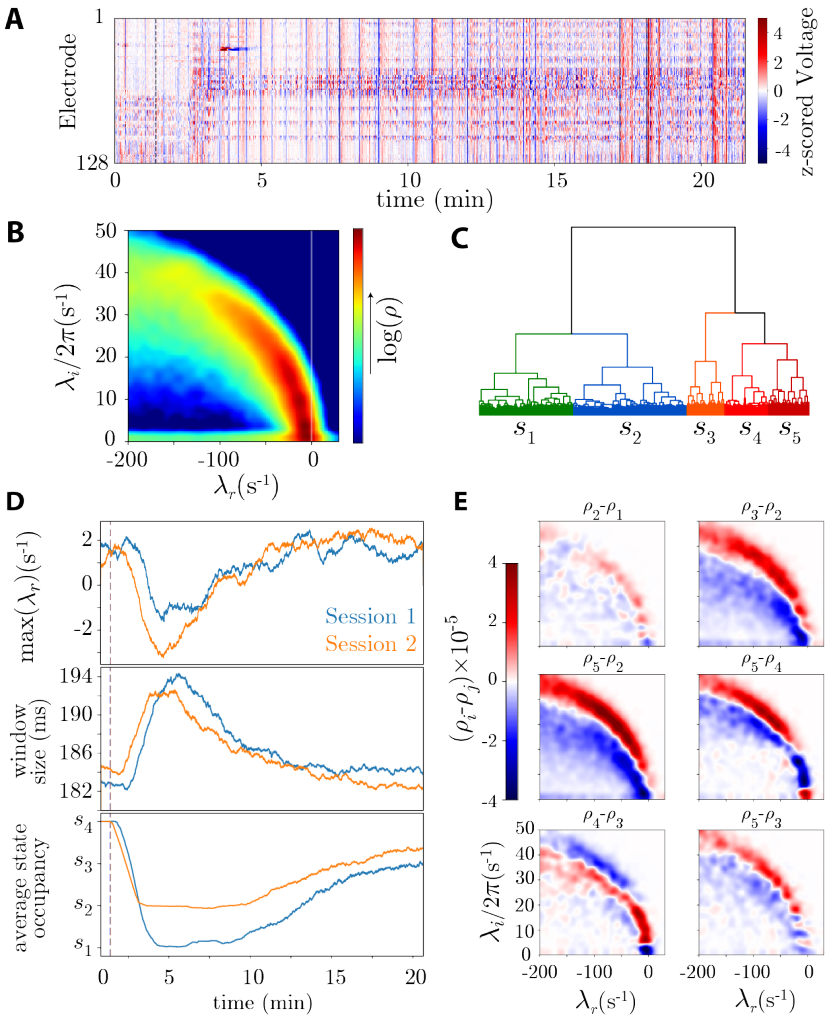

Figure 3.8: **Locally-linear analysis in the higher-dimensional context of electrocorticography recordings from non-human primates.** (A) Example z-scored voltage trace: injection of propofol (dashed line) induces anesthesia in the monkey subject. (B) Eigenvalue spectrum of the collection of linear models. The distribution of eigenvalues spans a wide range of frequencies and peaks near the instability boundary. (C) Dendrogram of the likelihood clustering of the space of models. (D) Propofol injection (dashed line) induces changes in brain dynamics. (top) The injection induces the stabilization of the dynamics for a transient period, followed by a slow relaxation towards the instability boundary. (middle) The window sizes increase after the injection of the anesthetic drug, reflecting a period in which the dynamics is less nonlinear. (bottom) Anesthesia pushes the dynamics to the low frequency states, s_1 and s_2. The curves were smoothed using a 1 s running average. (E) Difference between the eigenvalue distributions of different clusters. In general, the clusters exhibit frequency dependent changes in stability. Higher frequency states in s_1 and s_2 are damped, while frequencies in the δ band are long-lived. s_2 exhibits a minor increase in power in the θ and α bands compared to s_1. In contrast, states s_3, s_4, and s_5 exhibit higher amplitude high frequency dynamics, particularly in the β and γ bands.

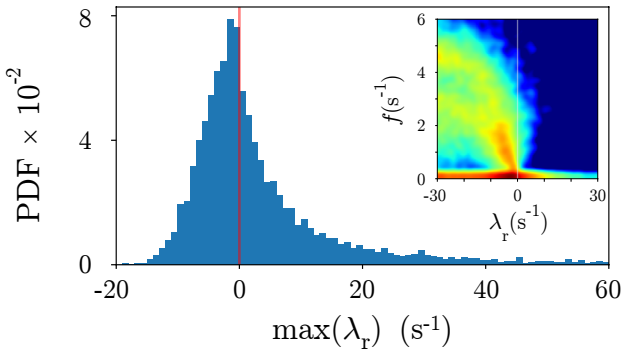

Figure 3.9: **Near-critical behavior in a population of hundreds of neurons from mouse visual cortex.** Distribution of the least stable real eigenvalues from each window of the local linear models obtained in recordings of 240 neurons in the visual cortex of *Mus musculus*. The inset shows the full distribution of eigenvalues - color code is the same as in Fig. (3.4). Here, due to the high-dimensionality, a regularization procedure was added to the original technique (Methods).

Kolmogorov-Sinai entropy [62, 63]. Adaptive locally-linear analysis offers a new approach for thinking quantitatively about animal behavior, where recent advances have resulted in multiple efforts aimed at understanding movement at high resolution [13, 36, 37]. In the posture dynamics of *C. elegans* we found that interpretable behavioral motifs emerged naturally, with high-level clusters reflecting canonical behavioral states of forward, reversal and turning locomotion [50] and finer-scale, novel states appearing deeper in the tree. An advantage of our clustering approach is that the level of behavioral description can be chosen appropriate to the nature of the analysis and these states form a natural basis with which to apply techniques such as compression [37, 64] and to explore longer-time behavioral dynamics through state transitions [13]. The dissimilarity measure also enables the comparison of models across datasets, regardless of experimental details such as frame rate, as long as postures are projected into the same basis. This can be useful for developing a master repertoire of behaviors [37] as well as looking for differences between nematode species or studying perturbations to behavior [36, 39, 51, 64–67]. We note that the success of the local linear basis in revealing interpretable worm behavior results in part from the ability to capture oscillations and the interactions between different posture modes, both common compo-

nents of movement behavior.

The eigenvalues of the posture dynamics reflect variability and hint at the presence of flexible control. While the eigenvalue distribution is centered on the frequency of the locomotor wave, the peak is close to the instability boundary and many models are unstable. Posture movements thus appear more complex than suggested by a model of stereotyped behaviors composed of a small collection of simple limit cycles [68].

The global neural activity of *C. elegans* also displays model dynamics which fluctuate across the instability boundary Fig. (3.7B), suggesting a near-critical brain state (see [69] for a similar, recent conclusion from a statistical perspective). Additionally, we obtained similar findings through local linear analysis of ECoG in monkey and single-cell recordings from a neural population in mouse visual cortex, Fig. (3.9). Such behavior was previously observed in whole brain activity [12, 57] and is consistent with the observation that the firing rate of neural populations exhibits subcritical dynamics [70]. Dynamical criticality is advantageous for information processing in models of neural networks [71, 72] and can occur as a result of an anti-Hebbian balance of excitation and inhibition [33]. Close to criticality, the dynamics is highly susceptible to external perturbations and small changes to the stability can have a dramatic impact on the dynamical time scales [73]. This susceptibility can change across brain regions [74] and we show that it can also be modulated with behavioral transitions and neural quiescence in *C. elegans*. Such modulation also occurs with the induction of anesthesia in ECoG [58], Fig. (3.8).

For simplicity and interpretability, we chose a basis of first-order linear models, though extensions to higher order are straightforward. Also, while we have focused on the deterministic model properties, the error terms ((3.1), Methods) may also carry important information. For example, it has been recently shown that even deterministic chaotic systems can be accurately represented as linear dynamics with a heavy-tailed stochastic forcing, the magnitude of which can be used to identify bursting or lobe switching events [75]. In our analysis we find that the error distribution exhibits heavy tails along the direction of the nonlinearities of the Lorenz system, and that the magnitude increases with lobe switching in the Lorenz system or reversal events in *C. elegans*.

There have been multiple recent advances in applying linear models to the analysis of complex time series [25–27, 76, 77] and while our ap-

proach shares a linear basis, there are important differences. For example, both autoregressive hidden Markov models and switching linear dynamical systems assume that the dynamics is composed of a set of discrete coarse-grained dynamical modes, revisited by the system. The number of these modes is a hyperparameter of the model, chosen to balance model complexity and accuracy. In contrast, our analysis finds as many linear models as permitted by reliable estimation and the depth of the hierarchical clustering can be chosen *a posteriori* depending on the interpretation of the clusters. Our combination of adaptive segmentation and hierarchical clustering also enables the explicit examination of the variability of models within each cluster. The combination of the simplicity of linear models with the power of the statistical methods yields a compelling route for the deeper understanding of complex dynamics and we expect our approach to be widely applicable.

3.7. METHODS

LINEAR DYNAMICS AND THE LIKELIHOOD FUNCTION

We approximate a given time series using first-order linear dynamical systems in short windows and use a likelihood-ratio test to estimate whether new observations can be modeled by the linear coefficients. Given a d-dimensional discrete time series $\vec{x} \in \mathbb{R}^d$, we define the first order vector autoregressive process,

$$\vec{x}_{t+1} = \vec{c} + \mathbf{A}\vec{x}_t + \vec{\eta}_{t+1}, \tag{3.1}$$

where $\vec{c} \in \mathbb{R}^d$ is an intercept vector, $\mathbf{A}$ is a $d \times d$ discrete time coupling matrix and $\vec{\eta}$ is a noise term with covariance Σ, which we assume to be Gaussian and white. We estimate the linear parameters $\theta = (\vec{c}, \mathbf{A}, \Sigma)$ through least squares regression. The continuous time linear couplings, ϕ, can be obtained by taking

$$\phi = \frac{\mathbf{A} - \mathbb{1}_d}{\Delta t}, \tag{3.2}$$

where $\mathbb{1}_d$ is a d-dimensional identity matrix and Δt is the inverse of the sampling rate.

Using windowed data $X_{k+1} = \vec{x}_t, t \in [t_0, t_0 + w_{k+1}]$ we construct the log-

likelihood ratio between models with parameters θ_k and θ_{k+1} as

$$\Lambda_{k,k+1} = l(\theta_{k+1}|X_{k+1}) - l(\theta_k|X_{k+1}). \tag{3.3}$$

where the pseudo log-likelihood function of model parameters $\theta_a = (\vec{c}_a, \mathbf{A}_a, \Sigma_a)$ from X_b for a Gaussian process is given by

$$l(\theta_a|X_b) = -\frac{1}{2}\sum_{t=t_0+1}^{w_b}\left\{\log\left[(2\pi)^d|\Sigma_a|\right] - \vec{\eta}_t^{\top}\Sigma_a^{-1}\vec{\eta}_t\right\}, \tag{3.4}$$

where $\vec{\eta}_t$ is the error of modeling X_b with θ_a.

ADAPTIVE LOCALLY-LINEAR SEGMENTATION ALGORITHM

We first define a set of candidate windows in which to examine whether there are dynamical breaks. This is done iteratively: we set a minimum window size w_{min} and then increment by ~ 10% which ensures that larger windows contain a proportionally larger number of observations. The candidate windows range between w_{min} and some w_{max} which corresponds to the value at which the step size is larger or equal to w_{min}. The specific value of w_{min} depends on the dataset and the dimensionality d and we chose w_{min} to be the smallest interval in which the data can be reliably fit. However, simply setting $w_{min} = d$ does not incorporate the possibility of multicollinearity, when two or more components are not linearly independent, which produces an ill-conditioned linear regression. This linear dependence results in a moment matrix $\mathbf{X}^{\top}\mathbf{X}$ that is not full rank or nearly singular, and therefore small perturbations result in large fluctuations in the estimated linear parameters. In addition, computing the log-likelihood function (3.4) requires inverting the covariance matrix of the error Σ. Thus, we require a minimum window size for which both $\mathbf{X}^{\top}\mathbf{X}$ and Σ are well-conditioned. We compute the condition number of these matrices as a function of window size and choose w_{min} as the smallest window for which the condition numbers are reasonably small. The results for each analyzed dataset are shown in Fig. (3.10).

Given a set of candidate windows we iterate over pairs of consecutive windows of size w_k and w_{k+1}, estimate the respective model parameters θ_k and θ_{k+1}, and locate a dynamical break if θ_{k+1} performs significantly better than θ_k in fitting the data from the window of size w_{k+1}. We assess significance through a likelihood ratio test and obtain $\Lambda_{k,k+1}$ from (3.3). We

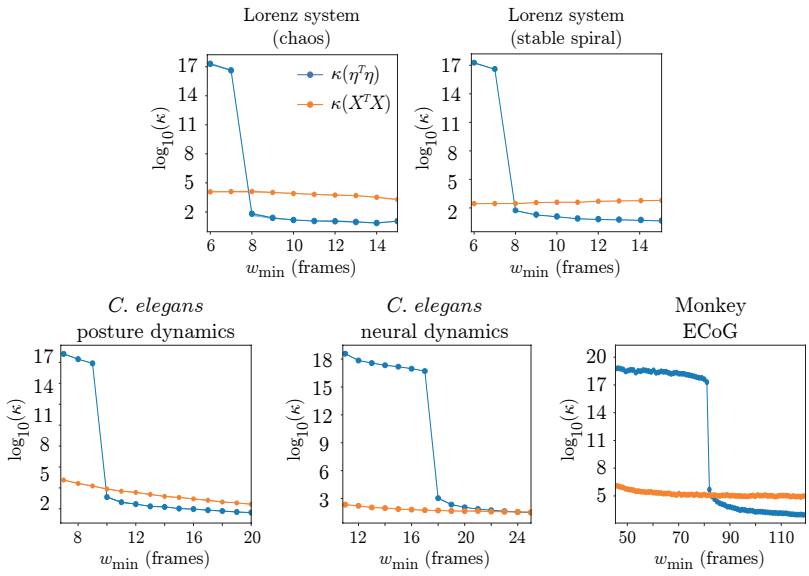

Figure 3.10: **Condition number of the moment matrix $\mathbf{X}^\top\mathbf{X}$ and the error covariance matrix $\eta^\top\eta$ as a function of window size.** We select the minimum window size as the smallest number of frames for which the model fit and log-likelihood estimation are well-conditioned. The condition number of $X^\top X$ and $\eta^\top\eta$ is calculated for different window sizes, and the median is estimated across samples taken randomly at different times in the time series. There is a drastic decrease in the condition number beyond a minimum window whose size depends on the data. Beyond this window, the model fit and log-likelihood estimation are well-conditioned.

note that our models are non-nested for which the likelihood ratio would be asymptotically χ^2 distributed. Instead, we take θ_k as a null model for the observations in the window of size w_{k+1} and use a Monte Carlo approach to generate $N = 5000$ surrogate trials of size w_{k+1} from θ_k in order to compute $P_{\text{null}}(\Lambda)$, the distribution of the log-likelihood ratio under the null hypothesis of having no model change. We identify a dynamical break if $\Lambda_{k,k+1} > \Lambda_{\text{thresh}}$ where Λ_{thresh} is defined by the larger solution of $P_{\text{null}}(\Lambda_{\text{thresh}}) = 0.05$. A graphical representation of the technique is shown in Fig. (3.1) and the algorithm is detailed in the Supplementary Information (SI). Finally, if the algorithm iterates to the maximum window size w_{max} we automatically assign a break which we then asses through the following procedure: we start with $w_k = w_{\text{min}}$ and compare the models found in the intervals $[w_{\text{max}} - w_k, w_{\text{max}}]$ and $[w_{\text{max}} - w_k, w_{\text{max}} + (w_{k+1} - w_k)]$ as we increase k until we span the entire set of candidate windows. If none of these tests suggest a break then we simply remove it.

We choose the significance threshold empirically and this choice reflects a tension between model complexity and accuracy; varying $P_{\text{null}}(\Lambda_{\text{thresh}})$ principally changes the number of breaks. While we have found $P_{\text{null}}(\Lambda_{\text{thresh}}) = 0.05$ to be reasonable across multiple datasets we provide additional intuition through a toy segmentation problem illustrated in Fig. (S9) of [1].

REGULARIZATION FOR HIGH-DIMENSIONAL DATA

Regularization can be incorporated straightforwardly into our method: at each iteration step we project the windows of size w_k and w_{k+1} to a space of orthogonal vectors defined by the first D eigenvectors of the covariance matrix of the window of size w_{k+1}, estimate whether a break exists in this lower dimensional space, and then project back the inferred model parameters to the original space through a simple linear transformation. The number of eigenvectors is chosen to keep the condition number of the covariance matrix of the data and the error below a certain threshold κ_{thresh} in order to ensure a well-conditioned model fit. We chose to use the condition number instead of the fraction of explained variance as a threshold, such that we can capture as much of the variance while being able to have a well-conditioned model fit. This results in projections that can capture more of the variance than that imposed by a variance threshold. We set the minimum window size at 10 frames, such that w_{k+1} is at least 10% larger than w_k (as in Algorithm 1 of the Supplementary In-

formation). We demonstrate this regularization procedure on a dataset consisting of calcium imaging of hundreds of neurons in the mouse visual cortex Figs. (3.9). Other approaches such as lasso or ridge regression may also be incorporated, but at the cost of additional regularization parameters [78, 79].

LIKELIHOOD-BASED HIERARCHICAL CLUSTERING

The space of linear dynamical systems has a family of equivalent representations given by the transformation $P \in \mathrm{GL}(n)$ of the group of non-singular $n \times n$ matrices and thus the Euclidean metric is not an appropriate dissimilarity measure. While previous solutions have been presented for measuring LDS distances [80, 81], the adaptation of these methods to our framework would be intricate and unnatural and we instead define a likelihood dissimilarity measure, which is consistent with the adaptive segmentation method. In essence, two models are distant if the model found by combining the two corresponding windows is unlikely to fit either window. On the other hand, when the models are similar, then the model found by combining the two windows is very likely to fit both windows. Specifically, let $\Lambda_{c,a} = l(\theta_a|X_a) - l(\theta_c|X_a)$ and $\Lambda_{c,b} = l(\theta_b|X_b) - l(\theta_c|X_b)$. We define the dissimilarity between models θ_a and θ_b as,

$$d_{a,b} = \Lambda_{c,a} + \Lambda_{c,b}, \tag{3.5}$$

where $X_c = X_a \cup X_b$, and θ_c is the result of fitting X_c to (3.1). This measure is positive semi-definite since $\Lambda_{c,a} \geq 0$ and $\Lambda_{c,b} \geq 0$ (θ_a is the maximum likelihood estimate in X_a; $l(\theta_a|X_a) - l(\theta_c|X_a) \geq 0$) and also symmetric; since we do not fit across windows, a first order linear fit in $X_a \cup X_b$ yields the same linear couplings as in $X_b \cup X_a$. After computing the dissimilarity between all linear models, we use Ward's criterion [34] to perform hierarchical clustering by minimizing the within-cluster variance.

DATA AND SOFTWARE

Lorenz data: We simulated the Lorenz system using the scipy.odeint package [82] with parameter choices $\sigma = 10$, $\beta = 8/3$ and $\rho = 28$ in the chaotic regime and $\rho = 20$ for spirals. We used step size $\Delta t = 0.02\,\mathrm{s}$. In the chaotic regime we integrated for a total of 1000 s, waiting 200 s for the trajectories to fall onto the attractor. For the stable spirals in the late-time transient chaos regime, we chose initial conditions $(x_0, y_0, z_0) = (x, 0, 20)$, where x

varied from −12 to −8 and 8 to 12 in steps of 0.2, yielding a total of 42 initial conditions. The trajectories were drawn to one of the stable fixed points $C_{\pm} = (x^*, y^*, z^*) = (\pm\sqrt{\beta(\rho-1)}, \pm\sqrt{\beta(\rho-1)}, \rho-1)$, for which linear stability analysis yields a stable oscillation with $\lambda_r \approx -0.4$ and $\lambda_i/(2\pi) \approx 1.4$ and a relaxation with $\lambda_r \approx -12.9$. We waited for 10 s before sampling the spiraling trajectory on additional 10 s. To reduce multi-collinearity we added small amplitude Gaussian white noise with a diagonal covariance matrix with variances $\sigma_{ii} = 0.001, \ \ i \in \{x, y, z\}$ to the simulated time series. The minimum window size $w_{min} = 10$ frames was chosen using Fig. (3.10).

***C. elegans* posture data** We analyzed previously published data consisting of foraging behavioral conditions [36, 83] in which N2-strain *C. elegans* were imaged at $f = 32$ Hz with a video tracking microscope. Coiled shapes were resolved and the time series downsampled to $f = 16$ Hz [39]. Worms were grown at 20°C under standard conditions [84]. Before imaging, worms were removed from bacteria-strewn agar plates using a platinum worm pick, and rinsed from *E. coli* by letting them swim for 1 min in NGM buffer. They were then transferred to an assay plate (9 cm Petri dish) that contained a copper ring (5.1 cm inner diameter) pressed into the agar surface, preventing the worm from reaching the side of the plate. Recording started approximately 5 min after the transfer, and lasted for 2100 s. In total, data from $N = 12$ worms was recorded. Using Fig. (3.10), we selected a minimum window size of $w_{min} = 10$ frames. Likelihood hierarchical clustering yielded a dendrogram for which a cut at the 4-branch level resulted in clusters with approximately 6500 (fast forward), 14400 (slow forward), 3500 (turns) and 4200 (reversals) models. In Fig. (3.6B), reversal events were identified when the phase velocity changes sign. Only segments for which there is a 2 s window of positive and negative phase velocity before and after the change of sign are considered.

***C. elegans* neural data** We analyzed whole-brain experiments from the Zimmer group in which transgenic *C. elegans* expressing a nuclear localized Ca^{2+} indicator were imaged in a microfluidic device where a reduction in O_2 concentration was observed to induce a "sleep"-like, quiescent state in *npr*-1 lethargus animals [53]. A range of 99-126 neurons was imaged for $N = 11$ worms and each neural trace was normalized by subtracting the background and dividing by the mean signal. A linear component was also subtracted to correct for bleaching. We used principal components analysis to reduce each ensemble recording to an 8-dimensional

time series capturing ~ 90% of the variance. Each of the experimental trials (one per worm) consisted of three 6 minute periods with alternating O_2 concentrations: starting with 10%, increasing to 21% and returning to 10%. We selected a minimum window size $w_{min} = 18$ frames using Fig. (3.10). Likelihood hierarchical clustering yielded a dendrogram for which a cut at the 3-branch level resulted in one cluster with 24 models, another with 74 models and a third outlier cluster containing just 1 model. Removing the outlier resulted in a dendrogram with a more even model distribution: one cluster with 24, another with 16 and a third with 55 models. We used this clustering to compare state labels with "active" and "quiescent" global brain states identified previously [53], Fig. (S5) of [1]. Data from unperturbed worms exhibiting more complex natural behaviors [49] was analyzed similarly.

Electrocorticography in monkey We analyzed a publicly available dataset (`http://neurotycho.org/`), that was previously described [5, 57, 85]. The details of the experimental procedure can be found in [86]. The raw 128 electrode signals were preprocessed in the following way. First, the original signal was downsampled from 1 KHz to 500 Hz. Then, two channels were removed due to significant line noise contamination. The remaining 126 electrodes were filtered to remove the line noise at 50 Hz and subsequent harmonics. Multi-taper filtering was performed using the Chronux toolbox [87], available at `http://chronux.org/`, with a bandwidth of 5 Hz (9 tapers) in a moving window of 2 s with 0.5 s overlap. The overlap regions were smoothed using a sigmoid function with smoothing parameter $\tau = 10$. Finally, the electrode signals were projected into 40 principal components that capture ~ 99% of the variance. We selected a minimum window size $w_{min} = 83$ frames using Fig. (3.10).

Mus musculus neural data We analyzed a publicly available dataset[2] from the Allen Institute [88]. The analyzed data constituted a total of 240 neurons from the anterolateral visual cortex of *Mus musculus*, at a depth of 275 μm. Neural activity was sampled at ~ 30 Hz for ~ 60 mins with a GCaMP6f calcium indicator, during exposure to a natural movie. The background subtracted bleach corrected signals were accessed using the Allen Software Development kit [89]. The local linear analysis was performed with regularization using a condition number threshold of $\kappa_{\text{thresh}} = 10^5$.

[2] `http://observatory.brain-map.org/visualcoding/search/cell_list?experiment_container_id=511854338&sort_field=p_sg&sort_dir=asc`

SOFTWARE

Code for the adaptive locally-linear segmentation and likelihood-based hierarchical clustering was written in Python [90] and is publicly available[3].

ACKNOWLEDGEMENTS

We thank SURFsara (www.surfsara.nl) for computing resources through the Lisa system. This work was supported by the research program of the Foundation for Fundamental Research on Matter (FOM), which is part of the Netherlands Organization for Scientific Research (NWO), and also by funding from The Okinawa Institute of Science and Technology Graduate University. GJS also acknowledges useful discussions at the Aspen Center for Physics, which is supported by National Science Foundation grant PHY-1607611.

[3] https://github.com/AntonioCCosta/local-linear-segmentation.git

REFERENCES

[1] A. C. Costa, T. Ahamed, and G. J. Stephens, *Adaptive, locally linear models of complex dynamics,* Proceedings of the National Academy of Sciences of the United States of America **116**, 1501 (2019).

[2] P. E. Arratia, G. A. Voth, and J. P. Gollub, *Stretching and mixing of non-Newtonian fluids in time-periodic flows,* Phys. Fluids **17**, 1 (2005).

[3] A. J. Majda and Y. Lee, *Conceptual dynamical models for turbulence,* Proceedings of the National Academy of Sciences of the United States of America **111**, 6548 (2014).

[4] B. Alakent, P. Doruker, and M. C. Çamurdan, *Time series analysis of collective motions in proteins,* J. Chem. Phys. **120**, 1072 (2004).

[5] T. Yanagawa, Z. C. Chao, N. Hasegawa, and N. Fujii, *Large-scale information flow in conscious and unconscious states: An ECoG study in monkeys,* PLoS ONE **8**, 1 (2013).

[6] K. Li, A. Javer, E. E. Keaveny, and A. E. Brown, *Recurrent neural networks with interpretable cells predict and classify worm behaviour,* NIPS (2017), 10.1101/222208.

[7] J. Pathak, Z. Lu, B. R. Hunt, M. Girvan, and E. Ott, *Using machine learning to replicate chaotic attractors and calculate lyapunov exponents from data,* Chaos **27**, 121102 (2017).

[8] S. L. Brunton, J. L. Proctor, and J. N. Kutz, *Discovering governing equations from data by sparse identification of nonlinear dynamical systems,* Proceedings of the National Academy of Sciences of the United States of America **113**, 3932 (2016).

[9] M. M. Churchland, J. P. Cunningham, M. T. Kaufman, J. D. Foster, P. Nuyujukian, S. I. Ryu, and K. V. Shenoy, *Neural population dynamics during reaching,* Nature **487**, 51 (2012).

[10] P. J. Schmid, *Dynamic mode decomposition of numerical and experimental data,* J. Fluid Mech. **656**, 5 (2010).

[11] B. W. Brunton, L. A. Johnson, J. G. Ojemann, and J. N. Kutz, *Extracting spatial-temporal coherent patterns in large-scale neural recordings using dynamic mode decomposition,* J. Neurosci. Methods **258**, 1 (2016).

[12] G. Solovey, K. Miller, J. Ojemann, M. Magnasco, and G. Cecchi, *Self-regulated dynamical criticality in human ECoG,* Front. Integr. Neurosci. **6**, 44 (2012).

[13] G. J. Berman, D. M. Choi, W. Bialek, and J. W. Shaevitz, *Mapping the stereotyped behaviour of freely moving fruit flies.* J. Royal Soc. Interface **11**, 1 (2014).

[14] V. Guralnik and J. Srivastava, *Event detection from time series data,* ICKDD 1999 , 33 (1999).

[15] J. I. Takeuchi and K. Yamanishi, *A unifying framework for detecting outliers and change points from time series,* T-KDE **18**, 482 (2006).

[16] Y. Wang, G. Sun, Z. Ji, C. Xing, and Y. Liang, *Weighted change-point method for detecting differential gene expression in breast cancer microarray data,* PLoS ONE **7** (2012), 10.1371/journal.pone.0029860.

[17] S. Liu, M. Yamada, N. Collier, and M. Sugiyama, *Change-point detection in time-series data by relative density-ratio estimation,* Neural Netw. **43**, 72 (2013).

[18] Y. Chen, B. Li, and L. Niu, *A local vector autoregressive framework and its applications to multivariate time series monitoring and forecasting,* Stat. Its Interface **6**, 499 (2013).

[19] N. Omranian, B. Mueller-Roeber, and Z. Nikoloski, *Segmentation of biological multivariate time-series data,* Sci. Rep. **5** (2015), 10.1038/srep08937.

[20] P. Preuss, R. Puchstein, and H. Dette, *Detection of multiple structural breaks in multivariate time series,* J. Am. Stat. Assoc. **110**, 654 (2014).

[21] Y. Kawahara, T. Yairi, and K. Machida, *Change-Point Detection in Time-Series Data Based on Subspace Identification,* ICDM 2007 , 559 (2007).

[22] J. D. Bryan and S. E. Levinson, *Autoregressive Hidden Markov Model and the Speech Signal,* Procedia Comput. Sci. **61**, 328 (2015).

[23] I. Stanculescu, C. K. I. Williams, and Y. Freer, *Autoregressive Hidden Markov Models for the Early Detection of Neonatal Sepsis,* IEEE J. Biomed. Health Inform. **18**, 1560 (2014).

[24] T. Gallagher, T. Bjorness, R. Greene, Y. J. You, and L. Avery, *The Geometry of Locomotive Behavioral States in C. elegans,* PLoS ONE **8** (2013), 10.1371/journal.pone.0059865.

[25] A. B. Wiltschko, M. J. Johnson, G. Iurilli, R. E. Peterson, J. M. Katon, S. L. Pashkovski, V. E. Abraira, R. P. Adams, and S. R. Datta, *Mapping Sub-Second Structure in Mouse Behavior,* Neuron **88**, 1121 (2015).

[26] S. Linderman, M. Johnson, A. Miller, R. Adams, D. Blei, and L. Paninski, *Bayesian Learning and Inference in Recurrent Switching Linear Dynamical Systems,* in *ICAIS 2017*, Proceedings of Machine Learning Research, Vol. 54, edited by A. Singh and J. Zhu (PMLR, 2017) pp. 914–922.

[27] J. E. Markowitz, W. F. Gillis, C. C. Beron, S. Q. Neufeld, K. Robertson, N. D. Bhagat, R. E. Peterson, E. Peterson, M. Hyun, S. W. Linderman, B. L. Sabatini, and S. R. Datta, *The Striatum Organizes 3D Behavior via Moment-to-Moment Action Selection,* Cell **174**, 1 (2018).

[28] S. B. Guthery, *Partition regression,* J. Am. Stat. Assoc. **69**, 945 (1974).

[29] D. M. Hawkins, *Point Estimation of the Parameters of Piecewise Regression Models,* J. R. Stat. Soc. Ser. C Appl. Stat. **25**, 51 (1976).

[30] F. Chamroukhi, S. Mohammed, D. Trabelsi, L. Oukhellou, and Y. Amirat, *Joint segmentation of multivariate time series with hidden process regression for human activity recognition,* Neurocomputing **120**, 633 (2013).

[31] M. A. Muñoz, *Colloquium: Criticality and dynamical scaling in living systems,* Reviews of Modern Physics **90**, 31001 (2018), arXiv:1712.04499 .

[32] M. O. Magnasco, O. Piro, and G. A. Cecchi, *Self-tuned critical anti-Hebbian networks,* Phys. Rev. Lett. **102**, 1 (2009).

[33] M. O. Magnasco, O. Piro, and G. A. Cecchi, *Dynamical and Statistical Criticality in a Model of Neural Tissue,* Phys. Rev. Lett. **102**, 1 (2009).

[34] J. H. Ward, *Hierarchical grouping to optimize an objective function,* J. Am. Stat. Assoc. **58**, 236 (1963).

[35] E. N. Lorenz, *Deterministic Nonperiodic Flow,* Journal of the Atmospheric Sciences **20**, 130 (1963), arXiv:NIHMS150003 .

[36] G. J. Stephens, B. Johnson-Kerner, W. Bialek, and W. S. Ryu, *Dimensionality and dynamics in the behavior of C. elegans.* PLoS Comput. Biol. **4**, e1000028 (2008).

[37] A. E. X. Brown, E. I. Yemini, L. J. Grundy, T. Jucikas, and W. R. Schafer, *A dictionary of behavioral motifs reveals clusters of genes affecting Caenorhabditis elegans locomotion,* Proceedings of the National Academy of Sciences of the United States of America **110**, 791 (2013).

[38] E. Yemini, T. Jucikas, L. J. Grundy, A. E. Brown, and W. R. Schafer, *A database of Caenorhabditis elegans behavioral phenotypes,* Nat Methods **10** (2013), 10.1038/nmeth.2560.

[39] O. D. Broekmans, J. B. Rodgers, W. S. Ryu, and G. J. Stephens, *Resolving coiled shapes reveals new reorientation behaviors in c. elegans,* eLife **5(e17227)** (2016), 10.7554/eLife.17227.

[40] M. Liu, A. K. Sharma, J. Shaevitz, and A. M. Leifer, *Temporal processing and context dependency in c. elegans response to mechanosensation,* eLife **7(e36419)** (2018), 10.7554/eLife.36419.

[41] G. J. Berman, W. Bialek, and J. W. Shaevitz, *Hierarchy and predictability in Drosophila behavior,* Proceedings of the National Academy of Sciences **104**, 20167 (2016).

[42] G. J. Berman, *Measuring behavior across scales,* BMC Biol. **16** (2018), 10.1186/s12915-018-0494-7.

[43] U. Klibaite, G. J. Berman, J. Cande, D. L. Stern, and J. W. Shaevitz, *An unsupervised method for quantifying the behavior of paired animals,* Phys. Biol. **14** (2017).

[44] A. J. Calhoun and M. Murthy, *Quantifying behavior to solve sensorimotor transformations: advances from worms and flies,* Curr. Opin. Neurobiol. **46**, 90 (2017).

[45] S. Han, E. Taralova, C. Dupre, and R. Yuste, *Comprehensive machine learning analysis of Hydra behavior reveals a stable behavioral repertoire,* eLife **7(e32605)** (2018), 10.7554/eLife.32605, 10.7554/eLife.32605 .

[46] B. Szigeti, A. Deogade, and B. Webb, *Searching for motifs in the behaviour of larval drosophila melanogaster and caenorhabditis elegans reveals continuity between behavioural states,* J. Royal Soc. Interface **12** (2015), 10.1098/rsif.2015.0899.

[47] J. G. Todd, J. S. Kain, and B. L. de Bivort, *Systematic exploration of unsupervised methods for mapping behavior,* Phys. Biol **14** (2017), 10.1088/1478-3975.

[48] A. M. Bruno, W. N. Frost, and M. D. Humphries, *A spiral attractor network drives rhythmic locomotion,* eLife **6(e27342)** (2017), 10.7554/eLife.27342.

[49] S. Kato, H. S. Kaplan, T. Schrödel, S. Skora, T. H. Lindsay, E. Yemini, S. Lockery, and M. Zimmer, *Global brain dynamics embed the motor command sequence of Caenorhabditis elegans,* Cell **163**, 1 (2015).

[50] N. A. Croll, *Behavioural analysis of nematode movement,* Adv. Parasitol. **13**, 71 (1975).

[51] R. F. Schwarz, R. Branicky, L. J. Grundy, W. R. Schafer, and A. E. X. Brown, *Changes in postural syntax characterize sensory modulation and natural variation of c. elegans locomotion,* PLOS Comput. Biol. **11**, 1 (2015).

[52] J. P. Nguyen, F. B. Shipley, A. N. Linder, G. S. Plummer, M. Liu, S. U. Setru, J. W. Shaevitz, and A. M. Leifer, *Whole-brain calcium imag-*

ing with cellular resolution in freely behaving caenorhabditis elegans, Proceedings of the National Academy of Sciences of the United States of America **113** (2016), 10.1073/pnas.1507110112.

[53] A. L. A. Nichols, T. Eichler, R. Latham, and M. Zimmer, *A global brain state underlies C. elegans sleep behavior,* Science **356** (2017), 10.1126/science.aam6851.

[54] T. Schrödel, R. Prevedel, K. Aumayr, M. Zimmer, and A. Vaziri, *Brain-wide 3D imaging of neuronal activity in Caenorhabditis elegans with sculpted light,* Nat. Methods **10** (2013), 10.1038/nmeth.2637.

[55] R. Prevedel, Y.-G. Yoon, M. Hoffmann, N. Pak, G. Wetzstein, S. Kato, T. Schrödel, R. Raskar, M. Zimmer, E. S. Boyden, and A. Vaziri, *Simultaneous whole-animal 3D imaging of neuronal activity using light-field microscopy.* Nat. Methods **11** (2014), 10.1038/nmeth.2964.

[56] V. Venkatachalam, N. Ji, X. Wang, C. Clark, J. K. Mitchell, M. Klein, C. J. Tabone, J. Florman, H. Ji, J. Greenwood, A. D. Chisholm, J. Srinivasan, M. Alkema, M. Zhen, and A. D. T. Samuel, *Pan-neuronal imaging in roaming Caenorhabditis elegans,* Proceedings of the National Academy of Sciences of the United States of America **113** (2016), 10.1073/pnas.1507109113.

[57] G. Solovey, L. M. Alonso, T. Yanagawa, N. Fujii, M. O. Magnasco, G. A. Cecchi, and A. Proekt, *Loss of Consciousness Is Associated with Stabilization of Cortical Activity,* J. Neurosci. **35**, 10866 (2015).

[58] L. M. Alonso, A. Proekt, T. H. Schwartz, K. O. Pryor, G. a. Cecchi, and M. O. Magnasco, *Dynamical criticality during induction of anesthesia in human ECoG recordings,* Front. Neural Circuits **8** (2014), 10.3389/fncir.2014.00020.

[59] Y. Ishizawa, O. J. Ahmed, S. R. Patel, J. T. Gale, D. Sierra-Mercado, E. N. Brown, and E. N. Eskandar, *Dynamics of Propofol-Induced Loss of Consciousness Across Primate Neocortex,* Journal of Neuroscience **36**, 7718 (2016).

[60] S. Chauvette, S. Crochet, M. Volgushev, and I. Timofeev, *Properties of slow oscillation during slow-wave sleep and anesthesia in cats,* Journal of Neuroscience **31**, 14998 (2011), arXiv:NIHMS150003 .

[61] I. T. Jolliffe, *A Note on the Use of Principal Components in Regression,* Journal of the Royal Statistical Society. Series C (Applied Statistics) **31**, 300 (1982).

[62] A. N. Kolmogorov, *On the entropy per unit time as a metric invariant of automorphisms,* Doklady of Russian Academy of Sciences **124**, 754 (1959).

[63] E. Ott, *Chaos in Dynamical Systems* (Cambridge University Press, 2002).

[64] A. Gomez-Marin, G. J. Stephens, and A. E. X. Brown, *Hierarchical compression of Caenorhabditis elegans locomotion reveals phenotypic differences in the organization of behaviour,* J. Royal Soc. Interface **13** (2016), 10.1098/rsif.2016.0466.

[65] A. Vidal-Gadea, S. Topper, L. Young, A. Crisp, L. Kressin, E. Elbel, T. Maples, M. Brauner, K. Erbguth, A. Axelrod, A. Gottschalk, D. Siegel, and J. T. Pierce-Shimomura, *Caenorhabditis elegans selects distinct crawling and swimming gaits via dopamine and serotonin,* Proceedings of the National Academy of Sciences of the United States of America **108**, 17504 (2011).

[66] S. Gao, S. A. Guan, A. D. Fouad, J. Meng, T. Kawano, Y. C. Huang, Y. Li, S. Alcaire, W. Hung, Y. Lu, Y. B. Qi, Y. Jin, M. Alkema, C. Fang-Yen, and M. Zhen, *Excitatory motor neurons are local oscillators for backward locomotion,* eLife **7(e29915)** (2018), 10.7554/eLife.29915.

[67] A. D. Fouad, S. Teng, J. R. Mark, A. Liu, P. Alvarez-Illera, H. Ji, A. Du, P. D. Bhirgoo, E. Cornblath, S. A. Guan, and C. Fang-Yen, *Distributed rhythm generators underlie Caenorhabditis elegans forward locomotion.* eLife **7(e29913)** (2018), 10.7554/eLife.29913.

[68] S. Revzen and J. M. Guckenheimer, *Finding the dimension of slow dynamics in a rhythmic system,* J. Royal Soc. Interface **9**, 957 (2012).

[69] X. Chen, F. Randi, A. M. Leifer, and W. Bialek, *Searching for collective behavior in a small brain,* **arXiv:1810.07623v1. Preprint, posted October 17, 2018.** (2018), arXiv:arXiv:1810.07623v1 .

[70] J. Wilting and V. Priesemann, *Inferring collective dynamical states from widely unobserved systems,* Nature Communications **9** (2018), 10.1038/s41467-018-04725-4, arXiv:1608.07035 .

[71] T. Toyoizumi and L. F. Abbott, *Beyond the edge of chaos: Amplification and temporal integration by recurrent networks in the chaotic regime,* Phys. Rev. E **84**, 1 (2011).

[72] D. Sussillo and L. F. Abbott, *Generating Coherent Patterns of Activity from Chaotic Neural Networks,* Neuron **63**, 544 (2009).

[73] J. Wilting, J. Dehning, J. P. Neto, L. Rudelt, M. Wibral, J. Zierenberg, and V. Priesemann, *Dynamic Adaptive Computation: Tuning network states to task requirements,* **arXiv:1809.07550v1. Preprint, posted September 20, 2018.** (2018), arXiv:1809.07550 .

[74] J. D. Murray, A. Bernacchia, D. J. Freedman, R. Romo, J. D. Wallis, X. Cai, C. Padoa-Schioppa, T. Pasternak, H. Seo, D. Lee, and X. J. Wang, *A hierarchy of intrinsic timescales across primate cortex,* Nature Neuroscience **17**, 1661 (2014).

[75] S. L. Brunton, B. W. Brunton, J. L. Proctor, E. Kaiser, and J. Nathan Kutz, *Chaos as an intermittently forced linear system,* Nat. Commun. **8**, 1 (2017).

[76] S. M. Oh, J. M. Rehg, T. Balch, and F. Dellaert, *Learning and inferring motion patterns using parametric segmental switching linear dynamic systems,* Int. J. Comput. Vis. **77**, 103 (2008).

[77] E. B. Fox, E. B. Sudderth, M. I. Jordan, and A. S. Willsky, *Nonparametric Bayesian Learning of Switching Linear Dynamical Systems,* NIPS (2009).

[78] A. E. Hoerl and R. W. Kennard, *Ridge Regression: Biased Estimation for Nonorthogonal Problemas,* Technometrics **12**, 55 (1970).

[79] F. Santosa and W. W. Symes, *Linear Inversion of Band-Limited Reflection Seismograms,* SIAM J. Sci. Stat. Comput. **7**, 1307 (1986).

[80] B. Afsari and R. Vidal, *The alignment distance on spaces of Linear Dynamical Systems,* CDC , 1162 (2013).

[81] A. Ravichandran, R. Chaudhry, and R. Vidal, *View-invariant dynamic texture recognition using a bag of dynamical systems,* Proc. of CVPR , 1651 (2009).

[82] E. Jones, T. Oliphant, P. Peterson, and et al., *SciPy: Open source scientific tools for Python,* (2001–).

[83] G. J. Stephens, M. Bueno de Mesquita, W. S. Ryu, and W. Bialek, *Emergence of long timescales and stereotyped behaviors in Caenorhabditis elegans.* Proc. Natl. Acad. Sci. U. S. A. **108**, 7286 (2011).

[84] J. E. Sulston and S. Brenner, *The DNA of Caenorhabditis elegans.* Genetics **77**, 95 (1974).

[85] S. Tajima, T. Yanagawa, N. Fujii, and T. Toyoizumi, *Untangling Brain-Wide Dynamics in Consciousness by Cross-Embedding,* PLOS Comput. Biol. **11**, 1 (2015).

[86] Y. Nagasaka, K. Shimoda, and N. Fujii, *Multidimensional recording (MDR) and data sharing: An ecological open research and educational platform for neuroscience,* PLoS ONE **6** (2011), 10.1371/journal.pone.0022561.

[87] P. Mitra and H. Bokil, *Observed Brain Dynamics* (Oxford University Press, New York, 2008).

[88] *Allen Institute for Brain Science. Allen Brain Observatory. Available at:* `http://observatory.brain-map.org/visualcoding/`, (2016).

[89] *Allen Institute for Brain Science. Allen SDK. Available at:* `https://allensdk.readthedocs.io/en/latest/`, (2015).

[90] G. Rossum, *Python Reference Manual*, Tech. Rep. (Amsterdam, The Netherlands, The Netherlands, 1995).

4

BRIDGING TIME SCALES THROUGH TRANSFER OPERATORS

4.1. INTRODUCTION

Biological phenomena are generally high dimensional and exhibit multi-scale dynamics in time and space. For example, stochastic fluctuations at the level of single molecules impact the behavior of cells, which will then impact the functioning of tissues/organs and therefore behavior. Naive statistical descriptions of such out-of-equilibrium systems often fail to capture important dynamics, while simple low dimensional approximations of the dynamics may hide subtle variations that are fundamental for a deeper mechanistic understanding.

Broadly speaking, we can think about such complexity through the language of differential equations. The state of the biological system, composed of a multiplicity of interacting degrees of freedom, evolves as,

$$\frac{dx}{dt} = F(x,t) + \gamma(x,t)\frac{dW}{dt}, \tag{4.1}$$

where $x \in X \in \mathbb{R}^D$, $F : \mathbb{R}^{D+1} \to \mathbb{R}^{D+1}$, $\gamma : \mathbb{R}^{D+1} \to \mathbb{R}^{D+1}$ and dW is a Wiener process. In general, biological processes will exhibit $D \gg 1$, and both $F(x,t)$ and $\gamma(x,t)$ may be complex non-linear functions, which makes dealing explicitly with such differential equations fundamentally challenging. In Chapter (2), we took a phenomenological approach and found a

Parts of this chapter are currently under review. [1]

set of variables for which most of the unpredictability could be subsumed into a Wiener process. This allowed us to find long time scale "roaming" and "dwelling" like states, in the form of an exploration-exploitation mode that captures the variation among nematode species. In Chapter (3), we focused on finer scale details of the postural dynamics, and developed an adaptive locally-linear parameterization of the postural time series that allowed us to learn fine-scale stereotyped states, as well as evidence of large variability within states. How can we combine the fine scale primitives of behavior (Chapter 3) to effectively generate the longer time scale exploration strategies found in Chapter 2?

In this chapter, we propose that a careful characterization of the system's state, combined with an operator theoretic treatment of the state-space dynamics, yields a powerful tool for bridging the gap between fine scale and coarse-grained phenomenological descriptions of behavioral dynamics. We will study the time evolution of ensemble of points in phase space, through the approximation of the Perron-Frobenius operator on phase space densities. By subsuming non-linearities into the finite rank approximation of the infinite dimensional operator, we learn an effective statistical description of the dynamics through a single linear operator. The eigenvalue spectrum of such operator provides a hierarchy of timescales, which may allow for time scale separation and an effective phenomenological description of the system through the long lived eigenfunctions, which capture important emergent coarse-grained properties of the dynamics, Fig. (5.1). This chapter serves as an introduction to the techniques that will be applied to explicitly bridge time scales in *C. elegans* behavior.

4.2. COARSE-GRAINING THE PHASE SPACE

We will study the time evolution of ensembles of points in state space. Instead of working directly with an ordinary differential equation, Eq. (4.1), we will work with a partial differential equation on densities, the Fokker-Planck equation,

$$\frac{\partial \rho}{\partial t} = -\nabla \cdot (F(x,t)\rho) + \frac{1}{2}\nabla \cdot \left[\nabla \cdot (\Gamma(x,t)\rho)\right], \tag{4.2}$$

where $\Gamma(x,t) = \gamma(x,t)\gamma(x,t)^\top$. The idea behind working with densities instead of the underlying equations of motions is that, in this way, we can

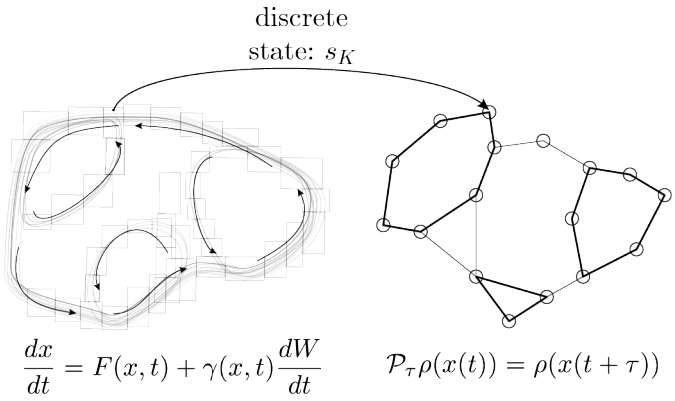

Figure 4.1: **Approximation of the transfer operator on densities.** Discrete states are built from continuous trajectories, such that we can study the flow of densities. We turn a finite dimensional differential equation (left) into a finite-rank approximation of an infinite dimensional operator (right). The spectral properties of the operator decompose the dynamics into spatio-temporal modes that capture the coarse-grained dynamics. Thick lines represent meta-stable states, which can be identified through the eigenfunctions of the operator.

abstract from the fine scale details of the dynamics and focus only on the ensemble behavior to extract coarse-grained emergent properties. In systems with a very large number of degrees of freedom, having access to the underlying equations of motion does not necessarily provide an understanding over the ensemble properties of the system. Much like how statistical mechanics abstracts from the dynamics of the molecules in a gas, here we try to focus only on the coarse-grained statistical properties of the dynamics and extract the emergent dynamical behavior of the system.

The time evolution of densities can also be studied through the operator associated with the infinitesimal generator of the Fokker-Planck equation, the Perron-Frobenius operator. Since our goal is to learn the emergent properties of the dynamics in a data-driven fashion, working within the operator theoretic framework offers substantial advantages. On the one hand, there is no need to learn the functional form of $F(x,t)$ and $\gamma(x,t)$. On the other hand, subsuming the non-linearities into the finite dimensional approximation of this infinite dimensional operator offers a complete description of the dynamics through a single linear operator,

whose spectrum provides a decomposition of the dynamics into a hierarchy of spatio-temporal modes. The Perron-Frobenius operator with respect to the transformation $S_\tau : X \to X$, which pushes the state forward by a time τ, is defined by the condition of conservation of mass [2],

$$\int_{S_\tau^{-1}(A)} f(x)\,d\mu = \int_A \mathscr{P}_\tau f(x)\,d\mu, \quad \text{for each } A \in \Sigma \tag{4.3}$$

where (X, Σ, μ) is a σ-finite measurable space, Σ denotes the σ-algebra of Borel sets, μ denotes the measure[1]. Therefore, $\mathscr{P}_\tau : L^1(X) \to L^1(X)$ acts on a set of probability density functions $D(X, \Sigma, \mu)$ defined by,

$$D(X, \Sigma, \mu) = \left\{\rho \in L^1(X, \Sigma, \mu) : \rho \geq 0 \text{ and } ||\rho|| = 1\right\}, \tag{4.4}$$

pushing them into the future by a time step τ,

$$\rho(t + \tau) = \mathscr{P}_\tau \circ \rho(t). \tag{4.5}$$

Conceptually, the operator corresponds to an infinite dimensional transition probability matrix. The spectrum of the transfer operator yields a hierarchy of modes, which decay to the invariant density on different time scales. For example, the eigenfunction of eigenvalue 1 of the Perron-Frobenius operator corresponds to the invariant density μ[2],

$$\mathscr{P}_\tau \mu = \mu. \tag{4.6}$$

The remaining eigenvalues of the Perron-Frobenius operator are bounded from above by $\lambda < 1$, and provide a hierarchy of eigenfunctions that relax towards the invariant distribution on different time scales, given by,

$$t_{\text{imp}} = \frac{-\tau}{\log|\lambda|}. \tag{4.7}$$

The closer eigenvalues are to one, the slower the eigenfunctions decay. Our approach essentially relies on the decomposition of the transfer operator into fast decaying modes and slow decaying modes that capture

[1] This essentially means that the full measure space is the union of a finite or countable family of sets with finite measure.

[2] For non-ergodic systems, the eigenvalue 1 can be degenerate indicating that the systems exhibits disjoint invariant sets.

the coarse-grained long time scale behavior of the system. In general, we look for a decomposition,

$$\rho(t+\tau) = \mathscr{P}_\tau^{\text{fast}} \circ \rho(t) + \mathscr{P}_\tau^{\text{slow}} \circ \rho(t), \tag{4.8}$$

where $\mathscr{P}_\tau^{\text{fast}}$ is captured by the fast decaying eigenfunctions ($\lambda \ll 1$), while $\mathscr{P}_\tau^{\text{slow}}$ is captured by the slow decaying eigenfunctions ($1-\lambda \ll 1$). Extracting these slow modes allows for the identification of sets that remain almost unaffected by the flow, known generally as coherent structures or metastable states [3–17]. Examples include learning protein conformations from short, off-equilibrium, molecular dynamics simulations [15], or identifying transport barriers in fluids [16]. In addition, in systems with a large time scale separation it is possible to learn effective lower dimensional phenomenological descriptions of the long time scale dynamical processes through the transfer operator formalism [11, 18].

Given the fact the Perron-Frobenius operator is infinite dimensional, we need to find finite-rank approximations of this operator. Recent years have seen a tremendous increase in data-driven approximation of the Perron-Frobenius operator and its adjoint, the Koopman operator, specially applied to fluid and molecular dynamics [3–17]. We will take a simple approach similar to [10], in which we build a finite dimensional approximation of the Perron-Frobenius operator using an Ulam-Galerkin discretization. A Galerkin projection takes the infinite dimensional operator onto an $N \times N$ operator of finite rank by truncating an infinite dimensional set of basis functions at N. Ulam's method uses characteristic functions as the basis for this projection,

$$\zeta_i(x) = \chi_{A_i}(x) = \begin{cases} 1, & \text{for } x \in A_i \\ 0, & \text{otherwise} \end{cases}. \tag{4.9}$$

This essentially means that we approximate the invariant measure as a piece-wise constant function, and the transfer operator as a Markov chain: we partition the phase space into N connected sets with nonempty and disjoint interior that covers M: $M = \cup_{i=1}^{N} A_i$, and approximate the operator by counting transitions from A_i to A_j in a finite time τ,

$$P_{i,j}(\tau, N) \approx \frac{\#(\{x | x(t) \in A_i \text{ and } x(t+\tau) \in A_j\})}{\#(\{x(t) \in A_i\})}. \tag{4.10}$$

The underlying dynamics in the full state space, governed by Eq. (4.1), is necessarily Markovian and the action of the infinite dimensional operator on the infinitesimal state is an exact representation of the dynamics. However, discretizing inherently erases information through clumping states together into a discrete state, and therefore the dynamics on the discretized state space is necessarily not Markovian. Nonetheless, a Markov model can approximate the slow dynamics arbitrarily well, provided that the discretization can be made arbitrarily fine and the transition time scale τ sufficiently long [19]. In addition, the eigenspectrum of the transfer operator provides only a lower bound to the eigenvalues of the infinite dimensional operator [19, 20]. With this in mind, in the remainder of this chapter we will essentially focus only on the longest lived eigenfunctions of a finite approximation of the Perron-Frobenius operator in order to extract coarse-grained emergent properties of the dynamics.

4.3. IDENTIFYING METASTABLE STATES

Metastable states are obtained by combining microstates such that,

$$\frac{\mu(M \cap S_\tau(M))}{\mu(M)} \approx 1. \tag{4.11}$$

Therefore, the macrostates M are composed of microstates that remain nearly unaffected by the flow. As noted by Froyland [10], the condition for almost invariance, Eq. (4.11), is unchanged under time reversal. This allows us to use theoretical properties of reversible Markov chains to find the optimal partition of the state space into metastable sets. We enforce detailed balance by first building the time-reversed operator,

$$P^-_{ij} = \frac{\pi_j P_{ji}}{\pi_i}, \tag{4.12}$$

where π_i is our estimate of the invariant measure in the partition A_i, obtained through the left eigenvector of P, Eq. (4.10). We then define the reversibilized Markov operator R as

$$R(\tau, N) = \frac{P + P^-}{2}, \tag{4.13}$$

where we have omitted τ and N in P and P^-. The reversibilized Markov operator is then diagonalized, $R\phi = \lambda\phi$, and we identify metastable states by clustering the first non-trivial eigenfunction of the reversibilized Markov operator ϕ_2 through fuzzy c-means clustering [10, 21] (see Methods).

As previously discussed, discretizing the state space inherently results in the loss of information about the finer scale properties of the dynamics and therefore the discrete state space is not Markovian. Nonetheless, we can approximate the longest lived eigenfunctions arbitrarily well by making the discretization scale as small as possible, and estimating the transition time needed for $R(\tau, N)$ to be approximately Markovian [19]. This is done by using the Chapman-Kolmogorov equality $[R(\tau)]^n = R(n\tau) \implies [\lambda_i(\tau_0)]^n = \lambda_i(n\tau_0)$, which results in implied time scales, Eq. (4.2), that are constant in $\tau = n\tau_0$. We use this notion as a guide to choose τ, long enough such that the reversibilized Markov chain is nearly Markovian [19]. We will make use of a physically motivated example to illustrate some of the practical aspects of the transfer operator approximation.

4.3.1. OVERDAMPED BROWNIAN PARTICLE IN A DOUBLE-WELL POTENTIAL

In order to highlight some of the practical aspects of the transfer operator approximation and connect it with known descriptions of physical systems, we will study the dynamics of an overdamped particle in a symmetric double-well potential, Fig. (4.2),

$$dx_t = -\partial_x V(x_t)\,dt + \sqrt{2\beta^{-1}}\,dW_t \tag{4.14}$$

where $V(x) = (x^2-1)^2$ and dW_t is a Wiener process. We simulate $T = 5\times10^5$s sampled at $dt = 10^{-3}\text{s}^{-1}$, with an effective inverse temperature of $\beta = 3.15k_B$, using an Euler-Maruyama integration scheme (see e.g. [22]).

We partition the state space into N Voronoi cells through k-means clustering, and estimate the transition matrix P_τ by counting the transitions between microstates $A_i(t)$ and $A_j(t+\tau)$ (see Methods). In this case, the dynamics should obey detailed balance by construction. Nonetheless, we build the reversibilized Markov chain to correct numerical errors, and choose τ such that the relaxation time scales asymptote, Fig. (4.2B). As we increase the number of partitions, the τ needed for an accurate Markovian approximation of the dynamics drops, reaching the sampling time of

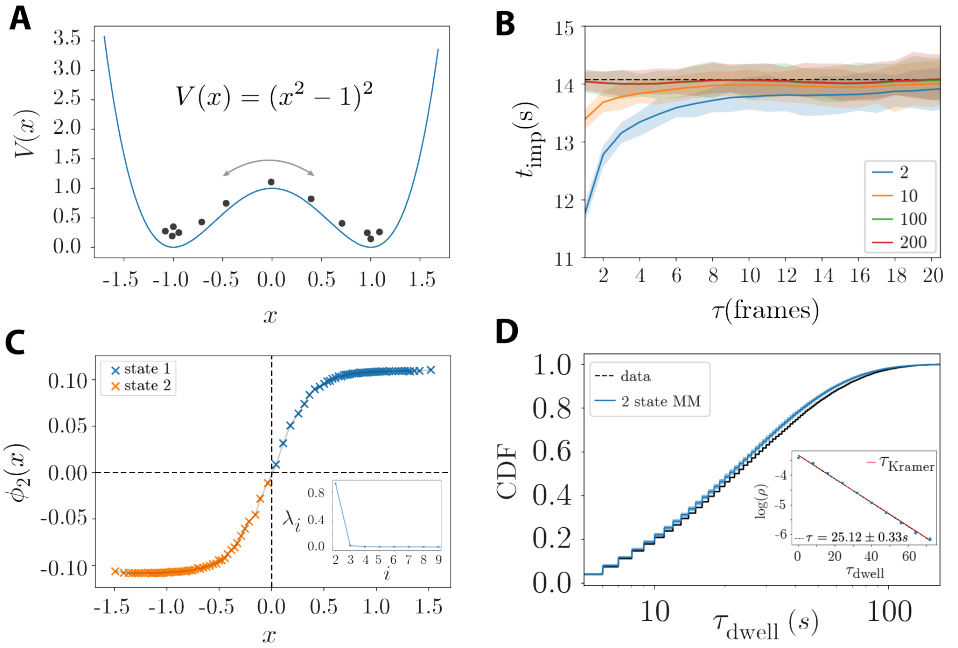

Figure 4.2: **Illustration of the transfer operator approximation in an overdamped Brownian particle in a double-well potential.** (A) - We simulate an overdamped particle in a symmetric double-well potential with $\sqrt{2\beta^{-1}} = 0.8$. (B) - Implied time scale of the longest lived eigenfunctions of the reversibilized transfer operator computed through a Galerkin projection onto N states using a k-means partitioning of the state space. Colors encode the number of states. The greater the number of states, the faster relaxation timescales converge to the asymptote, due to a better approximation of the boundary between metastable states. Confidence intervals were obtained through bootstrapping over 150 frame segments. Black dashed line represents the average time scale obtained with 100 partitions. (C) - Second eigenfunction of the reversibilized transfer operator computed using $N = 100$ partitions and $\tau = 1$ frame. Color encodes the partitioning of the eigenfunction through fuzzy c-means clustering (points are assigned the their most likely state). (C - inset) Firs eight non-trivial eigenvalues of the reversible transfer operator: there is a large gap between the second and third eigenvalues highlighting the large time scale separation in the system. (D) - Dwell times of the two metastable states computed from the data and from simulating the obtained 2 state Markov chain. (D - inset) - The distribution of dwell times closely matches the prediction from Kramer's rate theory. Errors in τ are computed through the standard deviation of the estimation done in 100 simulations. Shaded error bars represent 95% confidence intervals.

the simulations. This reflects our ability to better disentangle the boundary between the two metastable states of the system, which correspond to the potential wells. Using $N = 100$ partitions and $\tau = 1$ frame, we approximate the eigenvalues of the operator, Fig. (4.2C-inset). There is a clear timescale separation between the second and third eigenvalues, reflecting the existence of metastability along one eigenfunction. This eigenfunction offers a simple partition of the state space into its metastable states, which correspond to the potential wells, Fig. (4.2C). A two-state Markov model generated from the identified coarse-grained states captures the long time scale behavior of the system. The cumulative distribution of dwell times from simulations made from a 2 state Markov model closely matches the one from the data, Fig. (4.2D). In addition, we find that the decay time scale of the probability of remaining in the potential wells agrees with the prediction from Kramer's rate theory [23].

4.4. MARKOVIANITY AND PREDICTABILITY FOR STATE SPACE RECONSTRUCTION

In Chapter (3), we parameterized *C. elegans* postural time series through locally-linear models and used the statistics of the space of models to uncover structure in the short-time postural dynamics. Although powerful, this approach does not provide a natural way to study longer time scale dynamics: we are constrained to the short time scales in which the linear approximation holds. This is primarily due to the fact that the postural dynamics in inherently nonlinear in nature, but also because nothing guarantees that the postural time series evolve according to a first order differential equation. In fact, examples of second order dynamics are ubiquitous in biological systems: from single cell dynamics [24] to bird flocks and swarms [25, 26]. Even the dynamics of a simple harmonic oscillator exhibits second order dynamics in its position. In this example however, if we can measure the position and the momentum of the oscillator, we can then write down a system of first order differential equations that captures the dynamics of the system. Including this extra dynamical degree of freedom in the representation, and thus reconstructing the systems state space or phase space (we will these two terms interchangeably) [27, 28], not only simplifies the theory but also unleashes a higher degree of analytical power, as well as access to dynamical invariants and

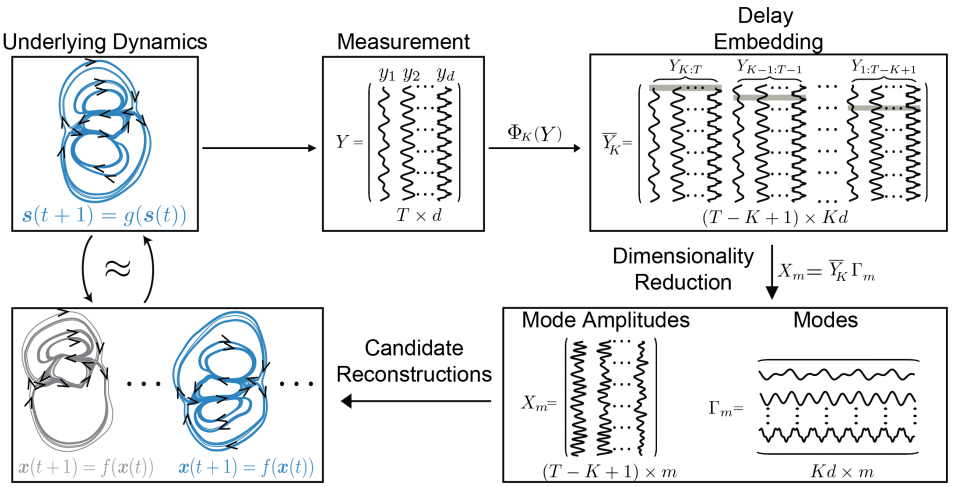

Figure 4.3: **State Space Reconstruction [1].** (From Upper Left) A d-dimensional time series of an underlying dynamical system is collected in the measurement matrix Y. The embedding operation Φ_K stacks delayed copies of the measurements within a short time window of length K into a matrix $\overline{Y}$ of size $(T-K+1)\times Kd$. Dimensionality reduction of $\overline{Y}$ results in an $m < Kd$ dimensional state space spanned by the basis vectors Γ_m called the modes. The mode coefficients X_m form an approximation of the state space of the underlying dynamics. Each value of K and m results in a different state space reconstruction of the underlying dynamics and we seek embedding parameters which maximize predictability and Markovianity for transfer operator approximation.

symmetries.

With a state space reconstruction, we seek a coordinate transformation Ψ that maps Y into a space X that is topologically equivalent [29] to the state space of the underlying dynamical system, a process known as time series embedding [30, 31]. Dynamical embeddings have been used to model complex phenomena such as ecological and neural dynamics [32, 33], and to characterize the stability and symmetry of their reconstructed attractors [34]. Although early approaches primarily used single-variable measurements, multivariate embeddings provide better reconstructions [35] and can improve prediction [36]. In [1], we have detailed a novel reconstruction method based on nearest-neighbor prediction and applied it to *C. elegans* postural dynamics, yielding interpretable state space modes and hints of deterministic chaos underlying the unpredictability of motion.

Here, we build upon those results and introduce new criteria for state space reconstruction. We first lift the D-dimensional measurements into a KD dimensional space of K contiguous delays and then project to a smaller m-dimensional subspace. Formally we decompose the embedding $\Psi = P_m \circ \Phi_K$ into a delay map Φ_K in which we iteratively stack $(K-1)$-delayed copies of Y into a $(T-K+1) \times KD$ matrix $\overline{Y}_K$, followed by a dimensionality reduction transformation P_m which projects $\overline{Y}_K$ onto an $m < KD$ dimensional space. P_m can in principle be any transformation and examples include numerical derivatives [37], delay coordinates [38] and random projections [33]. Here, we use singular value decomposition (SVD) [31, 35] followed by whitening transformation [39], which results in a state space with uncorrelated components spanning the dimensions of the first m singular vectors. In matrix notation $X_m = \overline{Y}_K \Gamma_m$, where Γ_m is the $KD \times m$ matrix of basis vectors spanning the m dimensional state space, while X_m contains the state space trajectories. This space of transformations allows for both derivative and more general linear filters [40] and the resulting coordinates reflect the most significant linear modes of the dynamics [31, 40].

The idea behind delay reconstruction is that as we stack delays into our definition of state, the state itself becomes memoryless and therefore more predictive. Picture the movement of a bead attached to a fixed spring. If we only have access to the position of the bead $x(t)$ at some time t, the prediction of the next state is ambiguous: the spring can be moving towards or away from its equilibrium state. This ambiguity regarding the future means that we need memory in order to make an accurate prediction: we not only need $x(t)$ but also $x(t-\tau)$, where τ is a time scale that is short enough such that we are not recurring back to the original state, but also long enough such that $x(t)$ and $x(t-\tau)$ are distinguishable. Therefore, the variable x itself is less predictable and less Markovian than the newly defined two-dimensional state composed of two time points $s = (x(t), x(t-\tau))$. Our criteria for state space reconstruction will therefore be the predictability and Markovianity of the candidate reconstructions, which we assess through estimating the entropy rate of a Markovian approximation of the dynamics. Given a finite partition $\{A_i\}_{i=1}^N$, we measure unpredictability through the entropy rate of the generated symbolic sequence assuming a first order Markov process from $A_i(t)$ to $A_j(t+dt)$, where dt is the sampling time of the data stream. Besides making the

calculation computationally tractable for large N[3], it provides a means to find the state space reconstruction and set of partitions that is most predictive and memoryless. For each candidate reconstruction, we compute the entropy rate through,

$$h(N) = \sum_{i,j=1}^{N} \pi_i P_{i,j}(dt, N) \log P_{i,j}(dt, N), \tag{4.15}$$

where π is the invariant distribution obtained from the first left eigenvector of $P(dt, N)$. Kolmogorov [41, 42] showed that Eq. (4.15) is bounded from above by the Kolmogorov-Sinai entropy h_{KS} in the limit of $dt \to 0$, which is the supremum over all possible partitions of the state space,

$$h_{KS} = \lim_{dt \to 0} \sup_{\{A_i\}_{i=1}^{N}} h(N). \tag{4.16}$$

The supremum is attained when a generating partition is used. When the phase space is partitioned along a generating partition, there is a one-to-one mapping between the state space trajectories and the symbolic dynamics encoded by the generating partition. However, finding a generating partition for general dynamical systems is extremely challenging, and only a few simple 1D and 2D discrete maps have been described in terms of their generating partitions [17]. Nonetheless, we will try to approach h_{KS} by sequentially refining our partition of phase space and optimizing the entropy rate.

Given a D-dimensional measurement time series $Y = \{y(t)\}$, $t \in \{0, dt, ..., T \times dt\}$ and a number of delays K, we stack delayed copies of Y generating a $K \times D$ dimensional trajectory matrix $\overline{Y}_K$. As we increase K, and thus include more dynamical information into the definition of state, the largest obtained entropy rate $h^*(K)$ decreases as the states have less memory and thus the system becomes more predictable. We choose K^* as the shortest time scale at which the estimates of the entropy stop decreasing. Once K^* is found, we do SVD on the obtained trajectory matrix $\overline{Y}_K$, and re-estimate the largest entropy rate as a function of dimension $h^*(m)$. We whiten the SVD modes before partitioning the space in order to ensure that different modes are given the same scale, making the space more amenable to the euclidean metric. If we project into a space

[3] Counting sequences of length l of an N letter alphabet quickly becomes intractable, since the number of allowed sequences grows with l^N

that is too low dimensional, the trajectories will self-cross and look more random than the true phase space trajectories, thus overestimating the entropy rate. We obtain a lower bound for m^* by looking at when the entropy rate as a function of m plateaus.

4.4.1. LORENZ SYSTEM

As an example application of using the transfer operator approximation to reconstruct the state space, we will study a low dimensional chaotic system given by the Lorenz equations, Fig. (4.4),

$$\begin{cases} \dot{x} = \sigma(y - x) \\ \dot{y} = x(\rho - z) - y \\ \dot{z} = xy - \beta z, \end{cases} \tag{4.17}$$

in the standard chaotic regime: $\sigma, \rho, \beta = (10, 28, 8/3)$. We simulate a long simulation of the Lorenz system, with $T = 10^4$s, sampled at $dt = 10^{-2}\text{s}^{-1}$ (see Methods). With increasing number of partitions N, the entropy rate, Eq. (4.15), grows and reaches a plateau at $\hat{h}_{KS} = 1.031(1.029, 1.032)$nat/s, with $N \sim 1000$ partitions, Fig. (4.4B). The relaxation times of the reversibilized transition matrix, Fig. (4.4B-inset), computed with $N = 2000$ partitions, converge after $\tau \sim 0.07$s, and we choose $\tau = 0.1$s to maximize the time scale separation between the first and second eigenfunctions. Using $N = 2000$ and $\tau = 0.1$s we approximate the reversibilized transfer operator and use its longest lived eigenfunction to split the state space into its almost invariant sets, Fig. (4.4C), through fuzzy c-means clustering (see Methods). The two almost-invariant sets split the state space along the stable manifold of the lowest period symmetric periodic orbit [43], plotted as a black line in Fig. (4.4C-right).

To illustrate the use of the Markovianity and predictability of the transfer operator approximation as state space reconstruction criteria, we take the x variable of the Lorenz system simulation and try to find the K and m that yield a maximally predictive and Markovian state space reconstruction. For each choice of K, we maximize the estimate of the entropy rate as a function of N. As we increase the number of delays K, the estimates of the maximum entropy drop with a large negative slope, before reaching a broad plateau, Fig. (4.5A - left). On close inspection, we see that the entropy rate estimates slowly grows after a local minimum at $K^* = 12$ frames. Given this choice of K, we then perform SVD and whitening,

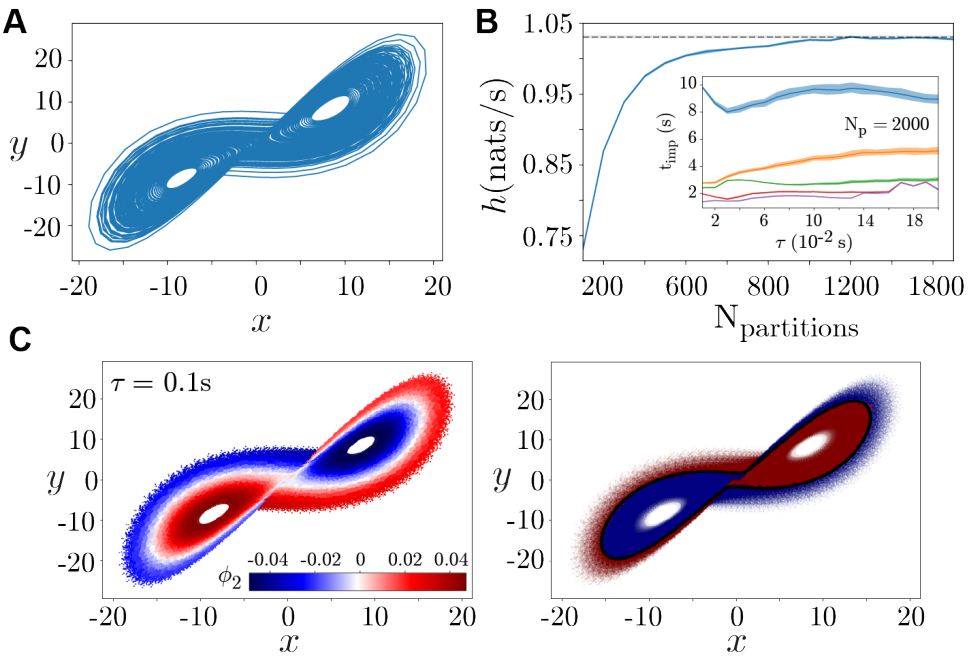

Figure 4.4: **Transfer operator approximation and almost invariant sets of the Lorenz system.** (A) - Sample trajectory of the Lorenz system in the standard chaotic regime. (B) - Entropy rate h as a function of the number of partitions. The entropy estimates stabilize after about 1000 partitions. Error bars are 95% boostrapped confidence intervals obtained by placing different partitions in the state space through the k-means++ initialization (see Methods). (B - inset) - Implied time scales of the first five eigenfunctions of the reversible transfer operator built with 2000 partitions stabilize with $\tau \approx 0.1\,s$. Error bars are 95% confidence intervals obtained by bootstrapping over 500 frame segments. Colors represent the implied time scales from different eigenfunctions (organized according to the time scale). (C - left) - Second eigenfunction of the reversible transfer operator computed with $\tau = 0.1s$. (C - right) - Almost invariant sets obtained through clustering the second eigenfunction. The lowest period symmetric periodic orbit (black line), and its stable manifold, establish part of the boundary between the almost invariant sets [43].

and estimate the maximum entropy rate as a function of dimension, m, Fig. (4.5A - right). The most predictable state space is found with $m^* = 3$ dimensions, yielding $\hat{h}_{KS} = 1.008(1.007, 1.009)$nat/s. A sample trajectory of the reconstructed attractor is shown in Fig. (4.5B). In Fig. (4.5C) we show the estimated relaxation time scales of the reversibilized transfer operator built from $N = 2000$ partitions of the reconstructed state space, which is remarkably similar to the one obtained using the simulations directly, Fig. (4.4B-inset). With $\tau = 0.1s$ we estimate the longest lived non-trivial eigenfunction of the reversibilized transfer operator and split the state space into almost invariant sets through fuzzy c-means clustering. Analogous to what we have found using the complete state space, the fastest symmetric unstable periodic orbits establishes part of the boundary between the almost invariant sets [43]. In this way, we have shown how we can take incomplete measurements of an underlying dynamical system, reconstruct the state space, and build an approximation of the transfer operator on densities that recovers the coarse-grained emergent properties of the dynamics.

4.4.2. OVERDAMPED PARTICLE IN A DOUBLE-WELL POTENTIAL COUPLED TO FAST LORENZ SYSTEM

In this section, we will make the time scale separation explicit in the equations of motion, and extract an effective coarse-grained statistical description of a purely deterministic system. We will essentially couple a particle in a double-well potential, with the y variable of a fast Lorenz system:

$$\begin{cases} \dot{x_1} = x_1 - x_1^3 + \frac{0.05}{\epsilon} y \\ \dot{x} = \frac{1}{\epsilon^2}\left[\sigma(y - x)\right] \\ \dot{y} = \frac{1}{\epsilon^2}\left[x(\rho - z) - y\right] \\ \dot{z} = \frac{1}{\epsilon^2}\left(xy - \beta z\right), \end{cases} \tag{4.18}$$

where the vector (x, y, z) solves the Lorenz equations, Eq. (4.17), in the standard chaotic regime and the scalar x_1 is driven by a fast chaotic signal with a characteristic time ϵ^2. We will use this toy example as an illustration of how we can extract slow coarse-grained properties of a dynamical system, even when we do not directly observe the full underlying state space. We will take the x_1 variable only, reconstruct the state space in the same way as we have done in the previous section, and then build a discretiza-

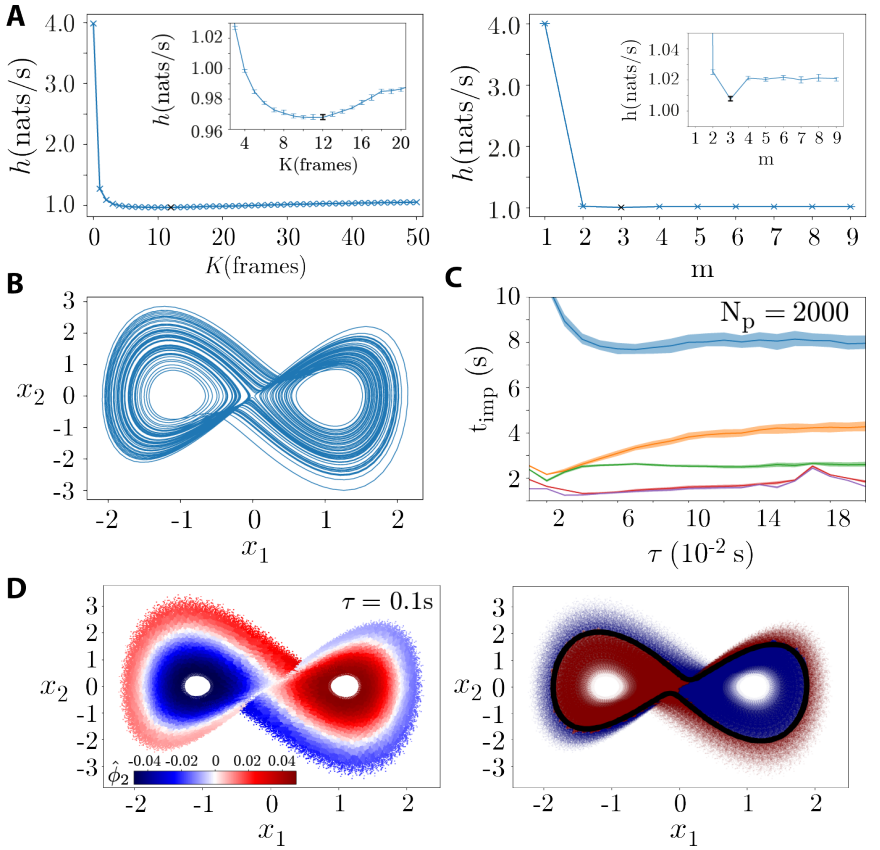

Figure 4.5: **Reconstructing the state space and almost invariant sets of the Lorenz system from incomplete measurements.** We take the x variable of the Lorenz system, and use to reconstruct the state space using delays. (A) - Entropy rate as a function of the embedding parameters. (A - left) Entropy rate as a function of K. We choose $K^* = 12$ frames. (A - right) Entropy rate as a function of dimension m. We choose $m^* = 3$. Error bars are 95% boostrapped confidence intervals obtained by placing different partitions in the state space through the k-means++ initialization (see Methods). (B) - Sample trajectory of the reconstructed state space variables along the first two modes x_1 and x_2. (C) - Implied time scales of the first five eigenfunctions of the reversible transfer operator built with 2000 partitions stabilizes at $\tau \approx 0.1\,s$. Note the remarkable resemblance with Fig. (4.4B-inset). Shaded error bars represent 95% confidence intervals bootstrapped over 500 frame segments. Colors represent the implied time scales from different eigenfunctions (organized according to the time scale). (D - left) - Second eigenfunction of the reversible transfer operator built from the reconstructed state space (computed with $\tau = 0.1s$). (D - right) - Almost invariant sets obtained by clustering the second eigenfunction of the reversible transfer operator built in the reconstructed state space. The lowest period symmetric periodic orbit (black line), and its stable manifold, establish part of the boundary between the almost invariant sets [43].

tion of state space that yields an effective phenomenological description of the dynamics at large scales.

In order to be able to observe the time scale separation, we generated a collection of 100 simulations sampled at 5000Hz for 10s, with $\epsilon = 0.1$ (see Methods). In Fig. (4.6A), we show the distribution of x_1, which resembles the invariant density of the double well potential. In fact, we can fit the distribution of x_1 to a Boltzmann distribution of the form $P(x_1) = e^{-\beta V(x_1)}$, where $V(x_1) = (x_1^2 - 1)^2$, and find an effective temperature of $\beta = 2.803 \pm 0.003$ in units of $k_B = 1$ (dashed lines in Fig. (4.6A)). Using this inferred temperature, we can simulate an overdamped Brownian particle under such a potential at this temperature, and find that the long term behavior of the system is remarkably similar to the x_1 variable of Eq. (4.18). Therefore, forcing through a fast chaotic system or a stochastic process is indistinguishable at long time scales.

Can we extract the coarse-grained metastable states of this system with incomplete measurements? We will now take the x_1 variable only, reconstruct the state space by stacking K delays, and extract the long lived eigenfunctions and metastable state through the approximation of the transfer operator on densities. We start by stacking K delays of x_1 into a $\overline{Y}_K$ trajectory matrix, and find the maximum entropy rate for each choice of K, Fig. (4.6B-left). The entropy quickly drops until it reaches a short plateau, after which we start losing information as the entropy drops linearly with a slope ~ 0 (see Discussion). As a guide, we plot the change in entropy rate as a function of K and choose $K^* = 13$ frames when the slope of h stops changing, Fig. (4.6B-left,inset). Given this choice of K^*, we then follow to find the number of dimensions needed to capture the predictability, which is $m^* = 4$, Fig. (4.6B-right), consistent with Eq. (4.18). The implied time scales of the reversibilized transfer operator, with $N = 2000$ partitions, indicate that there is one prominent eigenfunction, with a relaxation time that is about two orders of magnitude longer than the next, Fig. (4.6C). In this way, the spectrum of the approximated transfer operator remarkably captures the time scale separation we have put into the system through $\epsilon^2 = 10^{-2}$ in Eq. (4.18). We choose $\tau = 200$ frames as our transition time scale. We then diagonalize the reversibilized transition matrix and cluster the first non-trivial eigenfunction, Fig. (4.6D). We color-code the projection of the first non-trivial eigenfunction along the first state space variable, s_1, by the fuzzy c-means probability of belong-

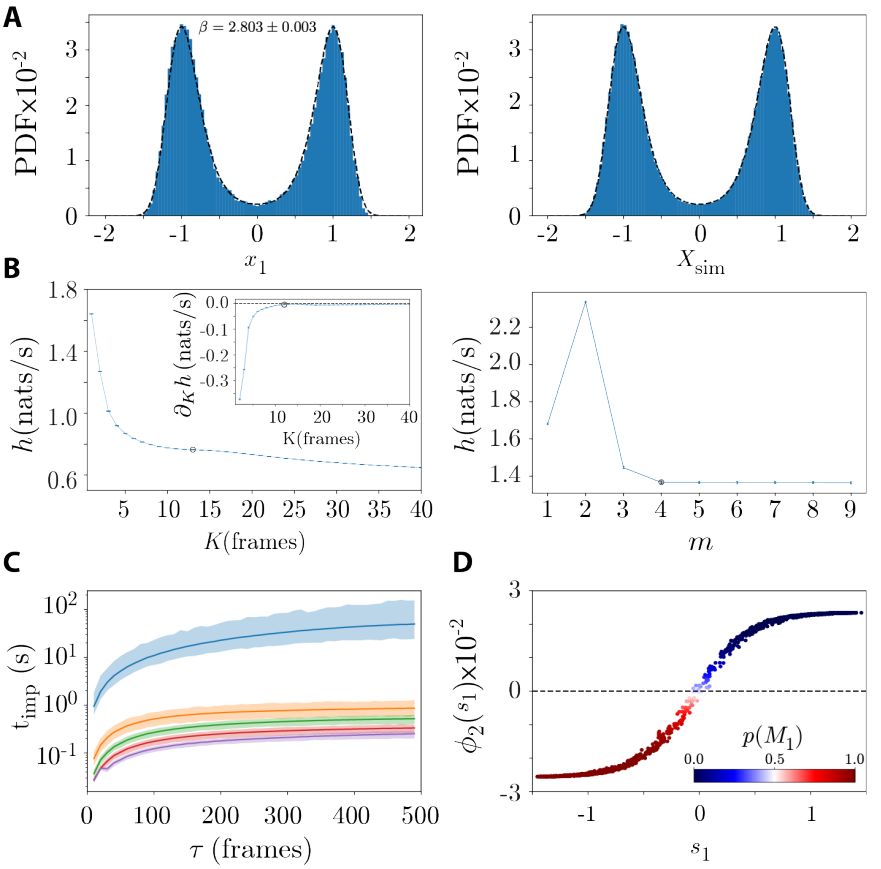

Figure 4.6: **Subsuming a fast chaotic system into an effective statistical description allows for the extraction of long lived properties of the dynamics.** (A-left) - We fit the distribution of x_1 to a Boltzmann distribution with $V(x_1) = (x_1^2 - 1)^2$, yielding $\beta = 2.083 \pm 0.003$. (A-right) - Using the inferred effective temperature, we simulate an overdamped particle in a double-well potential (using an Euler-Maruyama scheme) and essentially recover the long time behavior of x_1. (B) - Entropy rate as function of K and m. We choose $K^* = 13$ frames and $m^* = 4$. Error bars are 95% boostrapped confidence intervals obtained by placing different partitions in the state space through the k-means++ initialization (see Methods). (C) - Implied time scales of the first five eigenfunctions of the reversibilized transfer operator. One eigenfunction emerges as the longest lived, with a relaxation time about two orders of magnitude longer than the next eigenfunction, in accordance with the characteristic time $\epsilon^2 = 10^{-2}$ in Eq. (4.18). Confidence intervals are obtained by bootstrapping over 5000 frame segments. Colors represent the implied time scales from different eigenfunctions (organized according to the time scale). (D) - First non-trivial eigenfunction of the reversibilized transfer operator plotted as a function of the first state space variable s_1. Color encodes the fuzzy c-means probability of belonging to one of the metastable states, indicating that the eigenfunction separates the two wells of the double-well potential.

ing to one of the metastable states. The obtained metastable states correspond to the potential wells, and the eigenfunction is remarkably similar to the one obtained in Fig. (4.2C) for an overdamped Brownian particle in a double well potential.

4.5. DISCUSSION

In this chapter, we have introduced the concepts of state space reconstruction and transfer operator approximation with the goal of bridging time scales in complex high dimensional dynamical systems. The Markov approximation of the dynamics on the discretized state space offers a powerful tool for extracting coarse-grained emergent properties, and is robust to the origins of the underlying unpredictability of the system. In the last example, we started with short incomplete observations of a scalar variable coupled to an unseen fast chaotic system. From these short simulations, we were able to find the amount of delays K and dimensions m needed to reconstruct the underlying state space. Using the reconstructed state space and the short trajectories, we estimated the transfer operator on densities and learned that the system exhibits a strong time scale separation, consistent with the characteristic time scale that we have built into the simulations of Eq. (4.18). Finally, we found that the second eigenfunction of the reversibilized transfer operator essentially splits the state space among the two wells of the potential.

In systems with a clear time scale separation, like the first example, the dynamics is accurately approximated by a simple two state Markov model built from the identified metastable states. However, for systems with a continuum of time scales, the discrete Markov chain only provides an accurate approximation of the longest lived eigenfunctions (provided that we have a fine enough discretization and that we choose the transition time scale τ long enough). This means that we are necessarily losing information about the finer scale dynamics, and therefore our Markov approximation is not a complete model of the underlying dynamical system. Nonetheless, the finite Markov approximation of the dynamics allows us to identify the most important emergent properties of the system on longer time scales, which will be our main goal when applying these techniques to data.

We devised an heuristic method for choosing K^* in systems for which the entropy rate does not have a clear minimum/plateau. Our reasoning

is that we want the choice of K to provide a first order time scale separation, such that the dynamics then evolve as a smooth non-intersecting trajectory in state space. The remaining time scales are hopefully captured in the transfer operator approximation. In systems for which there are multiple time scales, like the last example, the slow drift in the entropy rate could be due to the fact that we slowly start adding information about longer time scale processes into the definition of state, which lowers the entropy rate as we cannot observe important faster time scale transitions. Further research will be needed to gain a deeper theoretical understanding of the behavior of the entropy rate estimates as a function of K for multiscale systems.

In the next chapter, we will make use of this formalism to extract long time scale behaviors from *C. elegans* posture dynamics. We will treat the fine scale posture time series as incomplete measurements of an underlying dynamical system and reconstruct its state space through maximizing predictability and Markovianity. The eigenfunctions of the transfer operator provide means to learn effect emergent properties of the dynamics, and therefore bridge the gap between fine scale postural dynamics (Chapter 3) and coarse-grained phenomenological descriptions of longer time scale behaviors (Chapter 2).

4.6. METHODS

STATE SPACE RECONSTRUCTION

Given a D-dimensional time-series in $Y = [\mathbf{y}_1^{1:T}, \cdots, \mathbf{y}_D^{1:T}]$, along with an estimate of the optimal embedding window K^*, and minimum embedding dimension m^*, the state space reconstruction proceeds as follows. First, we create the $L \times K^* D$ matrix $\overline{Y}_{K^*}$ containing delayed copies of the measurements, $\overline{Y}_{K^*} = [\mathbf{y}_{1:D}^{1:L}, \mathbf{y}_{1:D}^{2:(L+1)}, \cdots, \mathbf{y}_{1:D}^{K:T}]$, where $L = (T - K^* + 1)$. We then perform singular value decomposition and keep the first m^* left-singular vectors, which we whiten [39] to obtain uncorrelated rescaled modes. When estimating K^* and m^*, we use the following procedure. For a given choice of K, we build a trajectory matrix $\overline{Y}_K$, and then estimate the entropy rate of $\overline{Y}_K$ by partitioning the state space into N Voronoi cells through k-means clustering, and maximizing the entropy as a function of the number of partitions. We initialize the k-means algorithm with a k-means++ initialization 50 times, which randomizes the position of the

partition seeds. We use the variability coming from the inherent stochasticity of the partitioning process to obtain bootstrapped error bars. The same procedure is applied to the estimates of the entropy as a function of m, except that now we partition the state space given by the first m whitened singular vectors of $\overline{Y}_{K^*}$.

STATE SPACE PARTITIONING

We partition the state space into N Voronoi cells through k-means clustering with a k-means++ initialization using scikit-learn [44]. We initialize the algorithm $n = 50$ times, to yield different partitions of the state space.

ESTIMATION OF TRANSITION MATRICES

Given T observations, a set of N partitions, and a transition time τ, we count how many times we jump from the partition A_i at time t to the partition A_j at time $t+\tau$ as,

$$C_{ij}(\tau) = \sum_{t=0}^{T-\tau} \zeta_i(x(t))\zeta_j(x(t+\tau)), \tag{4.19}$$

where $\zeta_i(x)$ are the Ulam basis functions defined in Eq. (4.9). The maximum likelihood estimator of the transition matrix is obtained by simply row normalizing the count matrix,

$$P_{ij} = \frac{C_{ij}}{\sum_j C_{ij}}. \tag{4.20}$$

SPECTRUM OF THE TRANSFER OPERATOR AND IDENTIFICATION OF COHERENT SETS

We diagonalize the reversibilized Markov operator $R(\tau, N)$, Eq. (4.3), using ARPACK [45] constrained on finding the k eigenvalues with largest real part. We note that the estimated eigenvalues only provide a lower bound for the eigenvalues of the infinite dimensional operator [20]. The first non-trivial eigenfunction is clustered using fuzzy c-means clustering [21], using the scikit-fuzzy package [46] in Python [47]. The transition time scale is chosen long enough such that the implied time scales, Eq.(4.2), reaches an asymptote. In addition to the Markovinity condition, when constructing coherent sets we also try to maximize the time scale

gap between the first and second implied time scales. In order to get error bars in the implied time scales, we bootstrap over uncorrelated trajectories obtained by splitting the trajectory into shorter segments that are long enough such that the implied time scales converge clearly.

SIMULATIONS

Overdamped Brownian particle in a double well potential: We use an Euler-Maruyama integration scheme to generate a $T = 5 \times 10^5$s long trajectory sampled at $dt = 10^{-3}\text{s}^{-1}$ using Eq. (4.3.1) with $\sqrt{2\beta^{-1}} = 0.8$.

Lorenz system: We use scipy's odeint package [48] to generate a $T = 2 \times 10^4$s long trajectory of the Lorenz system in the standard chaotic regime $(\sigma, \rho, \beta) = (10, 28, 8/3)$, sampled at $dt = 10^{-2}\text{s}^{-1}$. We discard the first 10^4s to avoid transients, yielding a T = 10^4s long simulation.

Double-well coupled to Lorenz system: In order to have enough samples of the system both at small and large time scales, we sample the system at 5000s^{-1}. We generate 100 10s long simulations with varying initial conditions. The initial conditions for x_1 were chosen uniformly on the interval $[-2, 2[$, while x, y, z were sampled from a long simulation of the Lorenz system at the standard chaotic regime, sampled at 100s^{-1}, that had converged onto the attractor (to avoid sampling transients). Both simulations were done using scipy's odeint function [48].

ACKNOWLEDGEMENTS

We thank SURFsara (www.surfsara.nl) for computing resources through the Lisa system. This work was supported by the research program of the Foundation for Fundamental Research on Matter (FOM), which is part of the Netherlands Organization for Scientific Research (NWO), and also by funding from The Okinawa Institute of Science and Technology Graduate University. We also thank David Jordan and Tosif Ahamed for useful discussions.

REFERENCES

[1] T. Ahamed, A. C. Costa, and G. J. Stephens, *Capturing the Continuous Complexity of Behavior in C. elegans,* (2019), arXiv:1911.10559 [q-bio.NC] .

[2] A. Lasota and M. Mackey, *Chaos, Fractals, and Noise: Stochastic Aspects of Dynamics*, 2nd ed., Vol. 97 (Springer-Verlag New York, 1994).

[3] F. Noé and C. Clementi, *Kinetic Distance and Kinetic Maps from Molecular Dynamics Simulation,* Journal of Chemical Theory and Computation **11**, 5002 (2015), arXiv:1506.06259 .

[4] C. Schütte and W. Huisinga, *Biomolecular conformations can be identified as metastable sets of molecular dynamics,* Handbook of Numerical Analysis **10**, 699 (2003).

[5] F. Noé, I. Horenko, C. Schütte, and J. C. Smith, *Hierarchical analysis of conformational dynamics in biomolecules: Transition networks of metastable states,* Journal of Chemical Physics **126** (2007), 10.1063/1.2714539.

[6] K. Fackeldey, P. Koltai, P. Névir, H. Rust, A. Schild, and M. Weber, *From metastable to coherent sets - Time-discretization schemes,* Chaos **29** (2019), 10.1063/1.5058128.

[7] P. Koltai, H. Wu, F. Noé, and C. Schütte, *Optimal data-driven estimation of generalized markov state models for non-equilibrium dynamics,* Computation **6**, 1 (2018).

[8] P. Deuflhard and M. Weber, *Robust Perron cluster analysis in conformation dynamics,* Linear Algebra and Its Applications **398**, 161 (2005).

[9] G. Froyland, S. Lloyd, and N. Santitissadeekorn, *Coherent sets for nonautonomous dynamical systems,* Physica D: Nonlinear Phenomena **239**, 1527 (2010).

[10] G. Froyland, *Statistically optimal almost-invariant sets,* Physica D: Nonlinear Phenomena **200**, 205 (2005).

[11] G. Froyland, G. A. Gottwald, and A. Hammerlindl, *A Computational Method to Extract Macroscopic Variables and Their Dynamics in Multiscale Systems,* SIAM Journal on Applied Dynamical Systems **13**, 1816 (2014).

[12] S. Klus, B. E. Husic, and M. Mollenhauer, *Kernel canonical correlation analysis approximates operators for the detection of coherent structures in dynamical data,* (2019), arXiv:1904.07752 .

[13] J. D. Chodera and F. Noé, *Markov state models of biomolecular conformational dynamics,* Current Opinion in Structural Biology **25**, 135 (2014).

[14] H. Wu, F. Nüske, F. Paul, S. Klus, P. Koltai, and F. Noé, *Variational Koopman models: Slow collective variables and molecular kinetics from short off-equilibrium simulations,* Journal of Chemical Physics **146** (2017), 10.1063/1.4979344.

[15] F. Noé, H. Wu, J. H. Prinz, and N. Plattner, *Projected and hidden Markov models for calculating kinetics and metastable states of complex molecules,* Journal of Chemical Physics **139** (2013), 10.1063/1.4828816.

[16] E. M. Bollt, A. Luttman, S. Kramer, and R. Basnayake, *Measurable Dynamics Analysis of Transport in the Gulf of Mexico During the Oil Spill,* International Journal of Bifurcation and Chaos **346** (2011), 10.1142/s0218127412300121.

[17] E. M. Bollt and N. Santitissadeekorn, *Applied and computational measurable dynamics* (Society for Industrial and Applied Mathematics, Philadelphia, United States, 2013).

[18] S. Klus, F. Nüske, P. Koltai, H. Wu, I. Kevrekidis, C. Schütte, and F. Noé, *Data-Driven Model Reduction and Transfer Operator Approximation,* Journal of Nonlinear Science **28**, 985 (2018), arXiv:1703.10112 .

[19] J.-h. Prinz, H. Wu, M. Sarich, B. Keller, M. Senne, M. Held, J. D. Chodera, C. Schütte, F. Noé, J.-h. Prinz, H. Wu, M. Sarich, B. Keller, M. Senne, M. Held, J. D. Chodera, C. Schütte, and F. Noé, *Markov models of molecular kinetics : Generation and validation Markov*

models of molecular kinetics : Generation and validation, The Journal of Chemical Physics **134** (2011), 10.1063/1.3565032.

[20] N. Djurdjevac, M. Sarich, and C. Schütte, *Estimating the eigenvalue error of Markov State Models,* SIAM Multicale Model. Simul. **10**, 61 (2012).

[21] J. C. Bezdek, R. J. Hathaway, M. J. Sabin, and W. T. Tucker, *Convergence theory for fuzzy c-means: counterexamples and repairs,* IEEE Transactions on systems, man, and cybernetics **SMC-17**, 873 (1987).

[22] K. Burrage, P. Burrage, and T. Mitsui, *Numerical solutions of stochastic differential equations — implementation and stability issues,* J. Comput. Appl. Math. **125**, 171–182 (2000).

[23] H. A. Kramers, *Brownian motion in a field of force and the diffusion model of chemical reactions,* Physica **7**, 284 (1940).

[24] D. B. Brückner, A. Fink, C. Schreiber, P. J. F. Röttgermann, J. O. Rädler, and C. P. Broedersz, *Stochastic nonlinear dynamics of confined cell migration in two-state systems,* Nature Physics **15**, 595 (2019).

[25] A. Attanasi, A. Cavagna, L. Del Castello, I. Giardina, T. S. Grigera, A. Jelić, S. Melillo, L. Parisi, O. Pohl, E. Shen, and M. Viale, *Information transfer and behavioural inertia in starling flocks,* Nature Physics **10**, 691 (2014).

[26] A. Cavagna, D. Conti, C. Creato, L. Del Castello, I. Giardina, T. Grigera, S. Melillo, L. Parisi, and M. Viale, *Dynamic scaling in natural swarms,* Nature Physics **13**, 914 (2017).

[27] S. H. Strogatz, *Nonlinear Dynamics and Chaos with Student Solutions Manual: With Applications to Physics, Biology, Chemistry, and Engineering* (Westview Press, a member of the Perseus Books Group, Boulder, Colorado, USA, 2015).

[28] D. D. Nolte, *The tangled tale of phase space,* Physics Today **63**, 33 (2010).

[29] J. Palis and W. de Melo, *Geometric Theory of Dynamical Systems* (Springer US, 1982).

[30] M. Casdagli, S. Eubank, J. D. Farmer, and J. Gibson, *The theory of state space reconstruction in the presence of noise,* Physica D **51**, 52 (1991).

[31] D. S. Broomhead and G. P. King, *Extracting qualitative dynamics from experimental data,* Physica D: Nonlinear Phenomena **20**, 217 (1986).

[32] G. Sugihara and R. M. May, *Nonlinear forecasting as a way of distinguishing chaos from measurement error in time series,* Nature **344**, 734 (1990).

[33] S. Tajima, T. Yanagawa, N. Fujii, and T. Toyoizumi, *Untangling Brain-Wide Dynamics in Consciousness by Cross-Embedding,* PLOS Comput. Biol. **11**, 1 (2015).

[34] H. Kantz and T. Schreiber, *Nonlinear time series analysis*, Vol. 7 (Cambridge university press, 2004).

[35] P. Read, *Phase portrait reconstruction using multivariate singular systems analysis,* Physica D: Nonlinear Phenomena **69**, 353 (1993).

[36] H. Ye and G. Sugihara, *Information leverage in interconnected ecosystems: Overcoming the curse of dimensionality,* Science **353**, 922 (2016).

[37] N. H. Packard, J. P. Crutchfield, J. D. Farmer, and R. S. Shaw, *Geomery from a Time Series,* Physical Review Letters **45**, 712 (1980).

[38] F. Takens, *Detecting strange attractors in turbulence,* in *Dynamical Systems and Turbulence, Warwick 1980*, edited by D. Rand and L.-S. Young (Springer Berlin Heidelberg, Berlin, Heidelberg, 1981) pp. 366–381.

[39] J. H. Friedman, *Exploratory projection pursuit,* Journal of the American Statistical Association **82**, 249 (1987).

[40] J. F. Gibson, J. Doyne Farmer, M. Casdagli, and S. Eubank, *An analytic approach to practical state space reconstruction,* Physica. D, Nonlinear phenomena **57**, 1 (1992).

[41] A. Kolmogorov, *A new metric invariant of transient dynamical systems and automorphisms in Lebesgue spaces.* Dokl. Akad. Nauk SSSR **119**, 861 (1958).

[42] A. N. Kolmogorov, *On the entropy per unit time as a metric invariant of automorphisms,* Doklady of Russian Academy of Sciences **124**, 754 (1959).

[43] G. Froyland and K. Padberg, *Almost-invariant sets and invariant manifolds - Connecting probabilistic and geometric descriptions of coherent structures in flows,* Physica D: Nonlinear Phenomena **238**, 1507 (2009).

[44] F. Pedregosa, G. Varoquaux, A. Gramfort, V. Michel, B. Thirion, O. Grisel, M. Blondel, P. Prettenhofer, R. Weiss, V. Dubourg, J. Vanderplas, A. Passos, D. Cournapeau, M. Brucher, M. Perrot, and E. Duchesnay, *Scikit-learn: Machine learning in Python,* Journal of Machine Learning Research **12**, 2825 (2011).

[45] R. B. Lehoucq, D. C. Sorensen, and C. Yang, *ARPACK Users' Guide* (Society for Industrial and Applied Mathematics, 1998) https://epubs.siam.org/doi/pdf/10.1137/1.9780898719628 .

[46] *Scikit-fuzzy version 0.4.2,* .

[47] G. Rossum, *Python Reference Manual*, Tech. Rep. (Amsterdam, The Netherlands, The Netherlands, 1995).

[48] E. Jones, T. Oliphant, P. Peterson, and et al., *SciPy: Open source scientific tools for Python,* (2001–).

5

BRIDGING TIME SCALES IN *C. elegans* BEHAVIOR: FROM POSTURAL DYNAMICS TO MOTILITY STRATEGIES

5.1. INTRODUCTION

Animal behavior exhibits multiple time scales. From fine scale movements dictated by the coordinate activity of motor neurons, to larger scale sequences of behaviors controlled by higher order structures in the nervous system, to the modulation of said structures by the action of neuromodulators and external stimuli. A fine scale characterization of behavior such as the one employed in Chapter 3 fails to capture the longer time scale modulation of behavior and behavioral sequences, whereas a coarse-grained phenomenological description of the dynamics, such as the one in Chapter 2, fails to identify the fine scale postural dynamics underlying the behavioral variability.

Understanding the neural and genetic mechanisms underlying the control of behavior over multiple time scales requires dynamical representations that allow us to probe the details of the dynamics on longer time scales, without giving up on a fine scale postural description of the movement. Working at the level of the body posture allows us to study fine

This chapter builds upon results presented in [1], and we reference to this work often.

scale neuromuscular control mechanisms and most dynamical representations based on postures focus on short time scale behavior [2–6]. Although powerful, these approaches do not offer a principled means for bridging time scales, and are often tied to a specific time scale [7]. In fact, such representations often yield non-Markovian dynamics [6, 8], highlighting their failure to capture longer time scale changes in behavior. One of the main challenges in unifying time scales is the fact that higher level control mechanisms and hidden internal states impact the fine scale behavioral dynamics [9–11]. Hunger and reproductive state, for example, are main drivers of changes in behavior, and therefore impact the likelihood of different fine scale behaviors or behavioral sequences [12–17]. Therefore, we need a dynamical representation that allows us to accurately represent the fine scale dynamics, but also be able to abstract from the fine scale variability and extract coarse-grained emergent properties of the dynamics on longer time scales.

In our recent work [1], we have reconstructed the state space of *C. elegans* postural dynamics and used it to identify interpretable state space modes and hints of deterministic chaos underlying the unpredictability of motion. Here, we propose that the formalism of state space reconstruction and transfer operator approximation offers a principled means to abstract from the chaotic dynamics at finer scales and learn effective hydrodynamic theories of behavior on longer time scales. The transfer operator on phase space densities offers not only a model of the dynamics, but also enables the decomposition of behavior into long lived modes. This allows us to build a multiscale picture of the dynamics, from millisecond postural movements up to minutes long changes in the way worms explore their environment. We find evidence of neuromodulatory mechanisms that impact the longer time scale behavior, as well as fine scale changes in short time scale behaviors underlying the behavior on different conditions. Our results represent a significant advance in our ability to extract hidden long time scale processes from postural dynamics alone, and open the path for a deeper understanding of the underlying neural and genetic machinery controlling behavior on multiple interacting time scales.

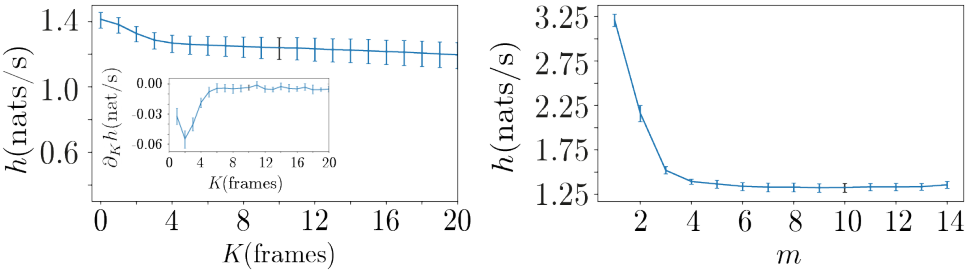

Figure 5.1: **Predictability for state space reconstruction of the posture dynamics: N2 worms off food.** We use the entropy of a first-order Markov approximation of the dynamics on a partitioned state space to assess the predictability and Markovianity of different candidate reconstructions. (left) - Maximum entropy rate h as a function of K, averaged over 12 worms. With increasing K the entropy rate quickly drops reaching a broad plateau. We choose $K^* = 10$ frames. (right) - Maximum entropy rate h as a function of the number of the state space dimension, m. With increasing m, the entropy rate drops and reaches a plateau at ~ 6 dimensions. We choose $m^* = 10$. Error bars are 95% confidence intervals bootstrapped across worms.

5.2. FORAGING WILD-TYPE WORMS: COHERENT SETS AND BEHAVIOR

In 2D, worms move by making dorsoventral sinusoidal bends along their body [18], which can be captured through high resolution tracking microscopy to give a multidimensional time-series of posture changes [19]. Despite the variety of visible postures, most of the shape variation is captured by a linear combination of a small number of primitive shape dimensions (eigenworms) [20, 21], as we have seen in Chapter 3. Projections along the eigenworm dimensions describe the worm's instantaneous shape and are not a direct indication of behavior, which arises from posture changes. For example, Schwarz et al. [2] found evidence that the posture space alone is not enough to provide an accurate Markovian approximation of the dynamics: sequences of three states were required to reproduce higher order sequence statistics. As introduced in the previous chapter, our approach explicitly includes dynamical information into the definition of state through state space reconstruction, while trying to maximize the predictability and Markovianity of the transfer operator approximation.

5.2.1. STATE SPACE RECONSTRUCTION

We analyse the same set of 12 N2 worms crawling on food-free plates as in Chapter 3. The measurements consist of a $T \times 5$ measurement matrix Y consisting of 5 eigenworm coefficients for a recording of duration $T = 33600$ frames, sampled at 16 Hz (for a total of 35 minutes). We stack $(K-1)$ time-shifted copies of Y to give the $(T-K+1) \times 5K$ trajectory matrix $\overline{Y}_K$. For each K, we estimate the maximum entropy as a function of the number and position of the partitions in state space, h (see Methods). As we increase K, the entropy quickly decreases until $K \sim 6$ frames, after which it slowly drifts but remains unchanged within error bars, Fig. (5.1-left). As a guide, we plot the change in entropy rate as a function of K, Fig. (5.1-left,inset), and choose K when the slope of h stops changing: we choose $K^* = 10$ frames. We then do SVD and whitening on $\overline{Y}_K$ and follow the maximum entropy rate as a function of m, Fig. (5.1-right). The entropy drops until $m \sim 6$ dimensions, in agreement with what we found in [1], despite using a very different method. Since $h(m)$ only provides a lower bound to the state space dimension, we make a conservative choice of $m^* = 10$ for reconstructing the transfer operator on phase space densities. This choice of K^* and m^* yields an estimate of the Kolmogorov-Sinai entropy of $\hat{h}_{KS} = 1.33(1.27, 1.38)$ (nats/s), which is comparable to the estimate obtained through the sum of positive Lyapunov exponents in [1], yet slightly larger. However, the near symplectic structure found in the spectrum of Liapunov exponents [1] combined with the growth of the number of positive exponents with the embedding dimension reported in Fig. (S8) of [1] indicates that a higher dimensional embedding might result in a larger upper bound for h_{KS}. From this choice of K^* and m^*, we build an ensemble embedding across all worms in the dataset, and build partitions on the combined state space.

5.2.2. COHERENT SETS CORRESPOND TO LONGER TIME SCALE MOVEMENTS: FORWARD RUNS AND PIROUETTES

As in Chapter 4, we estimate a lower bound for the transition time τ of the reversibilized transfer operator R_τ, Eq. (4.3), by looking the implied time scales t_{imp}, Eq. (4.2), as a function of τ, using $N = 4000$ partitions. Recall that a Markov chain respects the Chapman-Kolmogorov identity, and therefore the implied time scales, Eq. (4.2), should remain unchanged with increasing τ. Fig. (5.2A) indicates that even at sampling time the

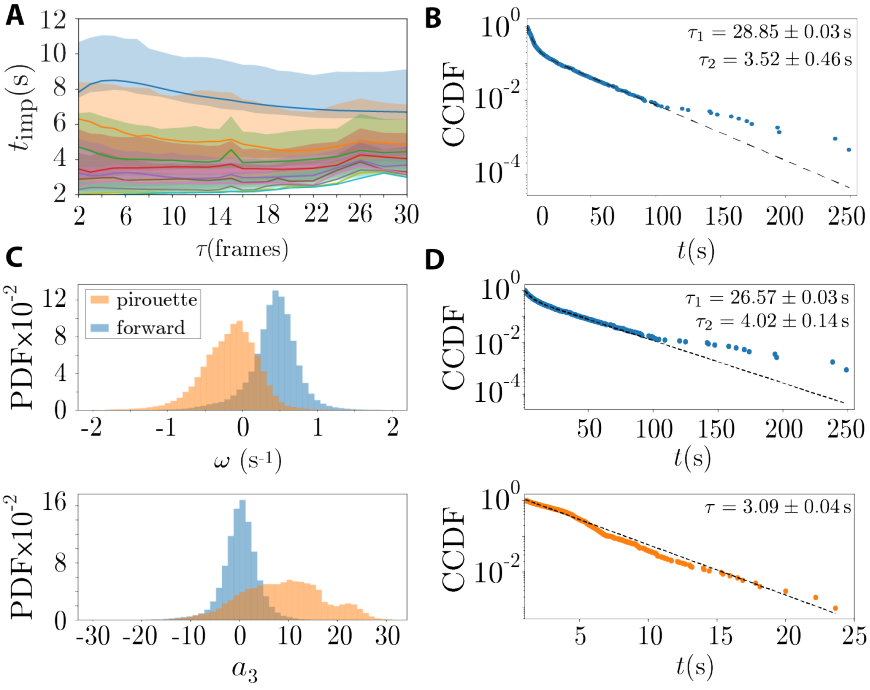

Figure 5.2: **Transfer operator approach reveals longer time scale movements: forward runs and pirouettes in foraging N2 worms.** (A) - Implied time scales t_{imp} of the first 10 non-trivial eigenfunctions (color coded) of the reversibilized transfer operator as a function of τ, with $N = 4000$ partitions of the state space. The implied time scales quickly converge, indicating that the Markov chain is approximately Markovian. We choose $\tau = 4$ frames for subsequent analysis as to maximize the time scale separation. We bootstrap over 10^4 frame segments to obtain 95% confidence intervals. (B) - Complementary cumulative distribution function (CCDF) of the run times of the states obtained through fuzzy c-means clustering the first non-trivial eigenfunction of the reversibilized transfer operator (see Methods). The bulk of the dwell time distribution approximately follows a bi-exponential distribution, consistent with the existent of two coarse-grained states: a longer lived run and a shorted time scale pirouette. Interestingly, unlike [22], the run length distribution is heavy-tailed, indicating that some worms perform longer time scale runs not captured by a simple two state model. (C) - Probability density functions (PDF) of the phase velocities ω and turning amplitudes a_3. The blue state corresponds to forward runs, with positive phase velocities ω and low values of a_3. The orange state corresponds to pirouettes: reorientations events composed of reversals (negative ω) coupled to turns (large a_3). (D) - Complementary cumulative distribution function (CCDF) of the dwell times in each of the coarse-grained states. (D - top) The forward states is longer lived, with run duration on the minute time scale. A bi-exponential fit serves to identify roughly shorter and longer lived forward runs, but fails to capture the heavy tail of the distribution. (D - bottom) The pirouettes are shorter lived ($\sim 5s$) and well approximated by a single exponential decay time. Confidence intervals in (A) are 95% bootstrapped confidence intervals. In (B) and (D) the errors are the standard deviations coming from the covariance matrix of the least squares regression.

transfer operator is approximately Markovian: we choose $\tau = 4$ frames for the subsequent analysis in order to maximize the time scale separation. Note that for larger τ the relaxation time scales of the different eigenfunctions start collapsing as the system mixes. We use the longest lived eigenfunction of the reversibilized transfer operator to partition the state space into coherent sets using fuzzy c-means clustering (see Methods). In Fig. (5.2B), we look at the distribution of run times for these two states[1]. The bulk of the distribution is well approximated by two time scales, which is reminiscent of the results from Pierce-Shimomura et al. [22], where the distribution of run lengths was computed from the centroid motion and two behavioral states were defined: "forward" runs and "pirouettes". Note, however, that the distribution also exhibits long runs not captured by a simple two state model. To further interpret the coherent sets, we computed the body wave phase velocities ω (see Chapter 3) and the turning amplitudes (as measured by the projection onto the third eigenworm a_3, see Chapter 3) for each of the obtained states, Fig. (5.2C). The negative velocities and large turning amplitudes indicate that one of the states corresponds to reversals coupled to ventrally-biased turns, which matches the description of the pirouette state in [22]. The other state corresponds to forward runs, as indicated by the positive phase velocities and low turning amplitudes. In Fig. (5.2D) we look at the distribution of run lengths for these two states. The pirouette run length distribution is well approximated by a single exponential function. In contrast, the bulk of the forward states exhibits at least two time scales, but also a heavy tail with longer time scale runs, in agreement with the multiplicity of sub-states found in the forward crawling state we identified in Chapter 3. These results also match the finding, discussed in Chapter 2, that the run length distributions of the forward state (computed from centroid trajectories), exhibited heavy tails not captured by a simple random telegraph process with two time scales (see Fig. (S7) in [23]). Therefore, the longer forward runs exhibited by some worms are likely part of a distinct neuromodulatory control process, possibly during the dispersal behavior [24]. Nonetheless, understanding how these longer runs are generated an controlled remains an interesting open question, highlighted by our approach. Finally, the fact that we identify short forward states with a com-

[1] Runs shorter than 1s were discarded in order to avoid noisy transitions at the boundary between sets and to match the sampling time in [22] for ease of comparison.

parable time scale to pirouette events indicates that classifying pirouettes through the run lengths of the centroid position can be misleading [22].

5.2.3. SEQUENTIAL SUBDIVISION OF COHERENT SETS IDENTIFIES INTERPRETABLE FINER SCALE BEHAVIORS

Given the complexity of the forward state, we wondered whether we could find interpretable finer scale structure in behavior. In order to do that, we sequentially subdivide the most cohesive coherent set, found by inspecting the spectrum of the operator built only from the microstates in each coherent set. The most cohesive state takes longer to relax to the invariant distribution, and is identified by finding the largest non-trivial eigenvalue among coherent sets. Once identified, we subdivide the most cohesive coherent set into two states through fuzzy c-means clustering (see Methods). We find that pirouettes are slightly more cohesive than the forward state. This agrees with the previous finding connecting the likelihood of turns given the length of reversals [24], showing that these two behaviors generally occur sequentially in time, resulting in a larger coherence. Subdividing the pirouette state yields shallower pirouettes and deeper turns, Fig. (5.3A). At the next iteration, we split the forward state into faster and slower forward crawling, Fig. (5.3B). Note that the slow forward state can also be considered almost a pause state, since the distribution of phase velocities is almost centered around 0. Also, we note that this state exhibits a dorsal bias. In fact, the next iteration splits this slow forward state further, revealing dorsal turns, Fig. (5.3C). We were surprised with this finding, as this indicates that dorsal turning (which accounts for only $\sim 1\%$ of the events in this dataset) usually occurs in combination with forward movement. The fact that ventral turns generally occur after a reversal, while dorsal turns generally occur during forward locomotion, indicate very distinct neuromodulatory control mechanisms for these two types of turns [25]. Note that this would have been completely overseen in a centroid based description, highlighting the importance of studying behavior at a postural level.

Our approach for subdividing a Markov chain follows [26], but this approach is not unique. The method for finding optimal coherent sets is backed by the spectral theory of Markov chains [27], but the subdivision of Markov chains in more than two states does not retain the same theoretical understanding. As such, various different heuristic methods have

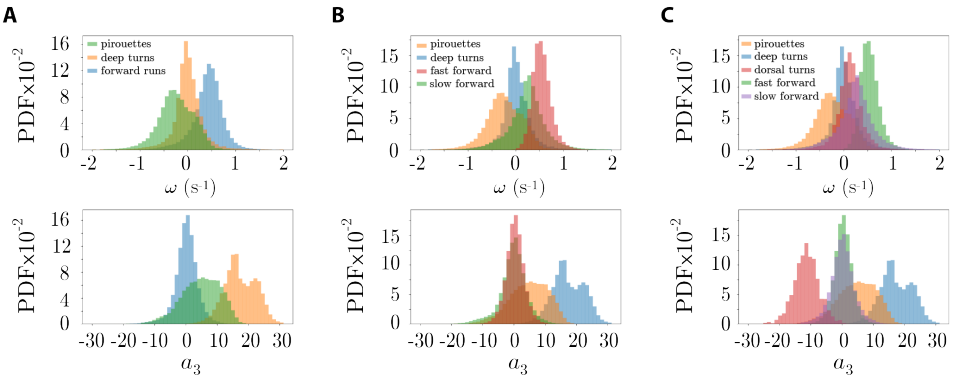

Figure 5.3: **Sequential subdivision of the state space through the transfer operator approach identifies substructure in behavior.** At each iteration step, we identify the most cohesive subset by computing the first non-trivial eigenvalue of the sub Markov chain built from the microstates in each coherent set. (A) - The first iteration splits the pirouette state into shallower pirouettes (reversal followed by shallow Ω-turns) and deeper Ω and δ-turns [21]. Note that the fact that the largest non-trivial eigenvalue was sitting in the pirouettes indicates they are more cohesive as a "state" than the forward state which seems to be composed by a multiplicity of substates. (B) - The subsequent step splits the forward state into faster and slower forward movement. Note that the slow forward state also exhibits a dorsal bias (as seen be the left skew in the a_3 distribution). (C) - The slow forward state in forward split into deeper dorsal turns, and slow movements (pause-like states). We note that these sub states result from a particular choice of subdivision procedure, as there exist other methods for subdividing the Markov chain. Therefore, the biological relevance of such substates is questionable. Nonetheless, this analysis shows that we can also use the transfer operator to get at finer time scale movement control. In addition, these coherent sets are dependent on the transition time scale (chosen as $\tau = 4$ frames, Fig. 5.2). If τ is chosen significantly larger, it will not disrupt the Markovian structure of the transition matrix but it might yield different substructures in behavior. In principle, τ should be optimized at each iteration step. Nonetheless, these results are robust exact choice of τ at each iteration step.

been proposed that either make use of more eigenfunctions to partition the system into more macrostates, or employ an hierarchical partitioning scheme similar to the one we have employed here [26, 28].

5.2.4. TRANSFER OPERATOR OFFERS REALISTIC MODEL OF *C. elegans* POSTURAL DYNAMICS

The approximation of the transfer operator on phase space densities also offers an effective model of the dynamics: a diffusion process in which the system hops between microstates according to the transition probabilities. Can this model accurately represent the complex postural dynamics of *C. elegans*? Focusing on an example worm, we estimate the transition matrix with $\tau = 4$ frames, we generate new sequences by sampling from the conditional probability at each state (see Methods). In Fig. (5.4), we show the distribution of dwell times in the two macrostates previously identified (forward and pirouettes) for the data (dashed lines) and simulations (black lines). Remarkably, the simulations capture the transition kinematics accurately over a wide range of time scales (from milliseconds to minutes). Note, however, that the forward state simulations overestimate the frequency of $\sim$ 10s runs and underestimates the frequency of longer runs $\sim$ 100s, which is consistent with the heavy tailed distributions found in Fig. (5.2D). This means that the heavy-tailed structure in the run length distribution is not even captured by a full microstate model. In Fig. (5.4B,C), we compare the simulations with the measurement time series used to reconstruct the state space and approximate the transfer operator. Recall that we started with a $T \times 5$ time series, for the projections along the first 5 eigenworms [20]. In order to obtain a time series of eigenworm coefficients from the simulations, we proceed as follows. For each new discrete microstate in the simulation, we randomly pick a state space point from the points within that microstate. We then project back the state to the full trajectory matrix, $\overline{Y}_K$ and extract the last measurement from the K frames window. As we have discussed in Chapter 3, the first two modes a_1 and a_2 exhibit a circular joint distribution, and the phase along that circle captures the body wave phase. In addition, a_3 essentially measures the turning amplitude. In Figs. (5.4B,C), we show the distribution of eigenworm coefficients obtained from simulations. Remarkably, the simulations not only capture the transition kinetics between coarse-grained states, but also fine scale details in the distribution of eigenworms

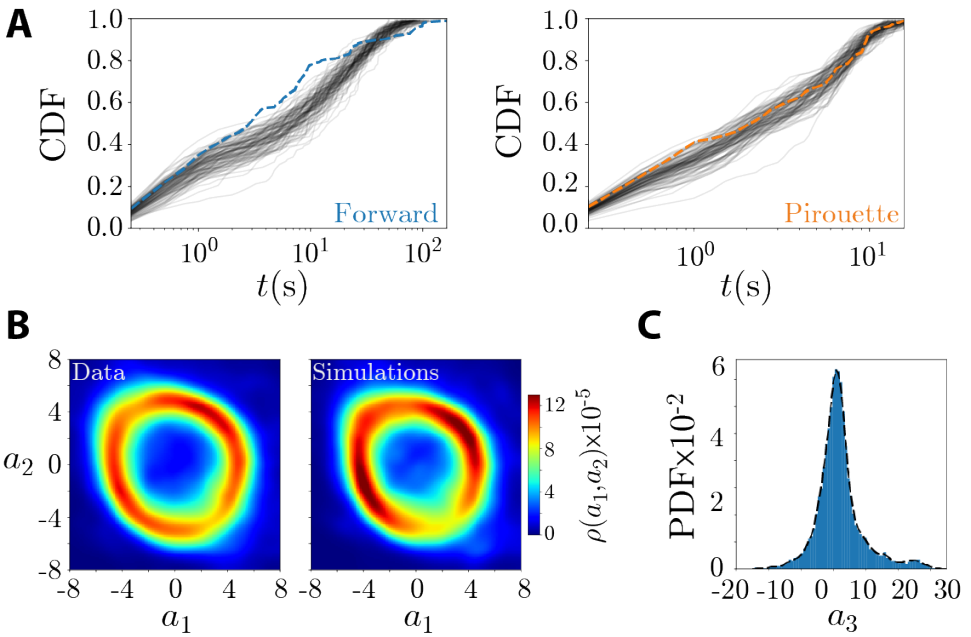

Figure 5.4: **Simulations done with the transfer operator capture foraging behavioral dynamics across scales.** (A) - Cumulative distribution function (CDF) of the dwell time in each of the macrostates identified in Fig. (5.2). Blue and orange dashed lines represent "forward" and "pirouette" states respectively, while black line represent 100 different simulations. Simulations capture the broad statistics of forward to pirouette transitions, except for minor differences around the ~ 10s time scale and the very tail of the distribution ~ 100s of forward runs. (B) - Joint probability distribution of the first two eigenworm projections $\rho(a_1, a_2)$ for the data (left) and simulations (right). (C) - Probability distribution function (PDF) of the turning amplitude a_3, compared to the simulations (black dashed line)

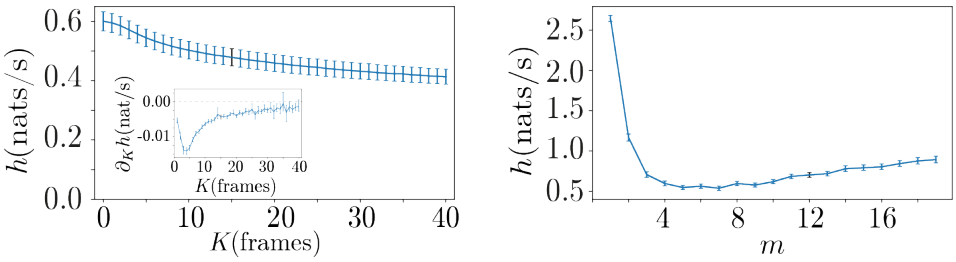

Figure 5.5: **State space reconstruction of N2 worms freely moving on a bacterial lawn.** (left) - Maximum entropy rate as a function of K, averaged over 150 worms. The entropy rate drops quickly until $K \sim 15$ frames, after which it slowly decreases (almost linearly) as a function of K. We choose $K^* = 15$ frames. (right) - Maximum entropy rate as a function of the number of the state space dimension, m. The entropy drops and reaches a plateau at ~ 6 dimensions. To be conservative, we choose $m^* = 12$. Error bars are 95% confidence intervals bootstrapped over worms.

coefficients. In this way, we are capable to faithfully simulate the complex postural dynamics of *C. elegans* over multiple time scales, using a single linear Markov operator. Previous attempts at modelling *C. elegans* posture dynamics relied on more complex models of the posture time series, like deep neural networks [29]. Here, by thinking principally about the definition of state and subsuming the nonlinearity into the transfer operator, we are able to faithfully capture the dynamics using a single linear operator. These simulations could also be used to generate realistic centroid trajectories using linear and non-linear resistive force theory [30], which would then directly compare with the results of Chapter 2.

5.3. WILD-TYPE WORMS ON A BACTERIAL LAWN: EXTRACTING LONGER TIME SCALE BEHAVIOR

In the previous section, we have studied the postural dynamics of a collection of N2 worms crawling off food for 35 minutes after a habituation period of 5 minutes. Given such conditions, worms are generally starved during most of the recording and exhibit a dispersion behavior in which they try to explore as much of the plate as fast as possible [24]. In such a scenario, the internal state of the worms with regards to hunger was very similar across all worms, which might be why we did not find signif-

icant longer time scale changes in behavior. On the contrary, worms on food exhibit minutes long bouts, broadly categorized as "roaming" and "dwelling" [31–33], in which the worms switch between local search and long range exploration, that can last up to ~ 25 minutes [32]. In this section, we will study the postural dynamics of N2 worms crawling on food-full environment, in which we hope to be able to observe distinct internal states, since food is known to strongly impact behavior in multiple ways [18, 34–38].

5.3.1. STATE SPACE RECONSTRUCTION

Trajectories from 150 N2 worms crawling on a bacterial lawn were collected, and the body posture tracked using a custom-made machine learning solution (see Methods). The posture trajectories were then projected onto the same set of eigenworms used in the off food worms (see Chapter 3) for ease of comparison, as these provide a good basis for *C. elegans* body posture across a variety of environmental and genetic perturbations [40]. Measurements thus consist of the first five eigenworms coefficients as a function of time, sampled at ~ 30 Hz for 15 minutes (see Methods). These 5D eigenworm trajectories were then used to build trajectory matrices, $\overline{Y}_K$, and we studied the entropy rate h as a function of K (see Methods). As in the off food worms, the entropy first drops quickly and then the slope gets closer to 0, Fig. (5.5A). As discussed in the previous chapter, this slow loss of information could be due to the fact that we are start including longer time scale processes into the definition of state. However, a deeper theoretical understanding of the long K behavior of the entropy rate estimates is needed to fully interpret these results. Our approach is to choose K such that we can capture the faster time scales without a significant loss in predictability: we choose $K^* = 15$ frames. As a function of the state space dimension m, the entropy quickly decays achieving a broad plateau at ~ 6 dimensions, Fig. (5.5B). We make a conservative choice of $m^* = 12$, which results in an estimate of the average Kolmogorov-Sinai entropy across worms of $\hat{h}_{KS} = 0.70(0.68, 0.73)$ (nat/s), much smaller than the entropy rate found off food: the behavior of the worms while crawling on food is on average more predictable than the behavior off food. From this choice of K^* and m^*, we build an ensemble embedding across all worms in the dataset, and build partitions on the combined state space.

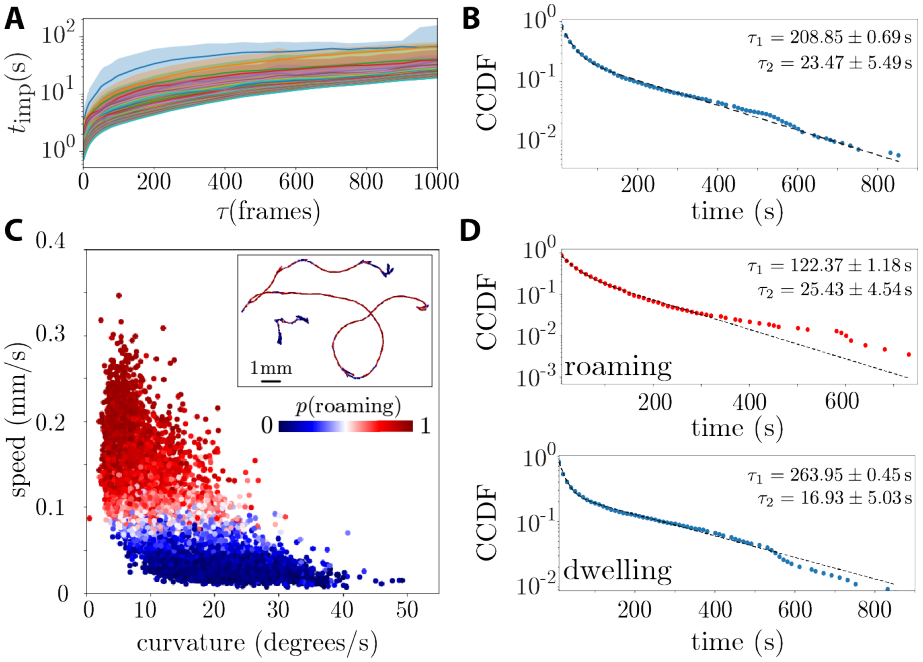

Figure 5.6: **Transfer operator approach reveals long time scale exploration-exploitation trade-off in N2 worms freely moving on a bacterial lawn.** (A) - Implied time scales t_{imp} of the first 50 non-trivial eigenfunctions (color coded) of the reversibilized transfer operator as a function of transition time τ, using 4000 partitions. Unlike the off food experiments, Fig. (5.2), now the dynamics exhibits modes that are much longer lived $t_{imp} \to 100$s. We choose $\tau = 300$ frames for subsequent analysis. We bootstrapped over 10000 frame segments to obtain 95% confidence intervals. (B) - Complementary cumulative distribution function (CCDF) of the run times of the states obtained through clustering the first non-trivial eigenfunction of the reversibilised transfer operator (see Methods). For ease of comparison with previous work [31, 32, 39], we averaged the probability of belonging to either state in 10s windows, and assigned them the most likely average state. The distribution of lifetimes is well approximated by a bi-exponential distribution. This suggests the existence of at least two coarse-grained states, and is reminiscent of the work from Fujiwara et al. [39] that used the distribution of runs to distinguish between "roaming" and "dwelling" states. (C) - Path curvature and the centroid speed (averaged in 10s windows), color coded by the probability of belonging to each coherent set: the two coarse-grained states correspond to the "roaming" and "dwelling" states described by Ben Arous et al. [31]. Therefore, the long lived eigenfunction of the reversibilized transfer operator indicates an exploration-exploitation trade-off in worm behavior. (C - inset) - Sample centroid trajectories color coded by the probability of roaming. (D) - Dwell time distribution for the roaming (blue) and dwelling (red) states. The dwelling state is well approximated by a bi-exponential distribution, and is generally longer lived than the roaming state. The roaming state exhibits a heavy tail with long runs not falling into a bi-exponential approximation of the distribution. Errors in the estimated time scales were obtained from the covariance matrix of the least squares regression.

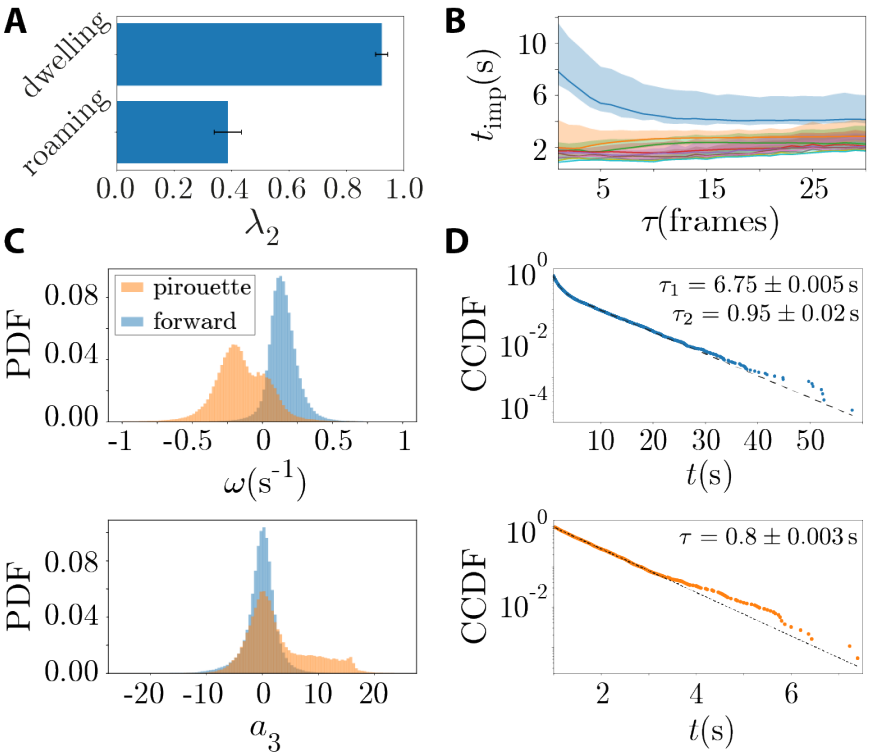

Figure 5.7: **The roaming state exhibits qualitatively similar coherent sets as N2 worms foraging off food.** (A) - First non-trivial eigenvalues of the sub Markov chain built from the roaming and dwelling microstates indicates that the roaming state is less coherent than the dwelling state (it relaxes faster to the invariant distribution). Error bars are bootstrapped standard deviations over 500 frame segments. (B) - Implied time scales t_{imp} of the first 10 non-trivial eigenfunctions (color coded) of the reversibilized transfer operator built only from the roaming microstates. Unlike the whole phase space, trajectories from the roaming state don't exhibit long time scales. We choose $\tau = 10$ frames for subsequent analysis. We bootstrap over 500 frame segments to get 95% confidence intervals. (C) - Distribution of phase velocities ω and turning amplitudes a_3 indicate that the first two coherent sets inside the roaming state correspond to forward runs (blue) and pirouettes (orange). (D) - Dwell time distribution for the forward and pirouette states. Pirouette run time distribution is well approximated by single time scale, while the forward state exhibits at least two time scales. In general, run lengths are shorter than in the off condition, Fig. (5.2D).

5.3.2. COHERENT SETS CAPTURE LONG TIME SCALE CHANGES IN MOTILITY: ROAMING AND DWELLING

We computed the implied time scales of the reversibilized Markov operator built with $N = 4000$ partitions, and found that the longest relaxation time scale is almost an order of magnitude larger than the one found off food, Fig. (5.2A). In addition, the implied time scales only converge after ~ 200 frames, and we choose $\tau = 300$ frames for subsequent analysis. The longest lived eigenfunction is used to attribute the probability of belonging to one of two coherent sets through fuzzy c-means clustering. In order to make the comparison with previous work on longer time scale dynamics from a centroid level perspective [31, 32, 39], we averaged the probability of belonging to either state in 10s windows. Assigning each 10s window to its most likely state, we combine microstates into coarse-grained states. The run time distribution of these two states closely follows a bi-exponential distribution, Fig. (5.6B), consistent with the results from Fujiwara et al. [39]. In [39], run lengths were estimated by segmenting the trajectories using a threshold in the path curvature, and "roaming" and "dwelling" states defined using the intersection between two exponential distributions fit to the run lengths. We find similar behavior, with the distribution being well fit by a bi-exponential function: the exponentials cross at $t_{\text{crit}} = 40.1$s, which is comparable to $t_{\text{crit}} = 44$s reported in [39]. In addition, the relative weight of the exponential functions indicates that $\sim 24\%$ of the run durations are long, which is in very good agreement with the results of Fujiwara et al. [39] for the duration of the state they defined as "roaming". We set out to further dissect the nature of these two coarse-grained states, and looked at the speed and curvature (computed from centroid trajectories) averaged in 10s windows (as in [31, 32]). In Fig. (5.6C), we color code each point according to the probability of belonging to one of the states, now called "roaming" state. There is indeed a very clear separation between low speed, high curvature states, defined as "dwelling", and high speed, low curvature states, defined as "roaming" [31, 32]. In Fig. (5.6C - inset) we show two centroid trajectories color coded by the probability of belonging to the roaming state, which highlights the fact that the longest lived eigenfunction lies along an exploration-exploitation axis, reminiscent of the "roaming-dwelling" mode found in Chapter (2) using a centroid-based analysis of the dynamics. Given these two alternative definitions of coarse-grained states: one

based on run lengths and the other based on speed and curvature, we set out to study the run lengths of each of the states, Fig. (5.6D). Interestingly, we find that both roaming and dwelling states exhibit long and short runs, which indicates that classifying states merely based on run lengths might be misleading. In addition, the roaming run lengths exhibit a heavy tail that does not fit a simple two-state model, and is qualitatively similar to the distribution of run lengths found in the off food worms, Fig. (5.2B).

5.3.3. IDENTIFYING SUBSTRUCTURE WITHIN THE ROAMING STATE

We decided to focus on the roaming state and study behavioral substructure within it. We built a Markov chain using only the microstates of either the roaming or dwelling state, and found that the dwelling state exhibits more cohesive coherent subsets, as seen by the magnitude of the first non-trivial eigenvalue conditioned either on the dwelling microstates or the roaming microstates, Fig. (5.7A). For the roaming states, we find that the implied time scales do not exhibit long time scale dynamics, Fig. (5.7B), relaxing an order of magnitude faster to the invariant distribution conditioned to the roaming state, than the dynamics on the full state space relaxes to the full invariant distribution, Fig. (5.6A). We choose $\tau = 10$ frames for subsequent analysis. Clustering the longest lived eigenfunction of the reversibilized operator yields coherent sets that correspond to forward states and pirouettes, Fig. (5.7C), much like what we found for worms on food-free plates, Fig. (5.2). Note, however, that the body wave phase velocity is much smaller in roaming worms on food, compared to worms off food, in agreement with previous studies at a centroid level [24]. In addition, we do not find deep δ-turns in worms crawling on food, and the run lengths are much shorter when the worms are on food Fig. (5.7D), compared to worms off food Fig. (5.2D).

5.4. MUTATION IN THE NPR-1 NEUROPEPTIDE RECEPTOR DISRUPTS LONG TIME SCALE DYNAMICS

In the previous section we have seen how the presence of food strongly affects behavior: worms exhibit long time scale changes in behavior char-

acterized by high speeds, low curving rates (roaming), and low speeds, high curving rates (dwelling). We have also found that the faster moving state on food (roaming) is slow in comparison with off food behavior, and that on food worms do not perform long pirouettes coupled with deep δ-turns. In order to further understand these changes in behavior with the food conditions, we decided to study the behavior of *npr-1 (ad609)* mutants, which exhibit a modified response to food [36], consistently roaming more across and during different developmental stages [41]. *npr-1* mutants are hypersensitive to the arousing effects of environmental oxygen and pheromones [42–45], due to the lack of inhibition of the neuropeptide receptors in a set of sensory neurons, and therefore consistently move more than N2 worms on food.

Trajectories from 7 *npr-1* worms crawling on a bacterial lawn for 15 minutes were sampled at 20 Hz, and the body posture tracked using a novel deep network based solution (see Methods). As before, we project the posture trajectories into the same set of eigenworms used in the off food worms, generating a 5D measurement time series. We then studied how the entropy rate changed as function of how many delays K we include in the definition of state (see Methods). The entropy rate quickly drops and reaches a broad plateau at $K \sim 6$ frames (within error bars), although exhibiting a consistent slow drift, Fig. (5.8A - left). We choose $K^* = 11$ frames. As a function of m, we see that after ~ 4 dimensions we capture the predictability of the system, Fig. (5.8A - right). We make a conservative choice of $m^* = 8$, which results in an estimate of the average Kolmogorov-Sinai entropy across worms of $\hat{h}_{KS} = 1.34(1.30, 1.37)$ (nat/s), which is much larger than the entropy rate of N2 worms on food, Fig. (5.5) and much closer the entropy rate exhibited by N2 worms crawling off food, Fig. (5.1). This agrees with the finding that the *npr-1 (ad609)* mutant exhibit lower average compressibility than wild type N2 worms on food [46, 47], although our results show a much starker difference between *npr-1* and N2 worms on food than the one reported in [46].

Remarkably, the implied time scales indicate that the *npr-1* mutation essentially removes the long time scale modes from the dynamics that we found for N2 worms on food, Fig. (5.8B), and the spectrum is qualitatively more similar to the one found in N2 worms off food, Fig. (5.2A). Nonetheless, the primitives of behavior that we have previously identified (forward runs and pirouettes), are still found in *npr-1* mutants by cluster-

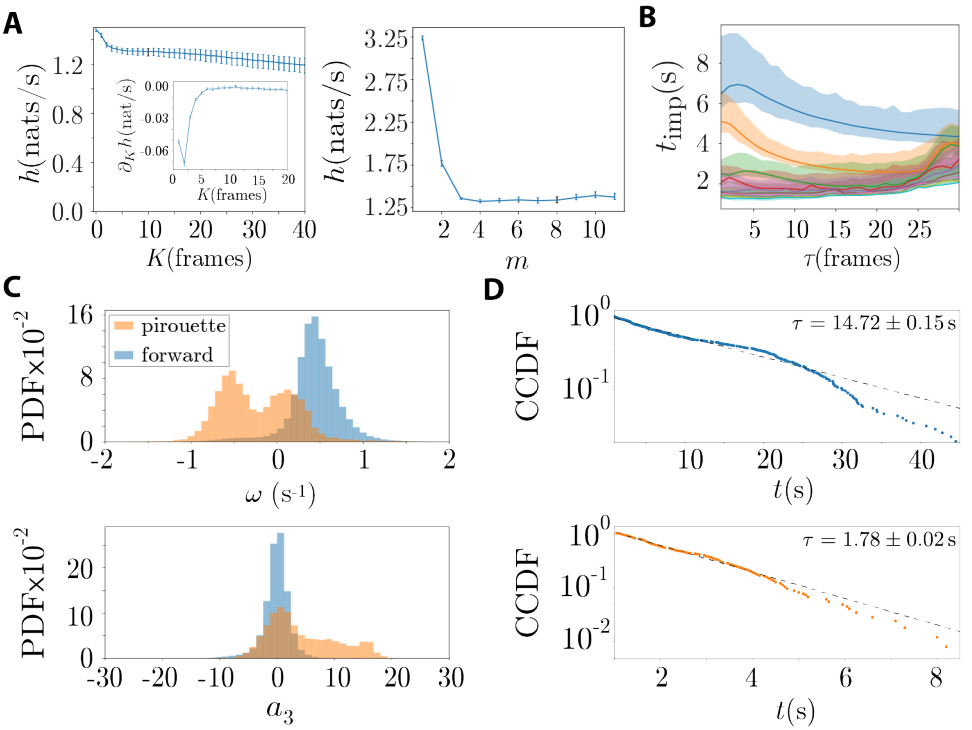

Figure 5.8: **Mutation in a neuropeptide receptor gene (NPR-1) removes long time scale dynamics.** (A-left) - Maximum entropy rate as a function of K, averaged over 7 worms. The entropy rate drops quickly until $K \sim 8$ frames, achieving a short plateau after which it slowly decreases (almost linearly) as a function of K. We choose $K^* = 11$ frames. (A-right) - Maximum entropy rate as a function of m. With increasing m, the entropy drops and reaches a plateau at ~ 4 dimensions. We choose $m^* = 8$. Error bars are 95% confidence intervals bootstrapped across worms. (B) - Implied time scales t_{imp} of the first 10 non-trivial eigenfunctions (color coded) of the reversibilized transfer operator, as a function of transition time τ, with 2000 partitions on the state space. Unlike N2 worms on food, *npr-1* mutants do not exhibit long lived modes. We choose $\tau = 4$ frames for subsequent analysis. Error bars are 95% confidence intervals bootstrapped over 2000 frame segments. (C) - Distribution of phase velocities ω and turning amplitudes a_3 indicate that the first two coherent sets correspond to forward runs (blue) and pirouettes (orange). (D) - Run time distributions for both states. Both forward and pirouette run lengths decay exponentially and, unlike the N2 worms, the run time distributions do not exhibit a heavy tail. Error estimates for the decay times are obtained from the covariance matrix used for least-squares regression.

ing the first non trivial eigenfunction of the reversibilized transfer operator, Fig. (5.8C). The run lengths of both states are longer than the ones found in roaming worms on food, Fig. (5.7D), and fits a simple exponential distribution: in this case we do not find heavy tailed run distributions. Therefore, even though the behavioral dynamics seems to make use of the same coarse-grained primitives (pirouettes and forward runs) as N2 worms off food and roaming N2 worms on food, the details of the transitions between states also change, being here much simpler than in the previous examples.

5.5. ANALYSIS OF PIROUETTES ACROSS EXPERIMENTS REVEALS DETAILS OF THE NEUROMODULATION OF REORIENTATION BEHAVIORS

Across experiments, pirouettes emerged alongside forward movement as one of the most important primitives of *C. elegans* behavior. This is in agreement with previous work in which the importance of pirouettes for navigation strategies is highlighted [22, 48–50]. However, we also find that pirouettes can be quite variable: some are longer and generally terminate in deep turns, others are shorter and composed of single reversal events. Broekmans et al. [21] found that ventral turns can indeed be split into two distinct classes, despite having similar kinematics. Some turns are shallower Ω-turns ($10 \leq a_3 \leq 20$), in which the worm barely touches its tail, and others are deeper δ-turns ($a_3 > 20$), in which the worm crosses itself turning to the dorsal side by overturning through the ventral side. In this section, we will look at the details of pirouettes across experiments and try to understand that variation in light of the environment (food vs off-food) and the mutation in the NPR-1 gene. For the on food condition, we consider only dynamics in the roaming state.

First of all, we see a large degree of variability across experiments regarding the duration of pirouettes and forward movement, Fig. (5.9A). In general, the longest locomotor bouts are found in N2 worms off food, for which the duration of forward runs is about an order of magnitude longer than the duration of reorientation events. This has been described as the "dispersal" behavior exhibited by worms when starved [24]. In stark contrast, worms roaming on food exhibit shorter run lengths, and the duration of forward and pirouettes is now comparable. Mutation in the *npr*-1

gene partially restores the longer runs, but not entirely. To further dissect the nature of these different pirouettes, and given our access to full postural data during entire reorientation events, we decided to look at the relationship between the duration of pirouettes and the depth of the subsequent turning event, as measured through a_3, Fig. (5.9B). Off food, we find that longer pirouettes (> 4s) generally end in deeper δ-turns, while shorter pirouettes either end in Ω-turns or forward motion. These results are in agreement with the finding that the length of reversal events is coupled to the likelihood of a subsequent turning event [24, 25, 50]. Strikingly, when the worms are roaming on food, we do not observe long reversals coupled to deep turns. Instead, we only found short pirouettes, most of them being just short reversals and some of them coupled to shallow turns. This is consistent with the recent work on escape response behavior [21], where it was shown that worms foraging off food exhibit deep δ-turns while escape behavior on food occur only through shallower Ω-turns. Mutation in the *npr*-1 gene partially recovers some of the longer pirouettes, but not the deep δ-turns.

In order to understand whether worms use these different types of pirouettes for distinct movement strategies, we looked at the frequency of different types of pirouettes across experiments, Fig. (5.9C). In general, N2 worms roaming on food exhibit a larger frequency of pirouettes, although these pirouettes are generally short and not coupled to deep turns. We defined short and long pirouettes through a threshold at $t_{\text{pirouette}} = 2$s and we can see that the frequency of longer pirouettes is significantly suppressed when N2 worms are roaming on a food environment. In addition, we see that the *npr-1* mutation partly recovers the off food behavior of N2 worms, but there are still important differences since *npr-1* mutants do not exhibit long pirouettes coupled with δ-turns. The lack of long pirouettes in the roaming behavior of N2 worms on food is consistent with the idea of a goal directed search done when worms are in a roaming state [31, 32, 51], in which quick reorientations serve to correct the direction of locomotion. These differences suggest that longer pirouettes serve a different movement strategies compared shorter pirouettes.

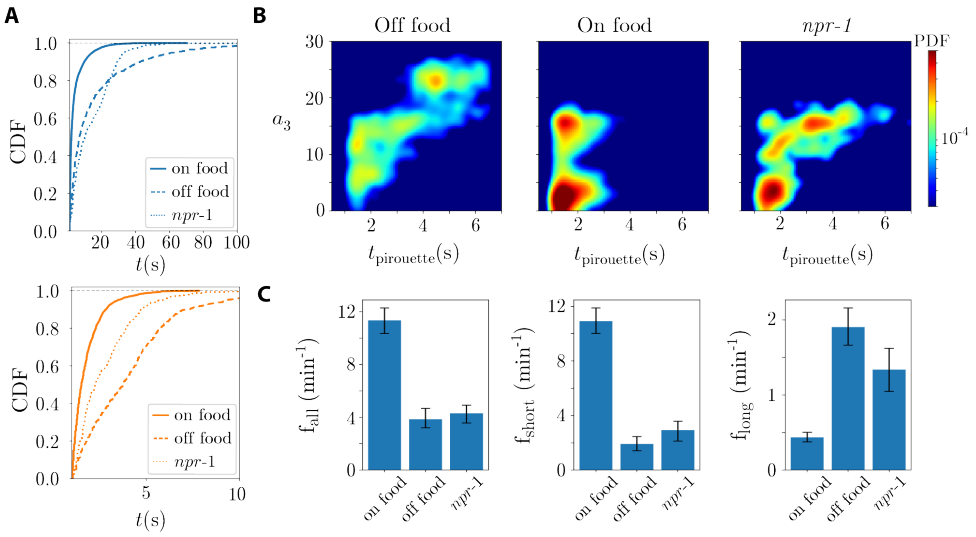

Figure 5.9: **Changes in length and depth of pirouettes across environments and *npr-1* mutation reveal patterns of neuromodulation of reorientation behaviors.** (A) - Cumulative distribution function of forward (blue) and pirouette states (orange) for N2 worms roaming on food, N2 worms off food, and *npr-1* mutants. On food, both forward and pirouettes run length are heavily suppressed. *npr-1* mutants exhibit higher run lengths than worms roaming on food, but not as long as N2 worms off food. (B) - Joint probability density function (PDF) of turning amplitudes and run lengths for pirouettes identified in different conditions. (B - left) Off food, N2 worms exhibit longer pirouettes which are coupled to deep δ-turns ($a_3 > 20$) [21]. The joint distribution exhibits roughly two other peaks: shorter pirouettes in which the worm does not turn (reversals) and slightly longer pirouettes that result in Ω-turns ($10 \leq a_3 \leq 20$) [21]. (B - center) When roaming on food, N2 worms do not perform deep reorientation events. Instead, most pirouettes are either short reversals or short reversals coupled to shallow Ω-turns. (B - right) *npr-1* mutants exhibit a higher frequency of longer pirouettes coupled to Ω-turns, but do not recover the deeper δ-turns found in N2 worms off food. (C) - Frequency of pirouettes per minute: we split pirouettes into short and long by a threshold at $t_{thresh} = 2$s. (C - left) N2 worms roaming on food exhibit a much higher frequency of pirouettes. Mutation in the NPR-1 gene recovers the off food pirouette rate. (C - middle) The frequency of short pirouettes is much larger in N2 worms on food compared to N2 worms off food and *npr-1* mutants. (C - right) The frequency of long pirouettes is largely reduced in N2 worms roaming on food, and the *npr-1* mutation nearly recovers the frequency of long pirouettes. In the analysis of figures (B) and (C) only runs longer than 1s were considered to avoid noise assignment of states (at the border between coherent sets).

5.6. LONG RANGE CORRELATIONS AND SCALING IN THE SLOW MODE DYNAMICS

The decomposition provided by the eigenfunction of the Perron-Frobenius operator offers the possibility of trying to find phenomenological models of the slow mode dynamics. In Chapter 4, we relied on the closed form of the equations of motion to essentially trade-off fast chaotic dynamics by a Wiener process, and build a phenomenological description of the system on longer time scales. In fact, this is just one out of a number of methods to construct reduced dynamics for slow variables [52]. The general idea is to try to find a subspace of Hilbert space that evolves slowly according to the dynamics, and to push the orthogonal space onto a noise-like term and sometimes a memory kernel, much like the Mori-Zwanzig formalism [53, 54]. Practically speaking, learning such effective descriptions without access to the equations of motion is much more challenging, but in systems with a clear time scale separation it is possible to make use of the approximation the Perron-Frobenius operator and its adjoint, the Koopman operator, to learn effective coarse-grained slow dynamics [55–57].

Motivated by these examples, we decided to study how the projection onto the slowest non-trivial eigenfunction of the Perron-Frobenius operator ($P\psi = \lambda\psi$) changed over time in *C. elegans* locomotion. To get a sense of the low order properties of the dynamics we first looked at the autocorrelation function of the slowest mode $\langle \psi_2(t)\psi_2(t+\tau)\rangle_\tau$ for each experiment, Fig. (5.10A). What we found is intriguing: the dynamics exhibit long range temporal correlations that change across experiments. N2 worms crawling on food exhibit higher correlations at large τ, followed by N2 worm off food. The mutation in the NPR-1 gene seems to destroy the longer range correlations, as the autocorrelation function crosses zero at $\tau \approx 10$s. In Fig. (5.10B-top), we focus on the experiments on N2 worms and find power law behavior in the autocorrelation function by plotting in a log-log scale: the absolute value of exponent is lower when on food, indicating that correlations decay even slower on food than off food. We note that we find power law behavior over almost two orders of magnitude, but the autocorrelation function eventually crosses 0 at a time scale of approximately 250s (compared to the $\sim$ 900s of the recordings on food). Power law behavior is a signature of scale free correlations, and so we decided to take a renormalization group approach in time, similar to a block spin transformation [58], in which we average the slow mode

dynamics in short windows w and re-estimate the autocorrelation functions. By defining the correlation time as the time at which the autocorrelation function crosses 0, $\langle \psi_2^w(t)\psi_2^w(t+\tau_c)\rangle_{\tau_c} \approx 0$ (within the sampling time scale), and rescaling time accordingly, we find that the autocorrelation functions collapse, Fig. (5.10B-bottom), highlighting the scale free nature of the dynamics. This means that the correlation between 1s long behaviors spaced by a 10s is the same as the correlation between 5s behaviors on the same time scale.

5.7. DISCUSSION

By thinking carefully about the definition of state, and subsuming the nonlinear dynamics into the approximation of the transfer operator on state space densities, we have been able to find an approximately Markovian representation of the complex postural dynamics of *C. elegans* through a single linear operator. We not only get a predictive model of the dynamics, but also a means to decompose the dynamics into spatio-temporal modes with time scales that range from milliseconds to minutes. In this way, we have been able to bridge time scales from fine scale postural changes all the way up to variation in the way worms explore the environment. Bridging time scales has been presented as one of the main challenges of current research in the physics of animal behavior [7, 59, 60]. Generally, researchers focus on a specific time scale of interest, and tune the representation to that specific time scale. Here, we provide means for capturing a wide range of time scales under a single representation, opening up new important questions about how these time scales interact.

Applied to *C. elegans* foraging off food, our approach naturally captures the longer lived behaviors used to explore the environment: forward runs and pirouettes [22]. In addition, we can zoom further and extract finer scale behaviors analogous to the ones found in Chapter 3. Not only that, but we also learn that dorsal and ventral turns generally occur during forward and backward locomotion, respectively, indicating that these two types of reorientations are likely controlled by different neuromodulatory mechanisms [25]. When on food, long term biases in exploratory propensity emerge, which we naturally capture with our approach. The spectrum of the transfer operator exhibits longer lived modes, and these modes can be used to decompose the dynamics into interpretable long lived changes in behavior. We note that the length of some of the long

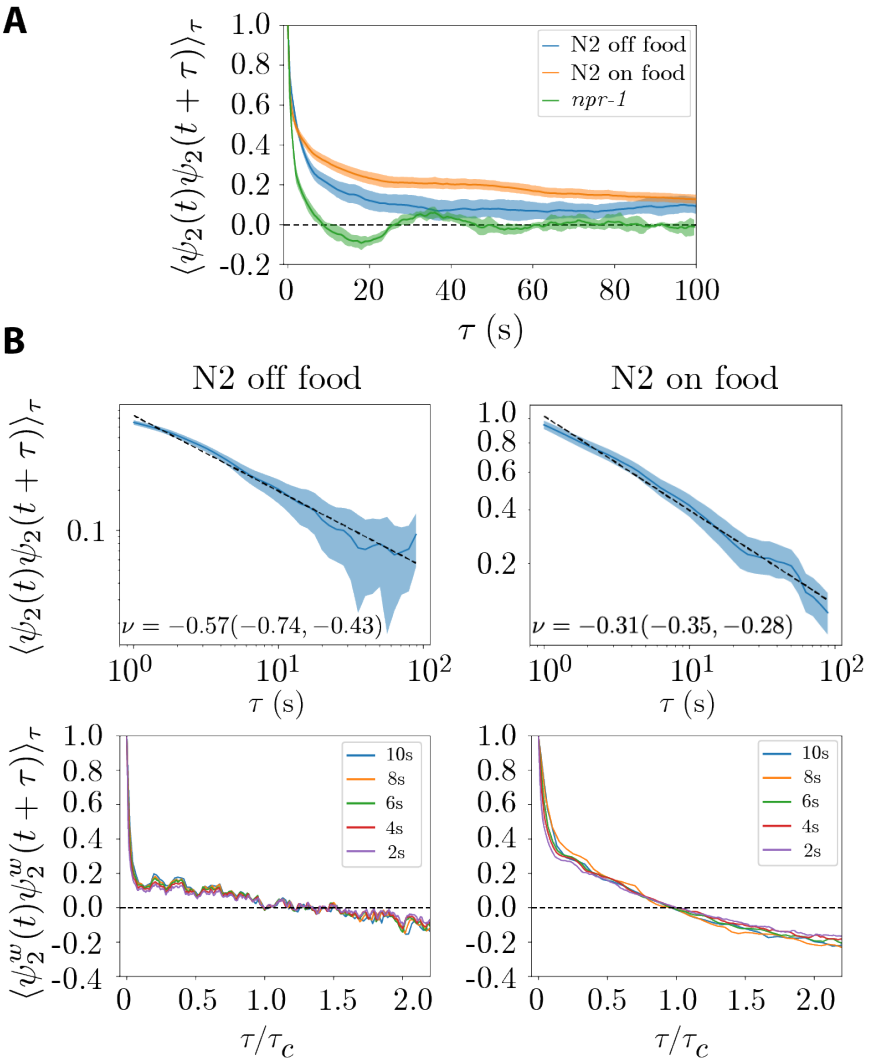

Figure 5.10: **Hints of scaling and long range correlations in the slow mode dynamics across experiments.** (A) - Autocorrelation function of the first non-trivial eigenfunction of the Perron-Frobenius operator for three different experiments: N2 worms off food, N2 worms on food and *npr-1* mutants on food. N2 worms exhibit long range correlations in the dynamics of the slow modes, while *npr-1* decays fast. (B-top) - Log-log plot of the N2 autocorrelation functions. The dynamics exhibits near power law behavior over almost two order of magnitude, with the exponent being modulated by the environment: on food the correlations decay slower. (B-bottom) - Autocorrelation functions of locally-averaged dynamics collapse after rescaling by the time scale of zero-crossing, τ_c. Shading and error bars in the exponent estimation, ν, are 95% confidence intervals bootstrapped across worms.

lived exploratory states is almost of the order of magnitude of the recordings (15 minutes), which impacts our estimates of the run length distributions. Bringing this analysis to longer time scale recordings is a future research goal. Comparing the roaming state with the behavior of the worms off food, we find important differences both in the transition kinematics (shorter overall dwell times) and in the overall speed and turning amplitude found in each behavior (lower speed and shallower turns on food). Nonetheless, there are qualitative similarities regarding the primitives of behavior: composed of forward runs and pirouettes. Making use of the ease of genetic manipulations in *C. elegans*, we studied the postural dynamics of *npr-1* mutants and found that the longer lived biases in behavior were essentially removed by this mutation. The behavior of these worms was closer to the behavior of N2 worms off food, but with important differences, which were made explicit by looking at details of pirouettes, as well as studying the dynamics of the longest lived eigenfunction.

By studying pirouettes, we found that δ-turns were absent when N2 worms are put on food and in the *npr-1* mutants, which is surprising given the fact that Ω and δ-turns are kinetically similar except for the magnitude of the turning amplitude [21], Fig. (5.2D). Tyramine orchestrated escape responses occur through GABA release by the VD motor neurons to the ventral muscles, which results in an asymmetry in the escape pirouettes that only occur ventrally [25]. Broekmans et al. [21] hypothesized that, if this neuromodulatory mechanism is preserved in foraging animals off food, then the purpose of δ-turns is to be able to turn dorsally by overturning to the ventral side. However, we also find that worms can exhibit deep dorsal bends (usually coupled to forward motion), Fig. (5.3C), and therefore this explanation is incomplete. Understanding how δ-turns are initiated and controlled by the nervous system, as well as how they are used for different movement strategies, remains an interesting open problem.

The differences in motility between *npr-1* mutants and N2 worms on food have been attributed to the hypersensitivity of these mutants to the arousing effects of environmental oxygen and pheromones [42–45]. The G-protein coupled receptor NPR-1 is expressed in the URX, AQR and PQR sensory neurons, and binding to the NPR-1 receptors inhibits the activity of these neurons and therefore the sensitivity to oxygen. The inhibition of these neurons results in the solitary feeding behavior exhibited by wild-type N2 [61], since social feeding is associated with lower oxygen concen-

trations to which N2 worms are insensitive through the inhibition of the URX, AQR and PQR neurons. *npr-1* mutants are unable to inhibit these neurons (because of the lack of NPR-1 receptors) and therefore exhibit enhanced arousing effects, as we have seen in Fig. (3.7), which results in the overriding of some of the typical behavior on food. On the other hand, dopaminergic signalling pathways act in response to mechanical stimulus from bacteria and have been associated with the slowing down and area restricted search behaviors in *C. elegans* [38, 62]. So, even though *npr-1* mutants are unable to dial down their arousal levels from a variety of stimuli, dopamine signalling is still present due to the stimuli from bacteria. In contrast, N2 worms off food are likely to underexpress flp-18 and flp-21, which have been identified as the ligands that bind to NPR-1 [63], and therefore do not inhibit the AQR, PQR and URX sensory neurons. Besides the lack of inhibition from binding to NPR-1 receptors, N2 animals off food also lack the dopaminergic signalling because they don't get the mechanical stimuli from the presence of bacteria. Therefore, one possibility is that it is only through the interaction between monoamine and neuropeptide signalling pathways that N2 worms off food are capable of eliciting deep δ-turns. Understanding how δ-turns are generated and controlled thus provides a means for a deeper understanding of the interaction between monoamine and neuropeptide signalling pathways [64].

By decomposing the dynamics into spatio-temporal modes in density space and focusing only on the longest lived modes, we learn an effective coarse-grained description of the system at large length and time scales, analogous to building hydrodynamic theories [65]. Power law behavior in the autocorrelation of hydrodynamic observables are a signature of out-of-equilibrium systems with conservation laws [66–70], and resembles the energy cascade found in turbulence [65]. The existence of heavy tailed run length distributions found in N2 worms are additional evidence of a self-organized criticality picture, characterized by the existence of avalanches of all sizes [71, 72]. As a biological system, the worm is inherently out-of-equilibrium, consuming energy and dissipating it throughout its life. In fact, the approximation of the Perron-Frobenius operator provides evidence of the breaking of detailed balance, with the appearance of complex conjugate eigenfunctions. The existence of conserved quantities is somewhat surprising, but it agrees with the near sym-

plectic structure we found for the Lyapunov spectrum in [1], and with the sub-critical dynamics of the locally linear models in Chapter 3. The fact that long range correlations disappear with the *npr-1* mutation indicate that these mutants fail to keep the conservation law. Indeed, studies have shown that the NPR-1 receptor is fundamental for maintaining micro-homeostasis in sleep behavior in the lethargus stage [14] and also for keeping the excitation-inhibition balance of motor neurons [73]. The organism evolved to keep a tight balance between the large number of interacting degrees of freedom in itself and the environment that surrounds it. It is the precise orchestration of those degrees of freedom, while keeping the system at the boundary between order and disorder, that results in slow hydrodynamics modes with scale-free correlations. The fact that we can perturb the organism and destroy the long range correlations provides important evidence for the picture of criticality in biological systems [74, 75], which in this case can be neatly associated with homeostasis. In Chapter (2), we have seen worm behavior off food exhibits a directional persistence in the body orientation over time scales of almost ~ 100s [76], which provides additional footing to the long range correlations exhibited by N2 worms. In addition, this suggests that *npr-1* mutants might be incapable of maintaining directional persistence, indicating that slow neuromodulatory processes involving the NPR-1 receptor might be involved in controlling these longer time scale behaviors.

Interestingly, the run length distributions in the first roaming/dwelling partition of the N2 behavior on food, Fig. (5.6B), are well approximated by a bi-exponential function. However, finer scale structure in behavior, such as the run length distributions for roaming states, Fig. (5.6D-top), or forward states within the roaming state or off food, Figs. (5.7D-top,5.2D-top), exhibit heavy-tails not predicted by a simple two time scale model. These results suggest a compelling picture of *C. elegans* behavior as evolving in a complex energy landscape, for which roaming and dwelling states are well separated by a large energy barrier, Fig. (5.11). Within the roaming state the landscape is more rugged, and as we zoom in the landscape becomes more and more populated with shallow meta-stable states, specially in the forward crawling state. This results in heavy-tailed run length distributions and power law behavior of the autocorrelation function of the first non-trivial eigenfunction of the transfer operator. This toy model of the dynamics highlights how complexity emerges at the finer scales of

behavior, and agrees with the picture of [1], were we found hints of deterministic chaos underlying the fine scale unpredictability of motion. Chaotic systems exhibit an infinite amount of unstable periodic orbits, which is consistent with the large number of metastable states found at the finer scales of the dynamics. Note, however, that this is merely a toy model of the organization of behavior, as we know that the system is out-of-equilibrium. To be taken seriously, this energy landscape needs to be time dependent, in order to include the effects of the environment, genetic mutations, and neuromodulation. In addition, the transitions between potential wells need not be driven by thermal noise, as finer scale transitions are, at least conceptually, well approximated by the chaotic meandering in a landscape of unstable periodic orbits. Nonetheless, this offers a useful mental picture of the organization of behavior over multiple time scales, brought to life through the transfer operator framework introduced in this thesis. Further research will be needed to make this picture physically precise.

Recent studies on animal behavior have found non-Markovianity in the behavioral dynamics, which was interpreted as a signature of dynamical complexity through the existence of unobserved internal states [6, 8]. However, we have shown that using Markovianity as a criterion for the definition of state provides an accurate representation of the dynamics over multiple time scales, and allows us to extract complex longer lived internal states directly. Nonetheless, and despite our effort to find a complete representation of state, there are features of the dynamics we fail to capture, such as the heavy tailed distributions in the run lengths, or the long range correlations and power law behavior in the slow mode dynamics. Analysing postural dynamics through the operator theoretic formalism presented here offers a new compelling route for a deeper understanding of animal behavior on multiple time scales, and how it emerges from the underlying neuronal and genetic machinery. We expect our approach to be widely applicable.

5.8. METHODS

STATE SPACE RECONSTRUCTION

Given a D-dimensional time-series in $Y = [\mathbf{y}_1^{1:T}, \cdots, \mathbf{y}_D^{1:T}]$, along with an estimate of the optimal embedding window K^*, and minimum embed-

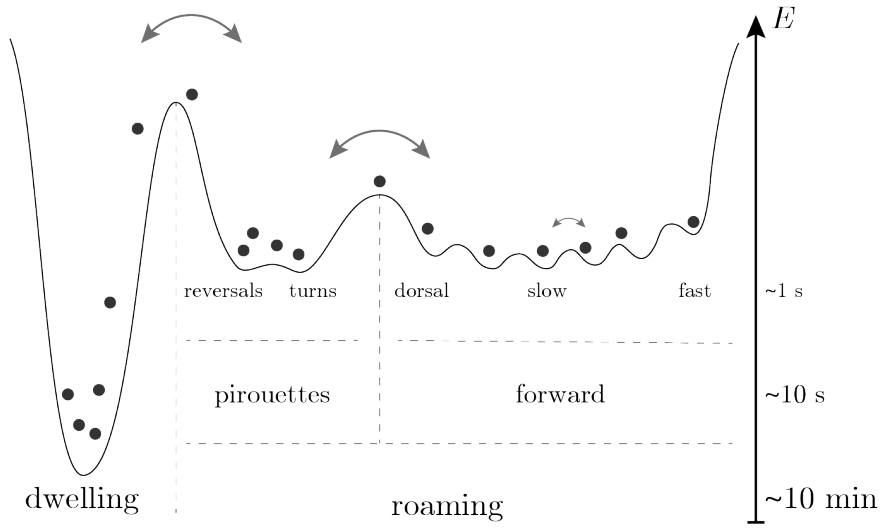

Figure 5.11: ***C. elegans* locomotion in an energy landscape.** At longer time scales, roaming and dwelling states are well separated by a deep energy barrier, which results in a run length distribution with two clear time scales, Fig. (5.6B). As we zoom in, the roaming state is broadly split into forward states and pirouette states. Within these states, specially in the forward state, the landscape becomes more and more rugged as we zoom in, with a very large number of metastable states being separated by very shallow energy barriers. This results in heavy tailed run length distributions, as well as power law decay of the autocorrelation function of the slowest eigenfunction.

ding dimension m^*, the state space reconstruction proceeds as follows. First, we create the $L \times K^* D$ matrix $\overline{Y}_{K^*}$ containing delayed copies of the measurements, $\overline{Y}_{K^*} = [\mathbf{y}_{1:D}^{1:L}, \mathbf{y}_{1:D}^{2:(L+1)}, \cdots, \mathbf{y}_{1:D}^{K:T}]$, where $L = (T - K^* + 1)$. We then perform SVD and keep the first m^* left-singular vectors, which we then whiten [77] to obtained uncorrelated rescaled modes. In the case of *C. elegans* postural dynamics measurements consist of 5D time series of eigenworm coefficients. In order to estimate K^* and m^*, we take the following procedure. For a given choice of K, we build trajectory matrices $\overline{Y}_K$ for each worm in a dataset, and then estimate the entropy rate of $\overline{Y}_K$ by partitioning the state space into N Voronoi cells through k-means clustering, and maximizing the entropy as a function of the number of partitions, as well as over the $n = 50$ different initializations of the partitioning algorithm. This yields an estimate of the entropy rate for each K and for each worm trajectory. We then bootstrap over worms to obtain 95% confidence intervals on the estimates of the average maximum entropy rate across worms. The same procedure is applied to the estimates of the entropy as a function of m, except that now we partition the state space given by the first m whitened singular vectors of $\overline{Y}_{K^*}$.

5

IDENTIFICATION OF COHERENT SETS AND IMPLIED TIME SCALES

We build the approximation of the reversibilized transfer operator as in Chapter (4). We partition the state space into Voronoi cells through k-means clustering, and estimate the transition probabilities between all microstates, $P(\tau, N)$, Eq. (4.10). We then build the reversibilized transfer operator, $R(\tau, N)$, Eq. (4.3), which we diagonalize using ARPACK [78] constrained on finding the k eigenvalues with largest real part. The first nontrivial eigenfunction is clustered using fuzzy c-means clustering [79], using the scikit-fuzzy package [80] in Python [81]. The transition time scale is chosen long enough such that the implied time scales, Eq.(4.2), reaches an asymptote. In addition to the Markovianity condition, when constructing coherent sets we also try to maximize the time scale gap between the first and second implied time scales. In order to get error bars in the implied time scales, we bootstrap over uncorrelated trajectories obtained by splitting the trajectory into shorter segments that are long enough such that the implied time scales converge clearly.

DWELL TIME DISTRIBUTION FITS

We fit the dwell time distributions using the lmfit package [82] for Python [81]. Errors are obtained through the covariance matrix of the least-squares regression.

STATE SUBDIVISION

Our approach to state subdivision is similar to [26], and the idea of relatively coherent sets. At each step in the subdivision process, we isolate the microstates from each coherent set and estimate the reversibilized Markov chain on those microstates only. The spectrum of each of the Markov chains allows us to identify the most cohesive set by the largest first non-trivial eigenvalue. We then use fuzzy c-means clustering [80, 83] to split the most cohesive state into its coherent sets.

SIMULATING *C. elegans* POSTURAL DYNAMICS THROUGH THE TRANSFER OPERATOR

In order to simulate worm trajectories, we first approximate the Perron-Frobenius operator, $P(\tau, N)$, in an example worm with $\tau = 4$ frames and $N = 4000$ partitions. Starting from a random discrete state, s_i, we obtain new states s_j by sampling from the transition probability conditioned on the current state, $p(s_j|s_i) = P_{i,j}(\tau, N)$. From the newly generated sequence of discrete states, we obtain continuous states by randomly picking a point from each discrete microstate in the sequence. Finally, we obtain eigenworm coefficients by projecting the continuous state back onto the trajectory matrix $\overline{Y}_K$ and taking the last time point from the K frames window.

DATA

N2 off food data: We analyzed previously published data consisting of foraging behavioral conditions [20, 84] in which N2-strain *C. elegans* were imaged at $f = 32$ Hz with a video tracking microscope. Coiled shapes were resolved and the time series downsampled to $f = 16$ Hz [21]. Worms were grown at $20°C$ under standard conditions [85]. Before imaging, worms were removed from bacteria-strewn agar plates using a platinum worm pick, and rinsed from *E. coli* by letting them swim for 1 min in NGM buffer. They were then transferred to an assay plate (9 cm Petri dish) that con-

tained a copper ring (5.1 cm inner diameter) pressed into the agar surface, preventing the worm from reaching the side of the plate. Recording started approximately 5 min after the transfer, and lasted for 2100 s.

N2 on food data: We analyzed open access data in which N2-strain *C. elegans* were freely moving in a food-full environment. Worms were grown at room temperature $\sim 22°C$ and maintained on standard NGM plates [86] with three drops of OP50 bacteria. The 3.5cm low-peptone NGM imaging plates were seeded with 20μl of OP50, in the center of the plate, and allowed to dry: the drop of OP50 is nearly circular with ~ 8mm in diameter. Worms were then transferred to the center of the plate, one worm per plate, and given 30 minutes of habituation, after which they were tracked for 15 minutes. Worms were imaged on an immobile platform isolated from tracking motion. In these experiments, sampling rate varied from 20 – 30 Hz. We selected 150 worms sampled at 30.0303 Hz to ensure a uniform sampling rate. For more experimental details, see [87]. Processing of the image frames was done using a custom made machine learning solution detailed below [88].

***npr-1* data:** We analyzed open access data in which *npr-1* mutants were freely moving in a food-full environment. The dataset consistend of 15 minute trajectories from 7 worms, sampled at 20 Hz. All other details of the experiments are the same as for the N2 data on food. For details, see [87].

Deep-learning tracking solution: The method used to solved coiled shapes in the foraging dataset [21] is a powerful tool for solving this complex image processing problem, but requires a large amount of computer time, making it impractical to use in large datasets. We developed a novel deep network solution to this problem, pioneered by Laetitia Hebert at OIST[2], which can produce results of similar quality (or better) than the algorithm used in [21], yet is orders of magnitude faster [88]. Using the results from [21], we train a Gaussian Mixture Model, which serves as a generative model of novel body shapes. Then, using [89] we generate realistic looking worm images: we learn the texture of the worm images in frames where the worms are not coiled, and feed this texture to artificially generated body shapes. This allows us to generate an infinite amount of training data, regardless of the details of the experimental conditions. Given this

[2]Okinawa Institute for Technology, Japan

training data, we use a Residual Network [90], in which we replace the last softmax layer with a fully connected regression layer. For the N2 worms on food, and the *npr-1* mutants, we first extract the centerline and morphological features of the worm using tierpsy-tracker [91, 92]. This information is then used to generate the training data with which to train the network and predict on the real images. In this way, we are able to get solutions for images that are challenging to analyse using classical tracking solutions, like images in which the worm exhibits a coiled shape or that are too blurry for classical tracking to work. After extraction of the centerline, and the tangential angles along it, we project those angles onto a canonical set of eigenworms [20].

ACKNOWLEDGEMENTS

We thank SURFsara (www.surfsara.nl) for computing resources through the Lisa system. This work was supported by the research program of the Foundation for Fundamental Research on Matter (FOM), which is part of the Netherlands Organization for Scientific Research (NWO), and also by funding from The Okinawa Institute of Science and Technology Graduate University. We thank David Jordan and Tosif Ahamed for useful discussions.

REFERENCES

[1] T. Ahamed, A. C. Costa, and G. J. Stephens, *Capturing the Continuous Complexity of Behavior in C. elegans,* (2019), arXiv:1911.10559 [q-bio.NC] .

[2] R. F. Schwarz, R. Branicky, L. J. Grundy, W. R. Schafer, and A. E. X. Brown, *Changes in postural syntax characterize sensory modulation and natural variation of c. elegans locomotion,* PLOS Comput. Biol. **11**, 1 (2015).

[3] A. C. Costa, T. Ahamed, and G. J. Stephens, *Adaptive, locally linear models of complex dynamics,* Proceedings of the National Academy of Sciences of the United States of America **116**, 1501 (2019).

[4] G. J. Berman, D. M. Choi, W. Bialek, and J. W. Shaevitz, *Mapping the stereotyped behaviour of freely moving fruit flies.* J. Royal Soc. Interface **11**, 1 (2014).

[5] A. B. Wiltschko, M. J. Johnson, G. Iurilli, R. E. Peterson, J. M. Katon, S. L. Pashkovski, V. E. Abraira, R. P. Adams, and S. R. Datta, *Mapping Sub-Second Structure in Mouse Behavior,* Neuron **88**, 1121 (2015).

[6] S. Gupta and A. Gomez-Marin, *A context-free grammar for Caenorhabditis elegans behavior,* bioRxiv (2019), 10.1101/708891.

[7] G. J. Berman, *Measuring behavior across scales,* BMC Biol. **16** (2018), 10.1186/s12915-018-0494-7.

[8] G. J. Berman, W. Bialek, and J. W. Shaevitz, *Hierarchy and predictability in Drosophila behavior,* Proceedings of the National Academy of Sciences **104**, 20167 (2016).

[9] D. J. Anderson, *Circuit modules linking internal states and social behaviour in flies and mice,* Nature Reviews Neuroscience **17**, 692 (2016).

[10] C. I. Bargmann and E. Marder, *From the connectome to brain function,* Nat Methods **10** (2013), 10.1016/j.cub.2012.01.061.

[11] F. Libersat and H.-J. Pflueger, *Monoamines and the Orchestration of Behavior,* BioScience **54**, 17 (2004).

[12] O. Hobert, *Behavioral plasticity in C. elegans: Paradigms, circuits, genes,* Journal of Neurobiology **54**, 203 (2003).

[13] S. M. Kim, C.-Y. Su, and J. W. Wang, *Neuromodulation of Innate Behaviors in Drosophila ,* Annual Review of Neuroscience **40**, 327 (2017).

[14] S. Nagy, N. Tramm, J. Sanders, S. Iwanir, I. A. Shirley, E. Levine, and D. Biron, *Homeostasis in C. elegans sleep is characterized by two behaviorally and genetically distinct mechanisms,* eLife **3**, e04380 (2014).

[15] M. J. Krashes, S. DasGupta, A. Vreede, B. White, J. D. Armstrong, and S. Waddell, *A Neural Circuit Mechanism Integrating Motivational State with Memory Expression in Drosophila,* Cell **139**, 416 (2009).

[16] V. M. Corrales-Carvajal, A. A. Faisal, and C. Ribeiro, *Internal states drive nutrient homeostasis by modulating exploration-exploitation trade-off,* eLife **5**, e19920 (2016).

[17] B. B. Shtonda and L. Avery, *Dietary choice behavior in Caenorhabditis elegans,* Journal of Experimental Biology **209**, 89 (2006).

[18] N. A. Croll, *Behavioural analysis of nematode movement,* Adv. Parasitol. **13**, 71 (1975).

[19] J. Likitlersuang, G. Stephens, K. Palanski, and W. S. Ryu, *C. elegans tracking and behavioral measurement,* J Vis Exp , e4094 (2012).

[20] G. J. Stephens, B. Johnson-Kerner, W. Bialek, and W. S. Ryu, *Dimensionality and dynamics in the behavior of C. elegans.* PLoS Comput. Biol. **4**, e1000028 (2008).

[21] O. D. Broekmans, J. B. Rodgers, W. S. Ryu, and G. J. Stephens, *Resolving coiled shapes reveals new reorientation behaviors in c. elegans,* eLife **5(e17227)** (2016), 10.7554/eLife.17227.

[22] J. T. Pierce-Shimomura, T. M. Morse, and S. R. Lockery, *The fundamental role of pirouettes in Caenorhabditis elegans chemotaxis.* J. Neurosci. **19**, 9557 (1999).

[23] S. J. Helms, W. M. Rozemuller, A. C. Costa, L. Avery, G. J. Stephens, and T. S. Shimizu, *Modelling the ballistic-to-diffusive transition in nematode motility reveals variation in exploratory behaviour across species,* Journal of The Royal Society Interface **16**, 20190174 (2019).

[24] J. M. Gray, J. J. Hill, and C. I. Bargmann, *A circuit for navigation in Caenorhabditis elegans.* Proceedings of the National Academy of Sciences of the United States of America **102**, 3184 (2005).

[25] J. L. Donnelly, C. M. Clark, A. M. Leifer, J. K. Pirri, M. Haburcak, M. M. Francis, A. D. T. Samuel, and M. J. Alkema, *Monoaminergic Orchestration of Motor Programs in a Complex C. elegans Behavior,* PLoS Biology **11** (2013), 10.1371/journal.pbio.1001529.

[26] T. Ma and E. M. Bollt, *Relatively coherent sets as a hierarchical partition method,* International Journal of Bifurcation and ChaosJ **23**, 1 (2013).

[27] G. Froyland, S. Lloyd, and N. Santitissadeekorn, *Coherent sets for nonautonomous dynamical systems,* Physica D: Nonlinear Phenomena **239**, 1527 (2010).

[28] K. Deng, P. G. Mehta, and S. P. Meyn, *Optimal kullback-leibler aggregation via spectral theory of markov chains,* IEEE Transactions on Automatic Control **56**, 2793 (2011).

[29] K. Li, A. Javer, E. E. Keaveny, and A. E. Brown, *Recurrent neural networks with interpretable cells predict and classify worm behaviour,* NIPS (2017), 10.1101/222208.

[30] E. E. Keaveny and A. E. Brown, *Predicting path from undulations for C. Elegans using linear and nonlinear resistive force theory,* Physical Biology **14** (2017), 10.1088/1478-3975/aa5ce6.

[31] J. Ben Arous, S. Laffont, and D. Chatenay, *Molecular and sensory basis of a food related two-state behavior in C. elegans,* PLoS ONE **4**, 1 (2009).

[32] S. W. Flavell, N. Pokala, E. Z. Macosko, D. R. Albrecht, J. Larsch, and C. I. Bargmann, *Serotonin and the neuropeptide PDF initiate and extend opposing behavioral states in C. elegans,* Cell **154**, 1023 (2013).

[33] I. Hums, J. Riedl, F. Mende, S. Kato, H. S. Kaplan, R. Latham, M. Sontag, L. Traunmüller, and M. Zimmer, *Regulation of two motor patterns enables the gradual adjustment of locomotion strategy in caenorhabditis elegans,* eLife **5**, 1 (2016).

[34] L. Avery and H. R. Horvitz, *Effects of starvation and neuroactive drugs on feeding in Caenorhabditis elegans,* Journal of Experimental Zoology **253**, 263 (1990).

[35] M. Chalfie, J. Sulston, J. White, E. Southgate, J. Thomson, and S. Brenner, *The neural circuit for touch sensitivity in Caenorhabditis elegans,* J. Neurosci. **5**, 956 (1985).

[36] M. De Bono and C. I. Bargmann, *Natural variation in a neuropeptide Y receptor homolog modifies social behavior and food response in C. elegans,* Cell **94**, 679 (1998).

[37] J. Gray, *How Animals Move*, Pelican books (Cambridge University Press, 1953).

[38] E. R. Sawin, R. Ranganathan, and H. R. Horvitz, *C. elegans locomotory rate is modulated by the environment through a dopaminergic pathway and by experience through a serotonergic pathway,* Neuron **26**, 619 (2000).

[39] M. Fujiwara, P. Sengupta, and S. L. McIntire, *Regulation of body size and behavioral state of C. elegans by sensory perception and the EGL-4 cGMP-dependent protein kinase.* Neuron **36**, 1091 (2002).

[40] A. E. X. Brown, E. I. Yemini, L. J. Grundy, T. Jucikas, and W. R. Schafer, *A dictionary of behavioral motifs reveals clusters of genes affecting Caenorhabditis elegans locomotion,* Proceedings of the National Academy of Sciences of the United States of America **110**, 791 (2013).

[41] S. Stern, C. Kirst, and C. I. Bargmann, *Neuromodulatory Control of Long-Term Behavioral Patterns and Individuality Article Neuromodulatory Control of Long-Term Behavioral Patterns and Individuality across Development Authors,* Cell (2017), 10.1016/j.cell.2017.10.041.

[42] B. H. H. Cheung, M. Cohen, C. Rogers, O. Albayram, and M. de Bono, *Experience-dependent modulation of C. elegans behavior by ambient oxygen.* Curr. Biol. **15**, 905 (2005).

[43] J. M. Gray, D. S. Karow, H. Lu, A. J. Chang, J. S. Chang, R. E. Ellis, M. A. Marietta, and C. I. Bargmann, *Oxygen sensation and social feeding mediated by a C. elegans guanylate cyclase homologue,* Nature **430**, 317 (2004).

[44] E. Z. MacOsko, N. Pokala, E. H. Feinberg, S. H. Chalasani, R. A. Butcher, J. Clardy, and C. I. Bargmann, *A hub-and-spoke circuit drives pheromone attraction and social behaviour in C. elegans,* Nature **458**, 1171 (2009).

[45] S. Choi, M. Chatzigeorgiou, K. P. Taylor, W. R. Schafer, and J. M. Kaplan, *Analysis of NPR-1 reveals a circuit mechanism for behavioral quiescene in C. elegans,* Neuron **78**, 869 (2013).

[46] A. Gomez-Marin, G. J. Stephens, and A. E. X. Brown, *Hierarchical compression of Caenorhabditis elegans locomotion reveals phenotypic differences in the organization of behaviour,* J. Royal Soc. Interface **13** (2016), 10.1098/rsif.2016.0466.

[47] A. D. Wyner and J. Ziv, *Some asymptotic properties of the entropy of a stationary ergodic data source with applications to data compression,* IEEE Transactions on Information Theory **35**, 1250 (1989).

[48] W. S. Ryu and A. D. T. Samuel, *Thermotaxis in Caenorhabditis elegans analyzed by measuring responses to defined thermal stimuli.* J. Neurosci. **22**, 5727 (2002).

[49] H. A. Zariwala, A. C. Miller, S. Faumont, and S. R. Lockery, *Step response analysis of thermotaxis in Caenorhabditis elegans,* Journal of Neuroscience **23**, 4369 (2003).

[50] B. Zhao, P. Khare, L. Feldman, and J. A. Dent, *Reversal frequency in Caenorhabditis elegans represents an integrated response to the state of the animal and its environment,* Journal of Neuroscience **23**, 5319 (2003).

[51] A. J. Calhoun and M. Murthy, *Quantifying behavior to solve sensorimotor transformations: advances from worms and flies,* Curr. Opin. Neurobiol. **46**, 90 (2017).

[52] D. Givon, R. Kupferman, and A. Stuart, *Extracting macroscopic dynamics: Model problems and algorithms,* Nonlinearity **17**, 1 (2004).

[53] H. Mori, *Transport, Collective Motion, and Brownian Motion,* Progress of Theoretical Physics **33** (1965).

[54] R. Zwanzig, *Nonlinear generalized Langevin equations,* Journal of Statistical Physics **9**, 215 (1973).

[55] G. Froyland, G. A. Gottwald, and A. Hammerlindl, *A Computational Method to Extract Macroscopic Variables and Their Dynamics in Multiscale Systems,* SIAM Journal on Applied Dynamical Systems **13**, 1816 (2014).

[56] A. Bittracher, P. Koltai, S. Klus, R. Banisch, M. Dellnitz, and C. Schütte, *Transition Manifolds of Complex Metastable Systems: Theory and Data-Driven Computation of Effective Dynamics,* Journal of Nonlinear Science **28**, 471 (2018).

[57] S. Klus, F. Nüske, P. Koltai, H. Wu, I. Kevrekidis, C. Schütte, and F. Noé, *Data-Driven Model Reduction and Transfer Operator Approximation,* Journal of Nonlinear Science **28**, 985 (2018), arXiv:1703.10112 .

[58] L. P. Kadanoff, *Scaling Laws for Ising Models near Tc,* Physics **2**, 263 (1966).

[59] A. E. Brown and B. De Bivort, *Ethology as a physical science,* Nature Physics , 1 (2018).

[60] S. R. Datta, D. J. Anderson, K. Branson, P. Perona, and A. Leifer, *Computational Neuroethology: A Call to Action,* Neuron **104**, 11 (2019).

[61] J. C. Coates and M. De Bono, *Antagonistic pathways in neurons exposed to body fluid regulate social feeding in Caenorhabditis elegans,* Nature **419**, 925 (2002).

[62] T. Hills, P. J. Brockie, and A. V. Maricq, *Dopamine and Glutamate Control Area-Restricted Search Behavior in Caenorhabditis elegans,* Journal of Neuroscience **24**, 1217 (2004).

[63] C. Rogers, V. Reale, K. Kim, H. Chatwin, C. Li, P. Evans, and M. De Bono, *Inhibition of Caenorhabditis elegans social feeding by FMRFamide-related peptide activation of NPR-1,* Nature Neuroscience **6**, 1178 (2003).

[64] M. Ezcurra, D. S. Walker, I. Beets, P. Swoboda, and W. R. Schafer, *Neuropeptidergic signaling and active feeding state inhibit nociception in Caenorhabditis elegans,* Journal of Neuroscience **36**, 3157 (2016).

[65] L. D. Landau and E. M. Lifshitz, *Fluid Mechanics, Second Edition: Volume 6 (Course of Theoretical Physics)*, 2nd ed., Course of theoretical physics / by L. D. Landau and E. M. Lifshitz, Vol. 6 (Butterworth-Heinemann, 1987).

[66] P. C. Hohenberg and B. I. Halperin, *Theory of dynamic critical phenomena,* Reviews of Modern Physics **49**, 435 (1977).

[67] T. Hwa and M. Kardar, *Dissipative transport in open systems: An investigation of self-organized criticality,* Physical Review Letters **62**, 1813 (1989).

[68] T. Hwa and M. Kardar, *Avalanches, hydrodynamics, and discharge events in models of sandpiles,* Physical Review A **45** (1992).

[69] G. Grinstein, D. H. Lee, and S. Sachdev, *Conservation laws, anisotropy, and self-organized criticality in noisy nonequilibrium systems,* Physical Review Letters **64**, 1927 (1990).

[70] P. L. Garrido, J. L. Lebowitz, C. Maes, and H. Spohn, *Long-range correlations for conservative dynamics,* Physical Review A **42**, 1954 (1990).

[71] P. Bak, C. Tang, and K. Wiesenfeld, *Self-organized criticality: An explanation of the 1/f noise,* Physical Review Letters **59**, 381 (1987).

[72] P. Bak, C. Tang, and K. Wiesenfeld, *Self-organized criticality,* Phys. Rev. A **38**, 364 (1988).

[73] T. M. Stawicki, S. Takayanagi-Kiya, K. Zhou, and Y. Jin, *Neuropeptides Function in a Homeostatic Manner to Modulate Excitation-Inhibition Imbalance in C. elegans,* PLoS Genetics **9** (2013), 10.1371/journal.pgen.1003472.

[74] D. R. Chialvo, *Psychophysics: Are our senses critical?* Nature Physics **2**, 301 (2006).

[75] T. Mora and W. Bialek, *Are Biological Systems Poised at Criticality?* Journal of Statistical Physics **144**, 268 (2011).

[76] M. Peliti, J. S. Chuang, and S. Shaham, *Directional locomotion of C. elegans in the absence of external stimuli,* PLoS ONE **8** (2013), 10.1371/journal.pone.0078535.

[77] J. H. Friedman, *Exploratory projection pursuit,* Journal of the American Statistical Association **82**, 249 (1987).

[78] R. B. Lehoucq, D. C. Sorensen, and C. Yang, *ARPACK Users' Guide* (Society for Industrial and Applied Mathematics, 1998) https://epubs.siam.org/doi/pdf/10.1137/1.9780898719628 .

[79] J. C. Bezdek, R. J. Hathaway, M. J. Sabin, and W. T. Tucker, *Convergence theory for fuzzy c-means: counterexamples and repairs,* IEEE Transactions on systems, man, and cybernetics **SMC-17**, 873 (1987).

[80] *Scikit-fuzzy version 0.4.2,* .

[81] G. Rossum, *Python Reference Manual*, Tech. Rep. (Amsterdam, The Netherlands, The Netherlands, 1995).

[82] M. Newville, T. Stensitzki, D. B. Allen, and A. Ingargiola, *LMFIT: Non-Linear Least-Square Minimization and Curve-Fitting for Python,* (2014).

[83] G. Froyland, *Statistically optimal almost-invariant sets,* Physica D: Nonlinear Phenomena **200**, 205 (2005).

[84] G. J. Stephens, M. Bueno de Mesquita, W. S. Ryu, and W. Bialek, *Emergence of long timescales and stereotyped behaviors in Caenorhabditis elegans.* Proc. Natl. Acad. Sci. U. S. A. **108**, 7286 (2011).

[85] J. E. Sulston and S. Brenner, *The DNA of Caenorhabditis elegans.* Genetics **77**, 95 (1974).

[86] S. Brenner, *The Genetics of Caenorhabditis elegans,* Genetics **77**, 71 (1974).

[87] E. Yemini, R. A. Kerr, and W. R. Schafer, *Preparation of samples for single-worm tracking.* Cold Spring Harb. Protoc. **2011**, 1475 (2011).

[88] L. Hebert, A. C. Costa, and G. J. Stephens, *Deep networks with generative training for coiled pose estimation in C. elegans,* in prep. (2020).

[89] G. Rogez and C. Schmid, *Image-based synthesis for deep 3d human pose estimation,* International Journal of Computer Vision **126**, 993 (2018).

[90] K. He, X. Zhang, S. Ren, and J. Sun, *Deep residual learning for image recognition,* CoRR **abs/1512.03385** (2015), arXiv:1512.03385 .

[91] A. Javer, M. Currie, C. W. Lee, J. Hokanson, K. Li, C. N. Martineau, E. Yemini, L. J. Grundy, C. Li, Q. L. Ch'ng, W. R. Schafer, E. A. Nollen, R. Kerr, and A. E. Brown, *An open-source platform for analyzing and sharing worm-behavior data,* Nature Methods **15**, 645 (2018).

[92] A. Javer, *Tierpsy tracker 1.5.0, doi.org/10.5281/zenodo.1323782,* (2018).

SUMMARY

Animal movement is remarkably rich, spanning multiple spatiotemporal scales and exhibiting an intricate combination of variability and sterotypy. We have no trouble identifying movement patterns, such as walking or jumping, even though the precise body motion can be quite variable, with each repetition being slightly different from the last. Similarly, longer time scale sequences of behaviors may appear random, but generally fit higher order interpretable patterns or goals. It is therefore essential to find succinct representations that characterize movement dynamics on multiple scales, if we hope to make connections between motile behavior and the underlying neural, genetic and environmental control mechanisms.

In this thesis, we explore novel physics approaches to the understanding of animal movement. In particular, we focus on the undulatory motion of *C. elegans*, a tiny worm ($\sim 1\,$mm) with a small, fully mapped, nervous system (~ 300 neurons). Worms move by propagating sinusoidal waves along their body and their behavior is typically composed of sequences of forward movements interrupted by sudden reversals and turns, in which the worm coils into itself to change the direction of locomotion. Despite its apparent simplicity, this organism is capable of remarkable behavior, orchestrating a large number of degrees of freedom in order to find food, mates, and adapt to changes in the environment. In addition, decades of research on the biology of the worm provide a deep understanding of its brain, its genes, and the way it develops from an egg to a fully developed organism. Guided by this deep level of biological understanding, we will use *C. elegans* as a test-bed for new quantitative approaches to behavioral analysis, revealing novel insights into the fundamental principles underlying movement behavior.

In **Chapter 2**, we study *C. elegans* motility from a coarse-grained perspective, treating the worm as a vector in the two-dimensional plane, defined from the centroid to the head of the worm. We take video recordings of worms freely moving on an agar plate, and study the trajectories traced by them over time using three measurements: the speed, the angular bearing

with respect to the lab frame, and the orientation of the movement (forward vs backward). Observation indicates that the movement is rather unpredictable, and therefore capturing its essential features requires a statistical description, analogous to that of the Brownian motion of a particle suspended in a fluid. We thus build a succinct parameterization of the dynamics through simple stochastic models built independently for the speed, bearing and orientation dynamics. The speed is modelled through a noisy forcing that relaxes to a mean value on a characteristic time scale. The bearing dynamics are parameterized as a diffusion process with a linear drift, which captures fluctuations about an overall trend. Finally, the orientation dynamics are modelled as a discrete jump process characterized by the time scales of forward and reverse runs. In total, the model is comprised of only 7 parameters: three for speed, two for bearing and two for orientation dynamics. Despite its simplicity, this model accurately captures the statistical properties of the dynamics, and simulations yield trajectories that are remarkably similar to those performed by worms.

C. elegans is part of the *Nematoda* phylum, one the largest and most diverse groups of species. Despite the large variety of habitats in which these nematodes can be found, they share a remarkable degree of anatomical similarity. This allows us to apply the same model across species and therefore study behavioral variability through the variation in the model parameters. We successfully applied our modelling approach to the trajectories of a dozen worms from nine different species of nematodes. Studying the model parameters across worms reveals a main mode of variation which captures a trade-off between exploration and exploitation: on the one end we have worms that exhibit slow speeds and large number of transitions between forward and backward movements (exploiting a local region), and on the other end we have worms that move in relatively straight paths at larger speeds (exploring larger areas). Using this main mode of variation as a phenotype, we find that while some species exhibit a large specificity to their behavior, most exhibit within-species variation that is comparable to that of the across species variability. These differences suggest a possible bet-hedging mechanism, in which individual-to-individual differences are increased in order to provide the species with an evolutionary advantage to deal with variable environments.

In **Chapter 3**, we zoom further into worm behavior and study fine scale

changes in body posture. We take measurements of worms freely moving on an agar plate, and extract the body's centerline from high resolution video tracking. We use a dimensionality reduction technique, called Principal Component Analysis (PCA), to extract a set of lower dimensional modes (called "eigenworms") that captures the wide variety of distinct body postures worms can perform. The time series of "eigenworm" projections provides a way to study the dynamics of the body posture. Close inspection reveals that fine scale postural dynamics is extremely complex, with every single body wave being different from the last. Our approach to the modelling of these dynamics is to decompose them into shorter segments, within which the time evolution of the body posture could be well approximated by linear dynamics. The idea is that even complex dynamics may be locally linear, in the same way a complex shaped surface is locally flat. Linear dynamics are simple: trajectories can only grow, decay, or oscillate. Nonetheless, by tiling together a collection of linear dynamical systems with parameters that change time, we can neatly reproduce complex dynamical patterns in a variety of systems. We use a likelihood-based approach to identify where dynamical breaks occur: as we grow the size of the local window, we essentially ask how likely is it that the new time points can be predicted by the same set of linear parameters. Using this adaptive approach therefore slices a time series into a collection of window of different sizes, within which the dynamics is approximately linear. We leverage this parameterization to cluster the locally-linear dynamics using a novel likelihood-based dissimilarity metric. Applied to the worms dynamics, this method recapitulates the well-known stereotyped behavioral motifs (forward movement, reversals, and turns), but also reveals finer scale variation in these states, including new motifs previously overlooked by ethologists. Given its generality, we were able to apply this method to a large variety of complex time series, revealing interesting structure in the neuronal dynamics of *C. elegans*, mice and local field potential recordings in Monkeys.

Interestingly, we find that across systems the linear dynamics fluctuates in the boundary between stability and instability, in a dynamically critical state that provides the system with a large degree of susceptibility to external stimuli, and that can be modulated either internally or through external perturbations. Transitions between forward and backward locomotion in the worm are accompanied by a bifurcation in the local dynam-

ics from stable to unstable states. Similarly, we find that lower awareness states in the brain of the worm (quiescence) or the Monkey (anaesthesia) induce a shift in the stability of the linear dynamics towards more stable states, therefore lowering the systems susceptibility to external perturbations. These subtle changes in stability can be advantageous by providing the system with a larger degree of flexibility and maneuverability.

In **Chapter 4**, we introduce a novel framework to understand how long time scale exploration strategies (Chapter 2) emerge from combinations of fine scale posture primitives of behavior (Chapter 3). This chapter serves as a theoretical introduction to the following chapter, in which these ideas are applied to the worm locomotion. In systems with a very large number of degrees of freedom and complex non-linear dynamics, the knowledge of the equations of motion often provides little understanding over the phenomenological properties of the system. Take a gas, for example: in principle, we could follow the position and velocity of all the molecules, which sum up to order $O(10^{23})$, and try to write down the equations of motion. However, that would not necessarily allows us to understand the ensemble properties of the gas, such as its temperature, pressure or volume. We will therefore attempt to abstract from the fine-scale trajectory based approach, and study instead the time evolution of ensembles in state space. One of the advantages of the ensemble-based approach is that we can write down a single linear operator, the Perron-Frobenius operator, that evolves densities in time. We essentially trade a finite set of non-linear equations of motion, by an infinite-dimensional linear operator, which we can approximate by making small partitions in the state space and estimating the transition probabilities between these discrete states. We can then use this transition matrix to decompose the dynamics into a hierarchy of spatiotemporal modes and find regions of state space that remain coherent for a long time.

In order to do this from measurement data, we first need to reconstruct the state space of the dynamical system, i.e., to find the set of variables that evolves according to a first order differential equation, meaning that we can predict the immediate future state using only the current state. As an example, take the motion of a bead attached to a spring. Newtonian mechanics dictates that the bead's acceleration is proportional to the position with respect to the rest state, with the proportionality constant given by the spring constant and the mass of the bead. The accel-

eration is defined as the second order derivative of the position: it measures how the velocity changes, which is a measure of how the position changes. What this means is that position alone will not be enough to specify the immediate future of the bead. In fact, we need to know not only the position, but also the velocity in order to know whether the bead is moving away or towards the rest state of the spring. Another way to make an accurate prediction of the future state is to look at the position of the bead at time $x(t)$ and at a time delay $x(t-\tau)$. Adding this extra dynamical degree of freedom into the definition of state yields a maximally predictive state that evolves according to a first order differential equation. In physics, we call this the phase space or the state space of the dynamics. Working with the state space unleashes a higher degree of analytical power, as well as access to dynamical invariants, symmetries and conservation laws. In addition, the ensemble-based approach relies on the fact that we can estimate densities in the full state space. Therefore, we need to reconstruct the state space in order to be able to extract the long-lived patterns of the dynamics from measurement data. In this chapter, we introduce a novel approach to state space reconstruction that leverages the approximation of the Perron-Frobenius (PF) operator to find a maximally predictive state space. We add time delays into the measurement time series and estimate how unpredictable the dynamics is by measuring the entropy rate of the associated PF operator. Without enough delays, the system will look more unpredictable and therefore the entropy rate will be high. As we increase the number of delays, the entropy rate starts decreasing, slower and slower as we approach the right number of delays at which the entropy rate stops changing. This allows us to find the optimal amount of time delays for reconstructing the state space, and also yields a state space discretization which enable an approximation of the PF operator that accurately captures the long time behavior of the system. We then study the spectrum of the operator and extract coherent sets by clustering the first non-trivial eigenfunction, which is the one that decays the slowest to the invariant density. This effectively splits the state space into regions that remain coherent with the flow, meaning that they transition more within that region than outside of it.

To illustrate the extraction of long lived states, we apply this method to the dynamics of an overdamped particle in a double well potential driven by thermal noise. In this case, the slow behavior of the system corre-

sponds to the hopping between the potential wells, which can be neatly identified by clustering the slowest eigenfunction of the PF operator. We demonstrate our state space reconstruction framework with an application to the Lorenz system in the standard chaotic regime. We take incomplete measurements, the time series of the x variable, and try to reconstruct the full state space and its ergodic properties. As we add delays, the entropy rate decays until it stops changing, at which point we have reconstructed the attractor. The topology of the reconstructed trajectories matches that of the underlying dynamical system, and we recover the entropy rate. In addition, we also recapitulate the long time scale spectrum of the PF operator, which remarkably enables us to identify the almost invariant sets of the Lorenz system from incomplete time series measurements. Finally, we make a bridge between deterministic and stochastic dynamical systems by coupling a particle in a double well with the y variable of a fast Lorenz system in the chaotic regime. We use our approach to reconstruct the state space of the dynamics, and recover the underlying time scale separation of the system as well as identify that the slowest dynamics correspond to the hopping between potential wells.

In **Chapter 5**, we apply these ideas to the posture dynamics of *C. elegans*, in order to extract long lived behavioral states from fine scale posture measurements. We start by analysing time series of lab strain N2 worms freely moving in a featureless environment. After extraction of the centerline, we again project the data into the lower dimensional "eigenworm" space. The first step in the analysis is to reconstruct the state space by adding time delays and studying the evolution of the entropy rate of the associated Perron-Frobenius operator. Using this approach, we find that $K^* = 10$ frames is enough to unfold the posture state. We then partition the reconstructed state space and study the spectrum of the associated transition matrix. The slowest eigenfunction decays to the equilibrium distribution on a time scale of ~ 10 s and clustering it reveals long time scale behavioral patterns of forward locomotion and pirouettes: composite behaviors in which the worm performs a reversal followed by a ventral turn. The duration of pirouettes is of order $O(10)$ s, while forward bouts can be as long as $O(100)$ s, much longer than the measurement time scale of $O(0.1)$ s. Using a similar approach, we can further decompose the dynamics into finer scale behaviors, which evolve over shorter time scales: we find that ventral turns generally occur after reversals, while

dorsal turns generally occur during forward locomotion. We further show that we can use the Perron-Frobenius operator to simulate fine scale posture time series, recovering both the stationary properties of the dynamics as well as the time scales of transitions between coarse-grained states.

In the previous analysis, N2 worms were on an environment without food in which they mostly move at higher speeds and explore a large portion of the plate. In contrast, when on food, worms exhibit much longer time scale behavioral patterns, transitioning between a roaming state, characterized by higher centroid speeds and lower angular speeds, and a dwelling state, in which worms stay in a local region of the plate and move at lower speed and higher angular speeds. Switching between these unobserved internal states is driven by changes in the expression of different types of neuromodulators, that effectively change the frequency with which worms transitions between different fine scale behaviors. For on-food worms, the entropy rate as a function of the number of delays indicates that $K^* = 15$ frames is enough the reconstruct the state space, which we partition in order to build an approximation of the PF operator. Analysis of the spectrum shows that the slowest decaying eigenfunction takes about $O(100)$ s to decay to the invariant density, about an order of magnitude longer than the decay time obtained in the off-food setting. Notably, clustering this eigenfunction yields two coarse-grained states with dwell times of up to ~ 500 s, which we can show correspond to the previously described roaming and dwelling states. We can therefore extract changes at the level of neuromodulation on long time scales, from high resolution posture measurements on short time scales.

Given the tremendous effect food has on the behavior of N2 worms, we decided to study a genetic mutant with a modified response to food: *npr-1*. The *npr-1* mutations impairs the expression of a neuropeptide receptor in a collection of sensory neurons, which would serve to inhibit their sensitivity when the conditions are favorable. In the absence of this receptor, *npr-1* worms become hypersensitive to the effects of environmental oxygen and pheromones. Because of this, the *npr-1* mutation overrides the transition from roaming to dwelling, and these worms typically move at higher speeds than N2 worms on food. As before, we take high resolution posture measurements of *npr-1* mutants crawling on a food-full plate, and study the time series of the lower dimensional projection into "eigenworm" space. Using the behavior of the entropy rate as

a function of the time delays, we choose $K^* = 11$ frames to reconstruct the state space, which we then partition in order to approximate the action of the PF operator. Unlike the N2 behavior on food, the longest time scale of the operator is now of $O(10)$ s, similar to what we found in the N2 off-food behavior. Therefore, we find a mutation that effectively removes the long time scale behavior found in wild type N2 worms on food.

The decomposition offered by the PF operator provides means to build effective phenomenological models on the slow dynamics. In fact, in ergodic systems with a large time scale separation it is possible to identify effective hydrodynamics variables, which are driven by noisy terms that correspond to the fast dynamics. Inspired by these approaches, we decided to study the time evolution of the projection onto the slowest eigenfunction of the Perron-Frobenius operator. As a first order measure of the dynamics, we computed the autocorrelation function of the slowest non-trivial eigenfunction across experiments. Remarkably, the slow dynamics of N2 worms exhibits long range correlations of $O(100)$ s. In addition, the *npr-1* mutation destroys these long range correlations, decaying in ~ 10 s. Plotting the N2 autocorrelation functions in a log-log scale, we find a significant power law regime, with an exponent that is higher off food (indicating the correlations decay slower on food). Power law autocorrelation functions are found in systems with scale free correlations and therefore we decided to take a renormalization group approach in time: we average the eigenfunction projections in short windows and re-estimate the autocorrelation functions. Remarkably, the autocorrelation functions collapse after rescaling according to the correlation time, providing further strong evidence of the scale-free nature of the dynamics. Power law behavior in the dynamics of hydrodynamics variables is a signature of out-of-equilibrium systems with conservation laws. The fact that *npr-1* does not exhibit long range correlations indicates that this mutants fail to maintain the conservation law. Interestingly, this is consistent with physiological studies that show that the NPR-1 receptor is essential to keep the balance between excitation and inhibition in motor neurons and to maintain homeostasis. These results suggest that slow hydrodynamic modes with scale-free correlations might exist due to the fact that organisms have evolved to orchestrate a large number of degrees of freedom, while keeping a tight balance between order and disorder.

ACKNOWLEDGEMENTS

This thesis would not be possible without the precious help and support from a large number of people, to whom I am forever indebted.

First of all, I need to express my deepest gratitude to my thesis supervisor, **Greg Stephens**. Your support, motivation, sharp insight and mentorship were fundamental in my learning and growth, both academically and personally. You have always encouraged and supported me to develop my own research ideas, and had a surgical sense of what I needed to grow. Your guidance and encouragement to participate in sharply chosen graduate schools and international conferences was fundamental. Thanks for letting me be part of such a broad and inspiring research group: from our VU group, to AMOLF and all the way to OIST. I'd also like to extend my gratitude to **Tom Shimizu**, for the insightful discussions and decisive attention to detail, which have undoubtedly sharpened my research. Special thanks to **Onno Broekmans** and **Stephen Helms**: your support was crucial when entering the world of biophysics and data analysis.

Tosif-san, I am also deeply indebted to you, you've taught me a great deal. Thanks for engaging in so many scientific discussions and for guiding me in dynamical systems land. Also, thanks for being such a great guide in Okinawa, I'll never forget those trips! **Mathijs**, thanks for sharing some of that experimental genius you have. It was a huge pleasure to share the PhD experience with you. Your energy is contagious: from the fun escape rooms to the trips to Cargese, Veldhoven or Haarlem, your presence has certainly made everything much more fun. **Liam**-san, it has been a great pleasure to share such great moments of science and friendship with you. Thank you for our half-broken tea breaks and all the insightful discussions we had over the white board. The trips to Japan, the US or Lisbon were made much better by your company. **Steffen**, it was great to have you on board and share my research with you. Your insight and guidance were an important part of my development, so thanks. Also thanks for having such a great spirit and engaging in so many fun activities. **Laetitia**, I have to thank you for playing such an important role in my development as a researcher. Thanks for all the insightful discussions,

and for sharing your coding expertise with me. **Kasia**, **Johan** and **Tatsuo**, thanks for being such great hosts in Okinawa and for your thoughtful insights on my research! **Rahiel**, **Abel**, **Nardi**, **Udi**, **Max**, **Lakshmi**, **Stan**, **Rico**, **Roshel**, **Mauricio**, **Dorien**, **Jair**, **Simon** and **Rafael**, thanks for bringing so much energy to the research group during your projects, it was great to share ideas and fun moments with you.

I'd like to express my gratitude to **Marcelo Magnasco**, for hosting me at Rockefeller University and bringing me into his fascinating scientific world. Special thanks also to **Andre Brown**, for all the support and insightful discussions in Lisbon, Marseilles or Okinawa, and for being such a great host in London. **David Jordan**, our discussions proved fundamental in the development of my research ideas. Thanks for being such a great host in London and for sharing your cocktail expertise!

5

Arigato **Naoko**-san for all the support at OIST and bedankt **Marja** for helping me in so many occasions at the VU. I would like to thank SURFsara for computing resources though the Lisa and Cartesius systems, and OIST for access to Sango and Saion. My research was mostly supported by the Foundation for Fundamental Research on Matter, which is part of the Netherlands Organization for Scientific Research, and also by The Okinawa Institute of Science and Technology Graduate University.

Finally, I would like to express my gratitude to my family and friends. A começar pelos meus pais e o meu mano, para quem irão sempre faltar palavras. Carlos e Isabelinha, obrigado do fundo do coração por serem tamanha inspiração, pelo vosso carinho e motivação, e por incentivarem a minha curiosidade. João, obrigado pela tua amizade e por todas as aventuras que vivemos juntos. Obrigado também por cativares ainda mais a minha curiosidade científica e por partilhares um pouco da tua brilhante intuição matemática. Ao tio Nelo, por todos os ensinamentos e pelo apoio em Coimbra, obrigado! Obrigado também aos amigos de infância, em especial ao Raul e ao Jonhy, por todos os momentos partilhados. Um agradecimento especial à Mariana, pelos momentos de partilha e cumplicidade e por todo o apoio que me deste neste percurso.

Obrigado Pedro pelo design da capa, e José Manuel Lopes de Castro por todo o apoio. Gostaria também de agradecer a um conjunto de professores que marcaram o meu trajecto: Albina, Milai, Sá, Maciel, prima Belinha e Carlos Rodrigues, obrigado pelos vossos ensinamentos. Um agradecimento especial ao professor Ângelo Rosa, a quem devo o facto

de ter decidido estudar física. Aos professores Carlos Fiolhais, Eef van Beveren e Manuela Silva, um muito obrigado pela disponibilidade, apoio e inspiração.

Um obrigado às minhas meninas, Juliana, Margarida e Teresa, por serem uma segunda família para mim. Obrigado por todos os momentos de amizade, apoio e partilha! Um abraço especial também para a Rita, Daniel, Catarina, Zé e restante brigada musical tuga, obrigado por me fazerem sentir em casa! Um forte abraço para os amigos de Coimbra, e em especial para o Trinca, Chato, Tocs, Pato, Piggy e Lea por me acompanharem nesta caminhada. Roberto, Carlos e João, obrigado por todos os momentos passados juntos e pelo vosso apoio. Thanks also to Seba, Fede, Maria, Tata, Guille, Pato, Aki, Giulio, Tamara, Federica, Davide, Robbie, Alice, Eugenio, Zan and mademoiselle Martin for all the fun moments we spent together and for brightening my experience in Amsterdam! Special thanks to my Palpita family, Merel and Ralph, for all the beautiful moments of music and joy. Thanks also to Daisy, Joeri, Marko, Mark, Frank, Manuela and Ronald for getting me on stage with you!

List of Publications

1. Stephen Helms, W. Mathijs Rozemuller, **Antonio Carlos Costa** [†], Leon Avery, Greg J. Stephens and Thomas S. Shimizu *Modeling the ballistic-to-diffusive transition in nematode motility reveals variation in exploratory behavior across species*, Journal of the Royal Society Interface 16 (2019).

2. **Antonio Carlos Costa**, Tosif Ahamed and Greg J. Stephens, *Adaptive locally-linear models of complex dynamics*, Proceedings of the National Academy of Sciences 116, 5 (2019).

3. Tosif Ahamed, **Antonio Carlos Costa** and Greg J. Stephens *Capturing the continuous complexity of behavior in C. elegans*, bioRxiv (2019).

4. **Antonio Carlos Costa**, David Jordan, Tosif Ahamed and Greg J. Stephens *Bridging time scales in C. elegans behavior*, in prep. (2020).

5. Laetitia Hebert, **Antonio Carlos Costa** and Greg J. Stephens *Deep networks with generative training for coiled pose estimation in C. elegans*, in prep. (2020).

6. W. Mathijs Rozemuller, Steffen Werner, **Antonio Carlos Costa**, Greg J. Stephens and Thomas S. Shimizu *Variability and control in C. elegans turning behavior*, in prep. (2020).

[†]Joint first author